Doctoral Thesis

Reliability of Flexible LEDs Investigated by Characterizing Mechanical Properties of Constituent Materials

Si-Hoon Kim

Department of Materials Science and Engineering

Graduate School of UNIST

2019

Reliability of Flexible LEDs Investigated by Characterizing Mechanical Properties of Constituent Materials

Si-Hoon Kim

Department of Materials Science and Engineering
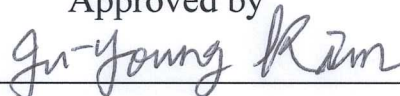
Graduate School of UNIST

Reliability of Flexible LEDs Investigated by Characterizing Mechanical Properties of Constituent Materials

A dissertation

submitted to the Graduate School of UNIST

in partial fulfillment of the

requirements for the degree of

Doctor of Philosophy

Si-Hoon Kim

12. 5. 2018

Approved by
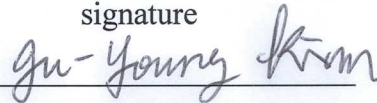
Advisor

Prof. Ju-Young Kim

Reliability of Flexible LEDs Investigated by Characterizing Mechanical Properties of Constituent Materials

Si-Hoon Kim

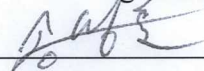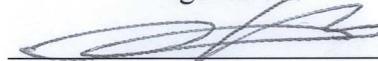This certifies that the dissertation of Si-Hoon Kim is approved.

12.5.2018

signature
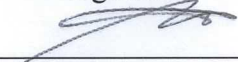
Advisor: Prof. Ju-Young Kim

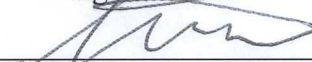signature

Prof. Myung Hoon Song

signature

Prof. Ki-Suk Lee

signature

Prof. Eun-chae Jeon

signature

Prof. Seung-Kyun Kang

Abstract

With increasing consumption of wearable devices, research on flexible displays used as light sources in flexible devices has been conducted in recent years. For realization of flexible, all components of light-emitting diodes (LEDs) must have flexibility. For this reason, studies on organic light-emitting diodes (OLEDs) with high flexibility characteristics are predominant. However, organic semiconductors have disadvantage such as poor color purity with broad full-width half maximum (FWHM) and low-charge carrier mobility. On the other hand, organic-inorganic hybrid perovskites have both characteristics of organic semiconductor materials such as high color purity with narrow full-width half maximum, high charge-carrier mobility and inorganic semiconductor materials such as low processing-cost based on solution process, easy band gap deformation.

Recently, many researches have been conducted to apply perovskite to flexible devices, which have the above advantages, and many flexible devices using perovskite have been developed. However, the study on the deformation characteristics of the developed perovskite flexible LEDs is mainly focused on whether the optical properties are maintained under the deformed state. If all the components deform within the elastic deformation range, they will return to their original state when the external force is removed. When a specific component is subjected to plastic deformation, interface separation phenomenon occurs, which causes a problem in driving the device. For the above reasons, it is important to improve the mechanical characteristics of a weakest material in order to improve the flexibility characteristics of the device. There is a lack of research on flexibility analysis based on mechanical properties.

Although research on flexible devices using perovskite has progressed through the above research. Organic materials react easily with moisture in air and degrade easily, so encapsulation performance of flexible devices must be improved at the same time. Encapsulation performance of flexible devices has been improved through the development of thin film encapsulation (TFE) materials with flexibility characteristic. However, unlike a rigid device using glass as a substrate, a flexible device uses a polymer-based substrate for its deformation characteristics, so that the substrate functions as a moisture infiltration path. Research on substrates for flexible devices with improved encapsulation performance is needed.

In this study, flexibility of perovskite LEDs was analyzed based on the mechanical properties of constituent materials of perovskite LEDs, and substrate for flexible devices with encapsulation properties was developed using silicon dioxide thin films.

The critical bending radius of the perovskite LED was set to be the point where the light intensity starts to decrease when repetitive bending deformation was applied at a specific bending radius. The elastic limit of constituent materials of perovskite LEDs was evaluated using a hole nanoindentation.

In-situ micro tensile test was conducted to measure the exact elastic limit of perovskite, which was the weakest material among the constituent materials. The critical bend radius was analyzed using the measured perovskite elastic limit and the distance from the neutral plane of the LED. The critical bending radius based on mechanical properties was compared with the critical bending radius which decreased the actual efficiency.

The substrate for flexible devices with encapsulation performance was developed using silicon dioxide thin films and analyzed for deformation characteristics. Silicon dioxide thin films were fabricated using sol-gel process. The encapsulation performance of the fabricated silicon dioxide thin film was evaluated by commercialized equipment and accelerating exposure test experiment applied to actual devices. The mechanical properties of silicon dioxide were analyzed by in-situ micro tensile test, and repeated bending tests were performed to evaluate critical bending radius applied to a polymer substrate for flexible device.

Contents

List of Tables

Abbreviation

Devices and perovskite materials

LEDs – Light-emitting diodes

OLEDs – Organic light-emitting diodes

PeLEDs – Perovskite light-emitting diodes

FSPeLED – Flexible and semitransparent perovskite light-emitting diodes

$MAPbBr_3$ – Methylammonium lead tribromide

$MAPbBr_xI_{3-x}$ – Methylammonium lead mixed halide perovskite

MEMS – Microelectromechanical systems

Measurement methods and equipment

AFM – Atomic force measurement

DFT – Density function theory

EELS – Electron energy loss spectroscopy

FEM – Finite element measurement

FIB – Focused ion beam

ICP – Inductively coupled plasma

MD – Molecular dynamic

PECVD – Plasma enhanced chemical vapor deposition

RIE – Reactive ion etching

SEM – Scanning electron microscopy

SIMS – Secondary ion mass spectrometry

TEM – Transmission electron microscopy

UTM – Universal testing machine

Properties of materials

d_n – Distance from neutral plane to bottom surface of target layer

d_f – Thickness of film (target layer)

E – Elastic modulus

L – Luminance intensity

L_{max} – Maximum luminance intensity

r_b – Bending radius

r_c – Critical bending radius

ε_{limit} – Elastic limit

ε_f – Fracture strain

ε_y – Yield strain

σ_f – Fracture strength

σ_y – Yield strength

EQE – External quantum efficiency

PLQE – Photoluminescence quantum efficiency

OTR – Oxygen transmission rate

WVTR – Water vapor transmission rate

Materials

AgNW – Silver nanowire

CF_4 – Tetrafluoromethane

C_4F_8 – Octafluorocyclobutane

CHF_3 – Fluoroform

CNT – Carbon nanotube

HCl – Hydrochloric acid

IPA – Isopropyl alcohol

ITO – Indium tin oxide

NOA – Norland optical adhesive

PDMS -Polydimethylsiloxane

PEDOT:PSS – Poly(3,4-ethylenedioxythiophene)-poly(styrenesulfonate)

PEO - Poly(ethylene oxide)

PET - Polyethylene terephthalate

PMMA - Poly(methyl methacrylate)

PVDF – Polyvinylidene fluoride

SEBS - Styrene Ethylene Butylene Styrene

SF_6 – Sulfur hexafluoride

TCO – Transparent conductive oxide

TEOS – Tetraethyl orthosilicate, $Si(OC_2H_5)_4$

TiO_2 – Titanium oxide

XeF_2 – Xenon difluoride

1. Introduction

As the demand of wearable devices increases, researches on deformable devices such as flexible and stretchable devices have increased. To ensure the flexibility of the device, all components must have sufficient deformation characteristics. Organic materials, which are widely used as an emission layer of a flexible device, are excellent in deformation characteristics but have a disadvantage in that they lack optical characteristics. In order to secure this point, much attention has been focused on organic / inorganic hybrid perovskites, which have both the characteristics of organic materials with low-cost solution-based processing and tunable band gap and the characteristics of inorganic materials with excellent optical properties.

Recently, many researches have been conducted to apply perovskite to flexible devices. Since indium tin oxide electrode, which is widely used as an electrode for a rigid perovskite LED, has a poor deforming property, many studies have been conducted to replace it with a flexible electrode. Flexibility of the device was evaluated by changing the efficiency under repetitive bending of fabricated devices. However, there has been no any analytical and systematical studies on flexible perovskite LEDs for analyzing the mechanical properties of each component layer, in order to determine which layer is the weakest under mechanical bending.

Additionally, deformation properties of perovskite LEDs are important to apply flexible device, but encapsulation performance is also important because the perovskite used as an emission layer is very sensitive to moisture. However, polymeric materials, which are widely used as substrate materials for flexible devices, have high deformation characteristics unlike rigid substrates such as glass and silicon, but they are very poor in barrier properties. Since the substrate acts as a penetration path of moisture, research for improving the moisture-proof property of the polymer substrate is needed.

In this study, flexible of light-emitting diodes was evaluated using mechanical properties of constituent materials and silicon dioxide thin films for encapsulation materials were fabricated by sol-gel process. Flexible LEDs were fabricated using perovskite used as emission layer in device and critical bending radius of perovskite LEDs was analyzed by changing of efficiency during repeated bending tests. Mechanical tests such as hole-nanoindentation and micro-tensile test were carried out to measure mechanical properties of constituent materials of perovskite LEDs. Critical bending radius was evaluated by elastic limit of constituent materials and compared to critical bending radius measured by experimentally. Silicon dioxide thin films were prepared by sol-gel process in amorphous phase. The fabricated films were analyzed for barrier properties for use as encapsulation materials. Mechanical properties were measured by tensile test in order to analyze critical bending radius. Repeated bending tests were carried out near the critical bend radius to evaluate the applicability to flexible devices.

2. Theoretical background

2.1 Perovskite light emitting diodes (PeLEDs)

Organic-inorganic hybrid perovskite have emerged as suitable materials for photovoltaic devices due to several advantages such as very high color purity with a narrow full-width half maximum (FWHM) regardless of crystal size, high charge-carrier mobility, high photoluminescence quantum yield (PLQY), low-cost solution-based processing, and a simply tunable band gap. Therefore, perovskite is an attractive material as emission material for light-emitting diodes[1-10].

In early days, methylammonium lead mixed halide perovskite ($MAPbBr_xI_{3-x}$) and methylammonium lead tribromide ($MAPbBr_3$) have low external quantum efficiency as 0.76% for near-infrared and 0.1% for green regimes, respectively[1]. Near-infrared device was fabricated using a thin 15 nm layer of $MAPbBr_xI_{3-x}$ perovskite layer positioned between titanium oxide (TiO_2) and poly(9.9'-dioctyl-fluorene) (F8) layers. Device of green light emitted was fabricated using $MAPbBr_3$ with indium tin oxide (ITO) and poly(3, 4-ethylenedioxythiophene) polystyrene sulfonate (PEDOT:PSS) used as anode, F8, Ca, and Ag layers used as cathode. Radiative recombination was performed by effectively confining hole and electron in $MAPbBr_xI_{3-x}$ and $MAPbBr_3$ perovskite layers due to ITO or TiO_2 and F8 in each perovskite LEDs structures. Structures and external quantum efficiency were shown in Figure 2.1. This demonstration This description provided the potential for development of perovskite materials. possibility of developing perovskite materials. This explains the potential for development of perovskite materials

Various efforts have been made to reduce non-radiative recombination and increase photoluminescence quantum efficiency (PLQE). Performance of perovskite LEDs notably improved by two strategies[11-14]. In first strategy, nanocrystalline perovskite directly coated in colloidal state by spin-coating method. Nanocrystalline perovskite have highly luminescent with PLQY of nearly 90% but maximum external quantum efficiency of perovskite LEDs is around 12% for near-infrared and 14% for green regimes, respectively[15]. Optical properties of nanocrystalline perovskite are modified by composition and crystal size. In second strategy, bulk perovskite film was deposited using precursor solutions with long chain ammonium halide additives.

Recently, two studies have been carried out to increase the efficiency of the perovskite and the efficiency of the perovskite has exceeded 20%[16, 17]. In first research, light trapping was mentioned to main cause of efficiency loss due to higher refractive index of perovskite[16]. Sub-micrometer-scale structure of perovskite effectively extractive trapped light from perovskite LEDs. Microstructure of perovskite layer for extraction of trapped light is simply formed by amino-acid additives into precursor solution. Additives effectively passivate defects on perovskite surface and decrease non-radiative recombination. Perovskite LED with amino-additives accomplished peak external quantum efficiency

as 20.7% and energy conversion efficiency as 12%. Related images were shown in Figure 2.2. As shown in Figure 2.3, the second approach requires management of compositional distribution in perovskite device for high luminescence and balanced charge injection[17]. Pre-synthesized $CsPbBr_3$ perovskite solution with CH_3NH_3Br additive was formed quasi-core/shell structure by sequential crystallization due to differing solubilities. Photoluminescence quantum efficiency was boosted by passivated non-radiative defects due to CH_3NH_3Br shell.
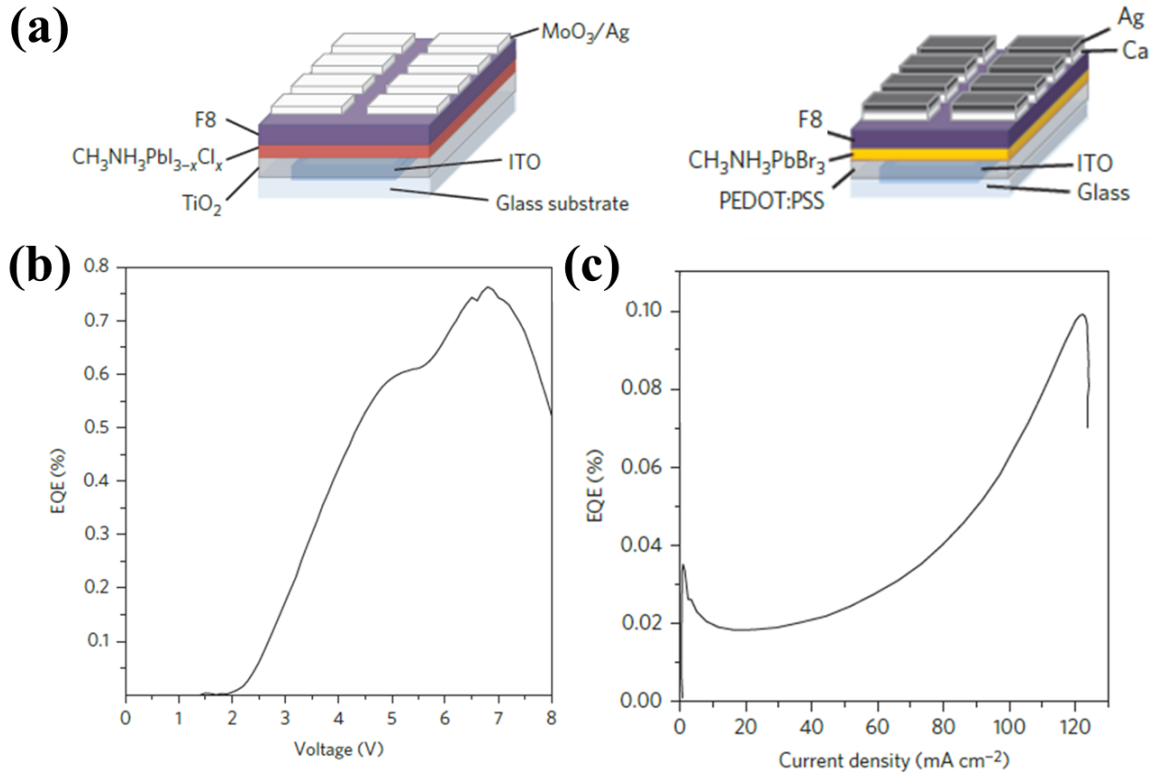
Figure 2.1. (a) Schematic of structure of near-infrared (left) and green (right) perovskite LEDs. (b) External quantum efficiency versus voltage curve of near-infrared perovskite LEDs. (c) External quantum efficiency versus current density curves of green perovskite LEDs[1].

3
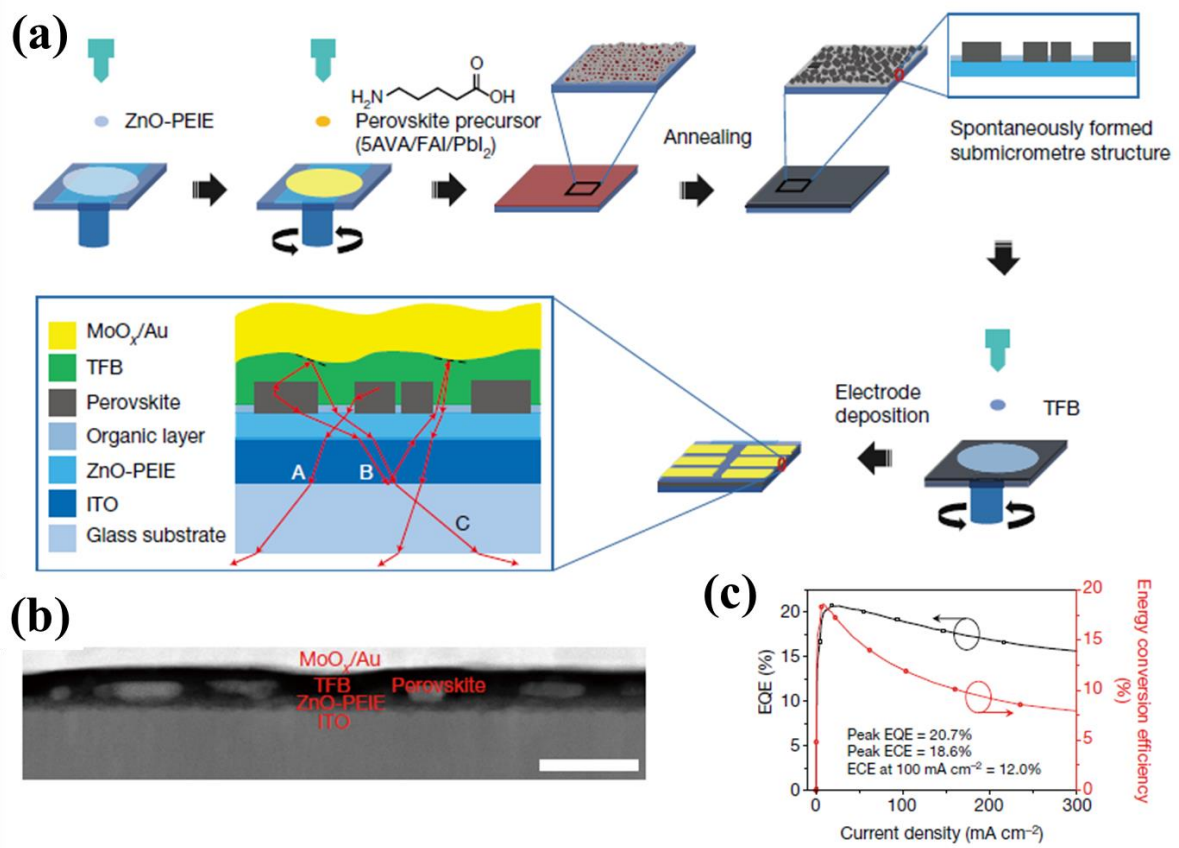
Figure 2.2. (a) Schematic of fabrication process of device with sub-micrometer structure. Rays A, B, and C is extracted by sub-micrometer structure. (b) STEM image of fabricated device. (c) External quantum efficiency and energy conversion efficiency plotted against current density[16].
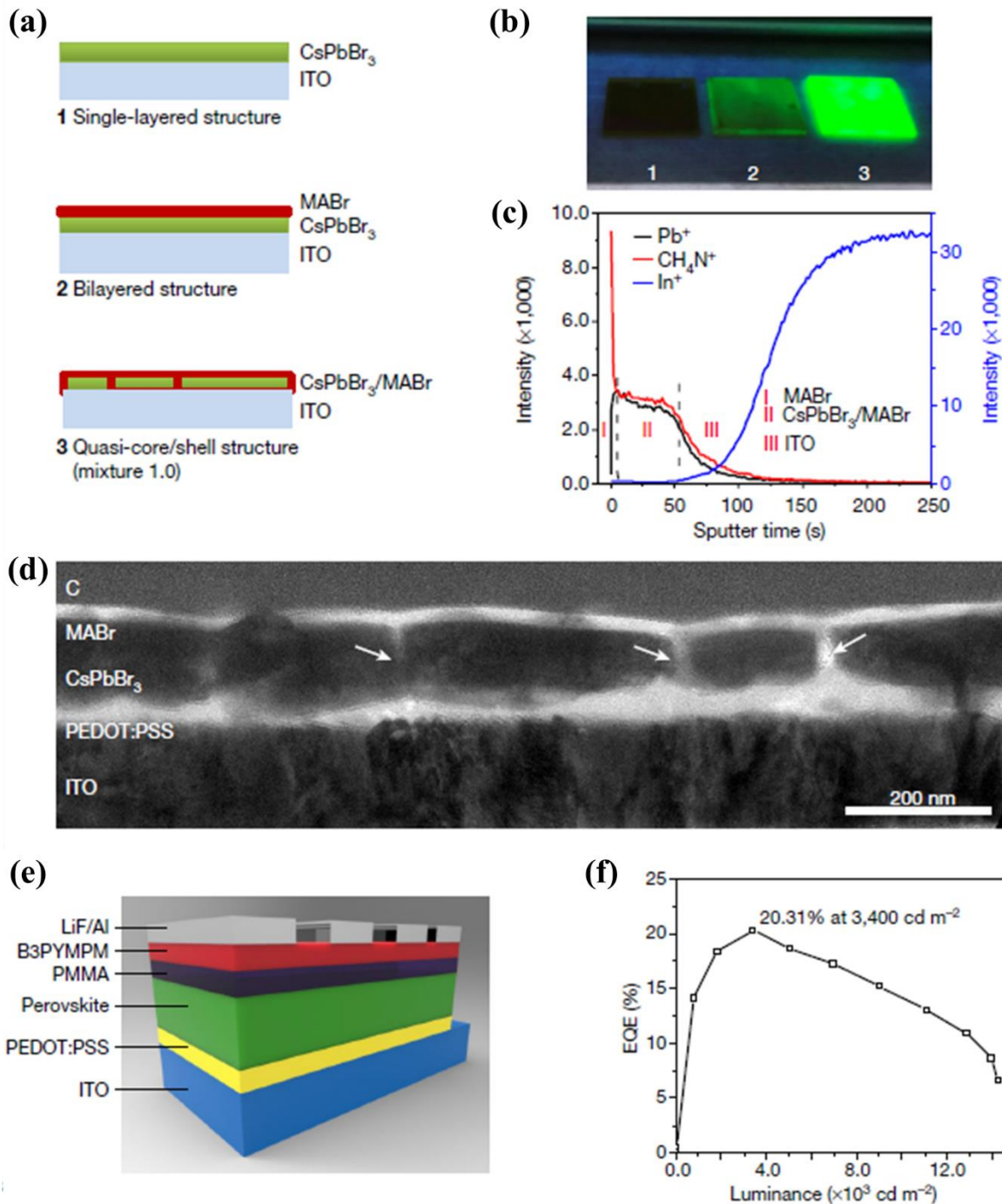
Figure 2.3. (a) Schematic of quasi-core/shell perovskite layer fabrication process, (b) Photo of three perovskite films under ultra-violet light. (c) SIMS depth analysis of quasi-core/shell structure perovskite films. (d) Cross-sectional TEM image of quasi-core/shell structure perovskite on PEDOT:PSS. (e) Schematic of quasi-core/shell perovskite LEDs with thin PMMA layer. (f) characteristic of best-performing perovskite LEDs[17].

2.2 Flexible perovskite light emitting diodes

For the realization of flexible and stretchable displays, each component layer of the devices should also be flexible and stretchable. Thus, flexible and stretchable organic light-emitting diodes (OLEDs) are being studied extensively, given the excellent flexibility and stretchability of organic materials. Recently, many researches have been conducted to apply perovskite to flexible devices. However, indium tin oxide (ITO) electrodes, which are conventional transparent conductive oxide (TCO) used in rigid devices, are not suitable for flexible devices because ITO electrode is brittle. Therefore, developing an electrode to replace the ITO electrode is most important in realizing a high-efficiency flexible device.

Bade et al. compared several properties of flexible printed perovskite LEDs on rigid ITO/glass substrate and carbon nanotube (CNT)/polymer substrate[18]. Device is consisted ITO or CNT electrodes used as transparent anode, a printed perovskite film used as emissive layer and, printed silver nanowire (AgNW) used as cathode. Structure and images of emitted device on CNT/polymer substrate were shown in Figure 2.4. Best performance of device on ITO /glass substrate was maximum luminance intensity (L_{max}) of 12,014 cd m^{-2} and maximum external quantum efficiency (EQE) of 1.1%. On the other hand, Device on CNT/polymer substrate had lower performance EQE of 0.14% with L_{max} of 360 cd mm^{-2}. Despite low efficiency of device on CNT/polymer substrate, device was bent to 5 mm without affecting the characteristic of the device.
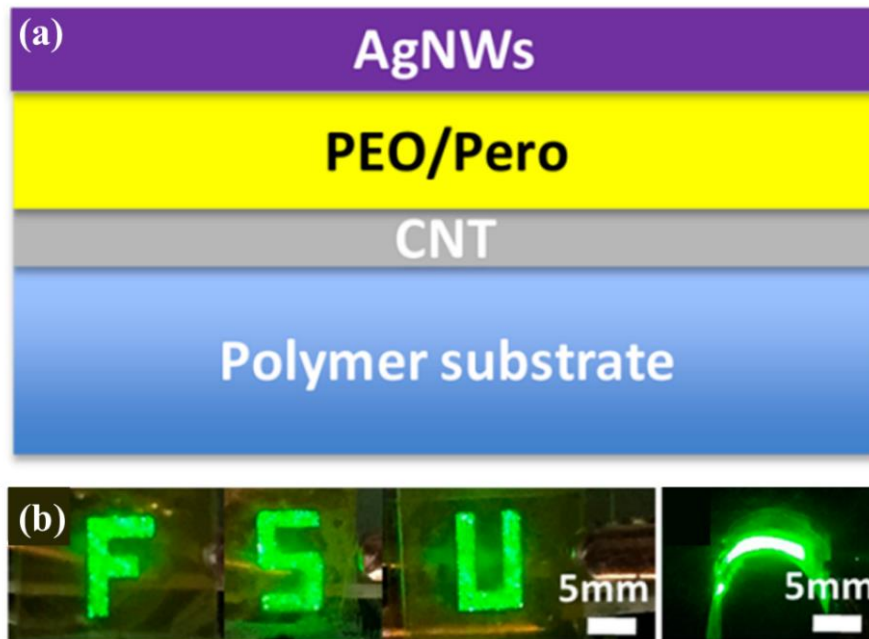
Figure 2.4. Schematic of flexible perovskite LEDs using carbon nanotube/polymer substrate. (b) Images of emitted device at flat and bending state[18].

Bade et al. also demonstrated intrinsically stretchable perovskite LEDs consisting methylammonium lead tribromide (MAPbBr$_3$) and poly(ethylene oxide) (PEO) used as emissive layer[19]. Device consisted PEDOT:PSS modified using PEO used as transparent and flexible anode, eutectic indium-gallium (EInGa) as anode, and emissive layer. Devices had a brightness of 15.960 cd m^{-2} at 8.5V and maximum external quantum efficiency of 0.62%. Device was not affected by stretching. Current efficiency was 2.7, 2.9, 3.2 cd A^{-1} at 0, 20, 40% strain, respectively. However, luminance decreased from 2887 cd m^{-2} to 583 cd m^{-2} at 4V during 100th stretching cycles. Graphs and images of stretchable perovskite LEDs were shown in Figure 2.5.
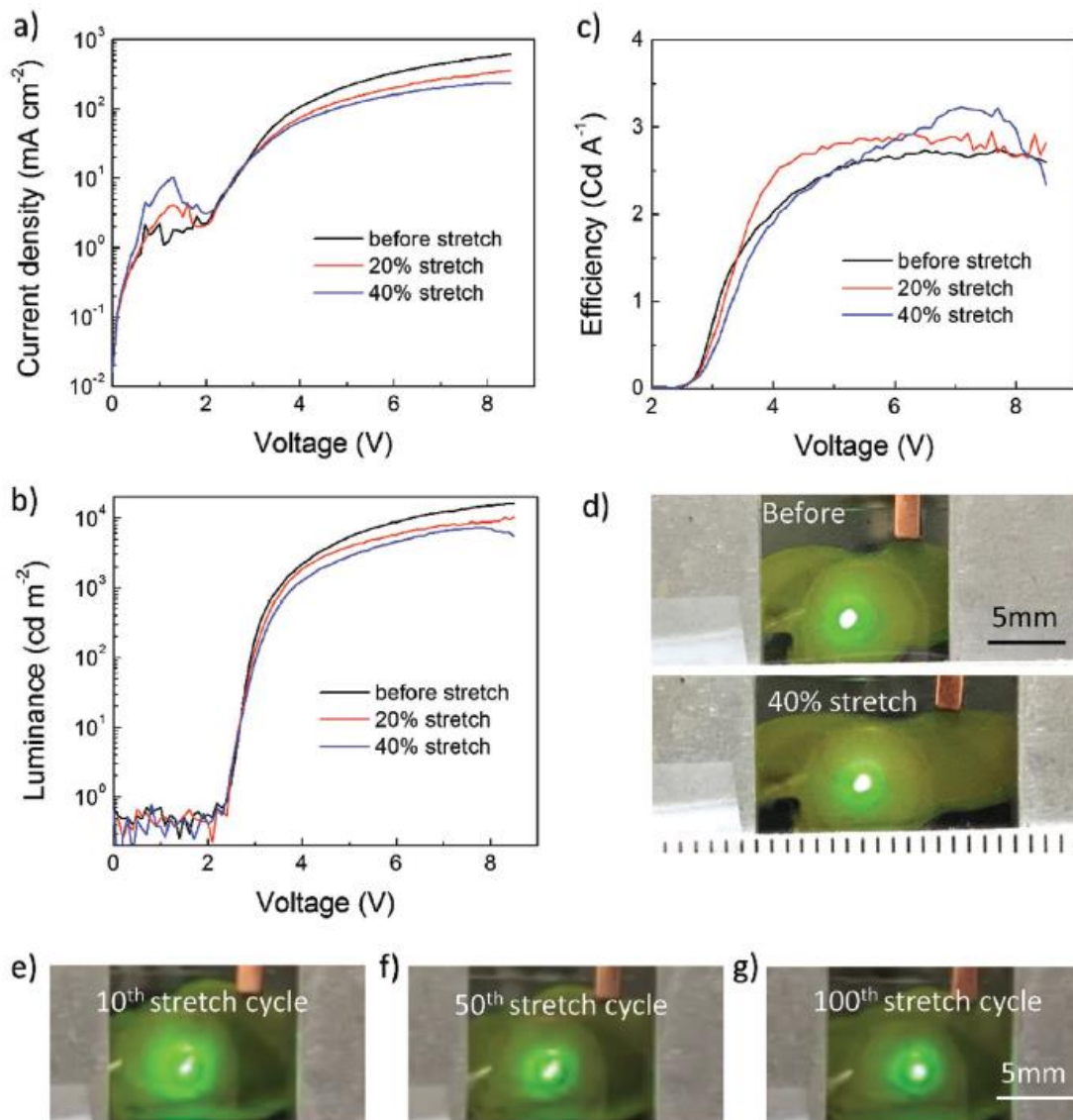
Figure 2.5. (a) Current density versus voltage, (b) Luminance versus voltage, (c) efficiency versus voltage characteristics of stretchable PLEDs before and after 20, 40% bending. (d) Images of emitted perovskite LEDs at 0 and 40% strain. (e-g) images of emitted perovskite LEDs after 10, 50, 100th cyclic stretched[19].

Seo et al. reported highly efficiency ITO-free flexible perovskite LEDs based on graphene anodes[20]. Device consisted four-layer graphene, PEDOT:PSS , perfluorinated ionomer (PFI), MAPbBr$_3$. They modified MAPbBr$_3$ emission layer using additive based nanocrystal pinning due to overcome low device efficiency. Images of device structure and emitted device were shown in Figure 2.6 (a) to (c). Perovskite LEDs on ITO anodes were also fabricated with higher maximum current efficiency 10.6 cd A^{-1} and external quantum efficiency 2.2%. Perovskite LEDs on graphene anodes showed higher maximum current efficiency as 18.0 cd A^{-1} and external quantum efficiency as 3.8% than perovskite LEDs on ITO anode. Since the graphene electrode excludes the negative effects of the ITO electrode in terms of exciton quenching, the efficiency is high. After 1200 bending cycles with 1.34% strain, Current density of perovskite LEDs on graphene electrode decreased by 81% from initial current density. However, Current density of perovskite LEDs on ITO electrode decreased by 64% from initial current density after 200 bending cycles and failed completely after 1200 bending cycles due to brittleness of ITO electrode. Graphs of efficiency of perovskite LEDs were shown in Figure 2.6 (d) to (f).

Zhao et al. introduced effect of bulky organo-ammonium halides on grain size and surface roughness of perovskite layer[21]. Bulky organo-ammonium halides lead to smooth surface of perovskite films with small crystal size due to confine crystal growth of perovskite. Authors used five different additives such as butylammonium iodide (BAI), dodecylammonium iodide (DDAI), benzylammonium iodide (PMAI), phenethylammonium iodide (PEAI), and 4-flurobenzylammonium iodide (FPMAI). Additives had different chain length and molecular size. The additives adjusted the grain size and surface roughness of perovskite according to the chain length and molecular weight. Authors demonstrated trade-off between optical properties and mechanical properties depending on tuning alkyl chain length of additives. Trade-off was overcome by increasing polarity of additives using electron-withdrawing groups. Flexible perovskite LEDs recorded high external quantum efficiency as 13%. Efficiency degradation did not observe after 10,000 bending cycles at bending radius of 2 mm. However, external quantum efficiency perovskite LEDs maintained by 80% of initial value after 10,000 bending cycles at bending radius of 1 mm. Characterization of flexible perovskite LEDs were presented in Figure 2.7.

Many researchers have developed a flexible perovskite light emitting device through evaluation of flexible electrodes and modification of perovskite layer. Flexibility of the device was evaluated using the change in efficiency of the device under repeated bending at various bending radius. However, there has been no any analytical and systematical studies on flexible perovskite LEDs for analyzing the mechanical properties of each component layer, in order to determine which layer is the weakest under mechanical bending.
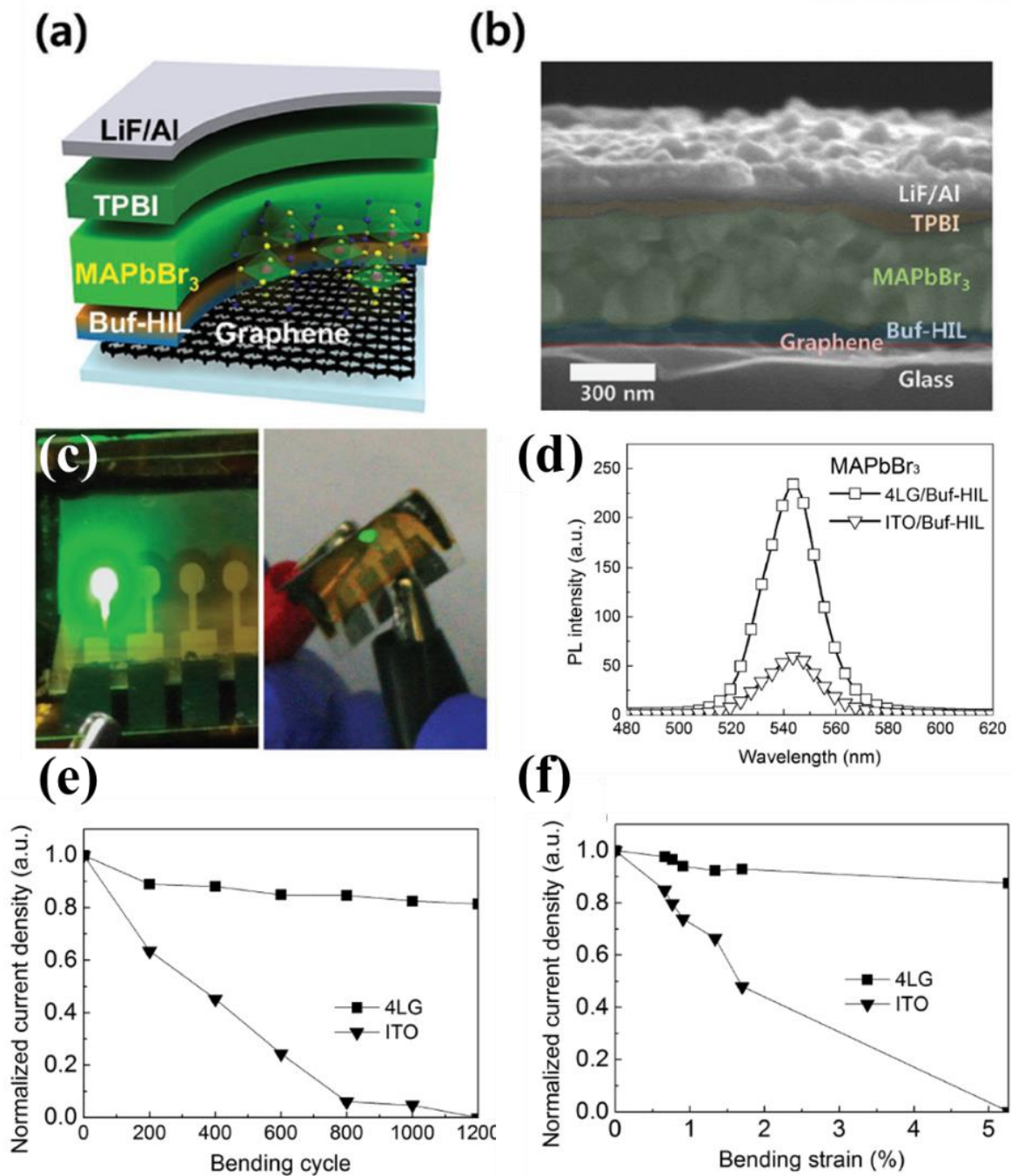
Figure 2.6. (a) Schematic and (b) cross-sectional images of perovskite LEDs on graphene anode. (c) optical images of emitted perovskite LEDs at flat and bending state. (d) Steady-state photoluminescence spectra of MAPbBr$_3$ film on graphene and ITO anode. (e-f) Normalized current density of graphene and ITO anode according to (e) bending cycle at bending strain 1.34% and (f) bending radius[20].
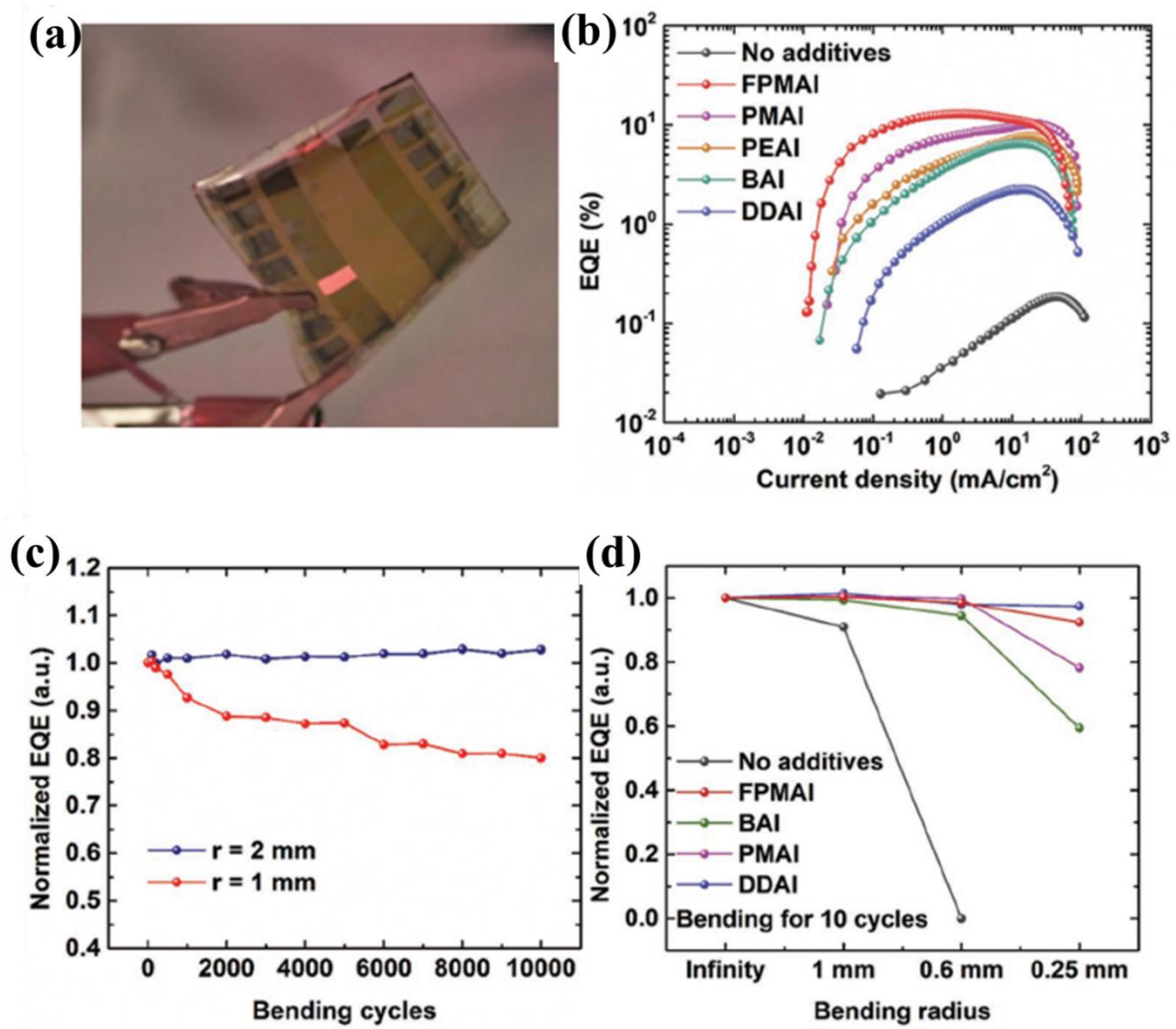
Figure 2.7. (a) Photo of emitted flexible perovskite LEDs with FPMAI additives. (b) EQE versus current density curves of perovskite LEDs. Normalized EQE depending on (c) bending cycles at bending radius of 1 and 2 mm. (d) bending radius after 10 bending cycles[21].

2.3 Previous research for mechanical properties of perovskite

Various types of highly flexible and semitransparent electrodes have been used for making flexible devices. However, critical requirement exists to fabricate flexible and semitransparent perovskite LEDs (FSPeLEDs) because appropriate solvent and processing temperature should be considered to coat flexible and transparent top electrode without the damage of perovskite film or other component layers. Unlike materials used for replaceable electrodes and substrates, perovskite has several advantages as an active material for LEDs. The perovskite is expected to be low in elastic deformability than other constituent materials used in perovskite LEDs due to high crystallinity[1, 11, 22]. The flexibility of perovskite LEDs has been studied extensively by experimental methods such as optical characterization under cyclic bending deformation, flexural properties of perovskite used in LEDs has not been studied.

As shown in Figure 2.8, crystal structure of perovskite compounds. Mechanical properties of perovskite depend on crystal structure and directional. Mechanical properties of perovskite have been studied extensively in various measurement method. Polycrystalline perovskite thin films easily degraded by reaction with moisture in the air. It is difficult to measure mechanical properties in external environment. Mechanical properties analysis has been carried out on single crystalline perovskite. Single crystalline perovskite was fabricated in the ambient conditions by anti-solvent evaporation method. The fabricated samples showed no significant degradation in air. The elastic modulus of single-crystalline $MAPbBr_3$ was determined to be 29.1 GPa based on density functional theory (DFT) calculations and 28.3 and 30.2 GPa using a laser ultrasonic technique[23-25]. Using nanoindentation measurements, the elastic modulus of single-crystalline $MAPbBr_3$ was determined to be 19.6 GPa and 17.7 GPa while its hardness was determined to be 0.36 GPa and 0.31 GPa[26, 27]. The images related to laser ultrasonic technique and nanoindentation were shown in Figure 2.9 and 2.10, respectively.

The mechanical properties of single-crystalline perovskite may be different from those of the perovskite used in thin-film form in PeLEDs, since the microstructure of perovskite thin films is highly dependent on the chemical composition and the fabrication process used[28, 29]. Thus, based on only the elastic modulus of perovskite as determined by DFT calculations and the laser ultrasonic technique, it is not possible to evaluate the flexibility of perovskite materials. Even though nanoindentation measurements allow one to determine the elastic modulus and hardness, the nanoindentation depth should be limited considering the thickness of the perovskite layer. This means that the elastic modulus and hardness as measured by nanoindentation would only be reflective of the local volume and would not represent the actual mechanical properties of the entire perovskite layer. However, the best way of evaluating the flexibility would be to perform uniaxial tensile tests on free-standing perovskite layers prepared using the same procedure as those used for the device itself. This would allow the stress and strain values corresponding to the onset of plasticity and fracture in the uniaxial stress to be determined and also allow the deformation and fracture behavior in the complex stress state to be evaluated based

on continuum mechanics.
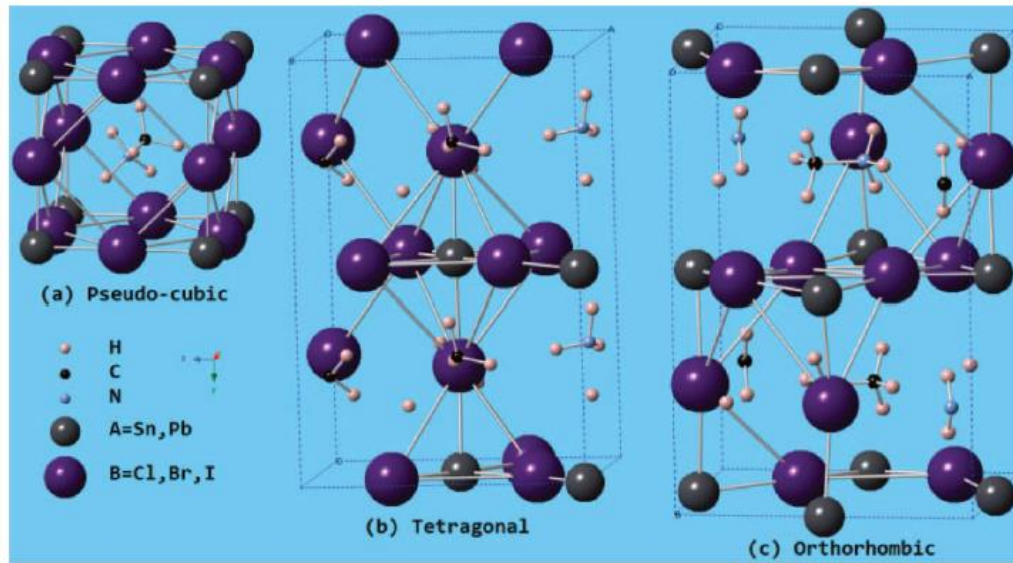
Figure 2.8. The crystal structure of $CH_3NH_3BX_3$ (B=Sn, Br; X=Br, I) perovskite compounds[23].
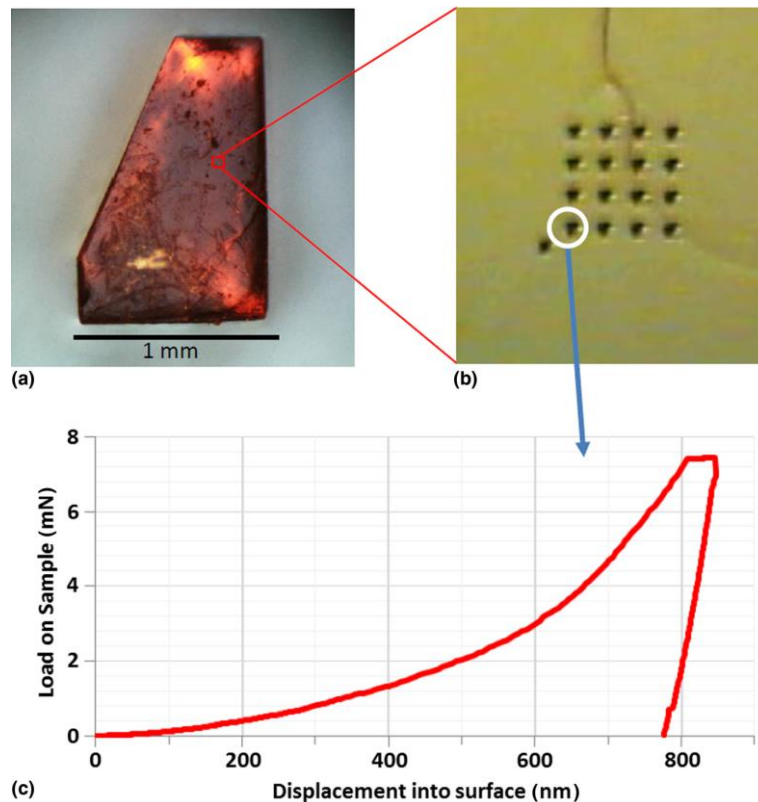
Figure 2.9. Image of single-crystal perovskite ($CH_3NH_3PbBr_3$) presenting (100) face and (b) image after indentation test. (c) Typical nanoindentation load-displacement curve on single-crystal $CH_3NH_3PbBr_3$[26].
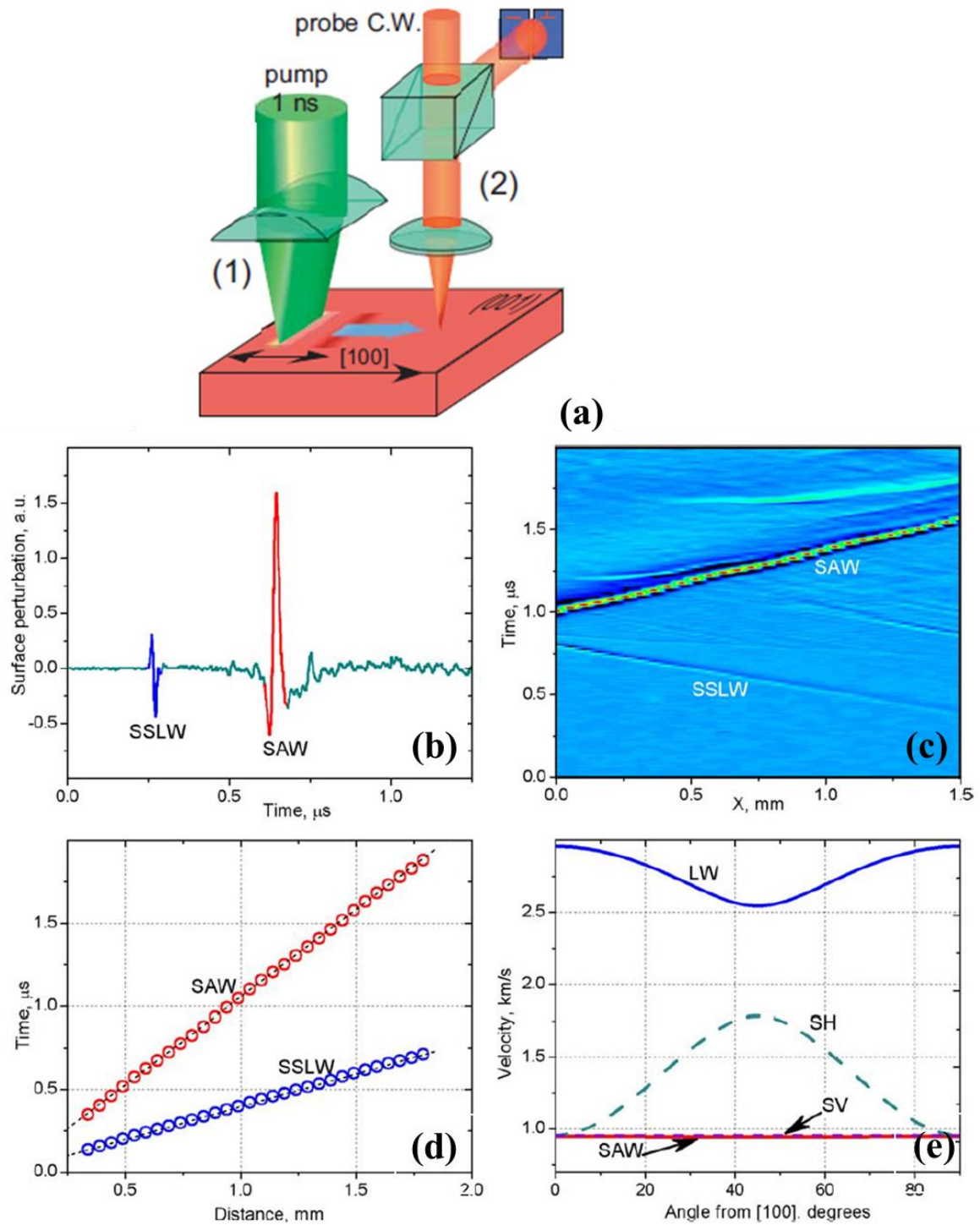
Figure 2.10. (a) Schematic of measurement equipment. (1) pulsed laser operating, and (2) C.W. laser. (b) Typical signal of two acoustic waves. (c) Scan along wave propagation direction. (d) Time versus displacement graph of wave. (e) Acoustic modes on (001) surface calculated from the extracted elastic modulus[24].

Table 2.1. Mechanical properties of perovskite (MAPbBr$_3$).

Composition (Crystallinity)	Phase	Testing method	Young's modulus (GPa)	Hardness (GPa)	Ref.
	Cubic	Density function theory	29.1		23
	Tetragonal		15.1		
	Cubic (100)	Nanoindentation	17.7	0.31	27
	Cubic (110)		15.6	0.26	
CH$_3$NH$_3$PbBr$_3$ (single crystal)	Cubic (100)		19.6	0.36	26
	Cubic (100)	Lase ultrasonic technique	28.3		24
	Cubic (110)		11.7		
	Cubic (100)		30.2		25
	Cubic (111)		11		

2.4 Deformation behavior of multi-layer structure

LEDs are manufactured in the form of multilayer structure with various constituent materials in thin film. If bending deformation occurs, the compressive and tensile strain are different depending on distance from neutral plane. When all components deformed in elastic deformation range, they return to original state by elastic recovery when external force is removed. When a specific component undergoes plastic deformation, interfacial separation phenomena such as wrinkle or delamination are generated, and the efficiency is decreased. If breakage occurs in the device, a problem occurs in driving the device itself. In order to ensure the durability of the device, all components must be deformed within the elastic deformation range. Schematics of deformation behavior were shown in Figure 2.11.
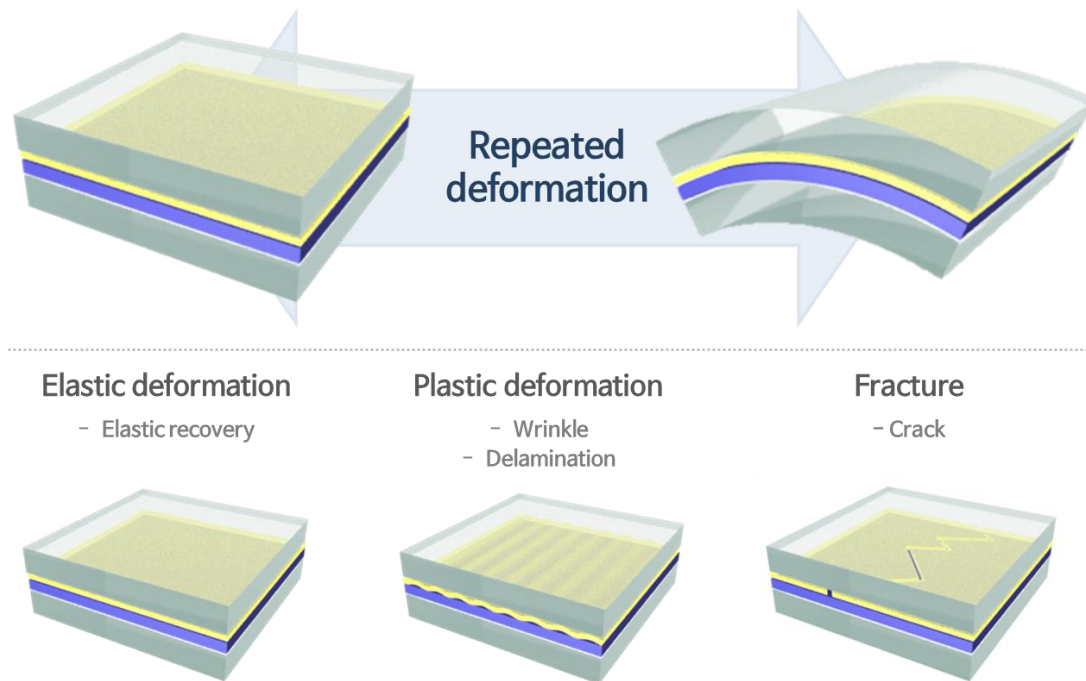
Figure 2.11. Schematic illustration of deformation behavior of multi-layered element depending on deformation behavior of constituent materials.

The strain acting on each component during bending deformation is determined by the distance from the neutral line in the device[30, 31]. Based on the neutral line, tensile strain is applied to the outside and compressive strain is applied to the inside. On the neutral line, strain is canceled and does not work. When there is only one layer on a thick substrate, generally half of the thickness of the substrate is regarded as a neutral line. In the case of the multi-layer structure, the position of the neutral line changes due to the different elastic modulus, Poisson ratio and thickness of each constituent materials.
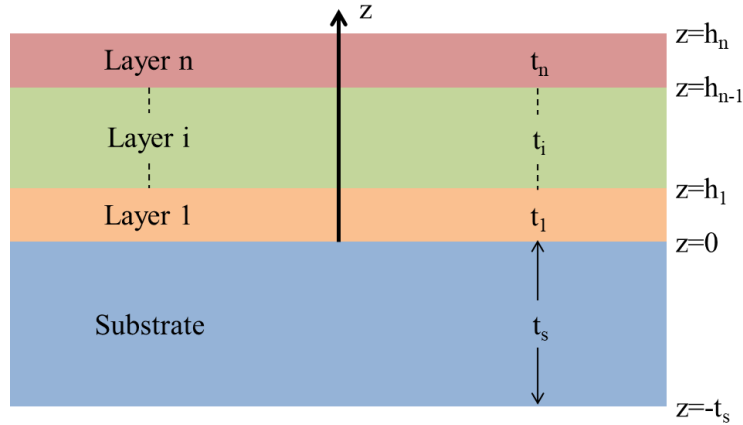
Figure 2.12. Schematic showing a multilayer strip and coordinate system.

Multilayer is schematically shown in Figure 2.12. The n layers individually have thickness t_i and are attached to a substrate having a thickness t_s. The subscript i is determined by the number of thin films in the range from 1 to n. Layer 1 is attached to top surface of substrate. The reference of the z-axis is set at the interface of the substrate with one layer, and the bottom surface of the substrate is expressed as $z = t_s$. The free surface of the top layer is represented by $z = h_n$ and the interface between i and i + 1 layers is represented by $z = h_i$. In the multi-layer structure, the distribution of strain is expressed by the expression

$$\varepsilon = (z - t_n)/r_b, \tag{2.1}$$

where t_n is location of neutral axis and r_b is bending radius of multi-layer structure. Stress/strain distribution in multi-layer structure, resultant force generated by the bending strain component is zero, the following equation is satisfied.

$$\int_{-t_s}^{0} \frac{E_s(z-t_s)}{r} dz + \sum_{i=1}^{n} \int_{h_{i-1}}^{h_i} \frac{E_i(z-t_s)}{r} dz = 0, \tag{2.2}$$

Solutions of Equation (2.1) and (2.2) yield

$$t_b = \frac{-E_s t_s^2 + \sum_{i=1}^{n} E_i t_i (2h_{i-1} + t_i)}{2(E_s t_s + \sum_{i=1}^{n} E_i t_i)}, \tag{2.3}$$

In the following section, the distance from the position of neutral axis (t_b) to bottom surface of layer was set to d_n. The strain acting on the top surface of each layer of the LEDs element was calculated using the following equation as

$$\varepsilon = \frac{d_n + d_f}{r}, \tag{2.4}$$

where d_n is distance between neutral plane to bottom surface of film and d_f is thickness of films equal to t_i.

16

2.5 Encapsulation OLEDs

Organic light-emitting diodes has developed rapidly in recent few decades with much attention due to their several advantages[32-35]. Organic light-emitting diodes is easily degraded by atmospheric moisture and oxygen by various method[36-43]. Encapsulation of organic light-emitting diodes is necessary to prevent moisture and oxygen in atmosphere. Thus, lifetime of device is determined by permeation rate of encapsulation materials produced at end of device fabrication process. Required barrier properties of various application were presented in Figure 2.13[44].
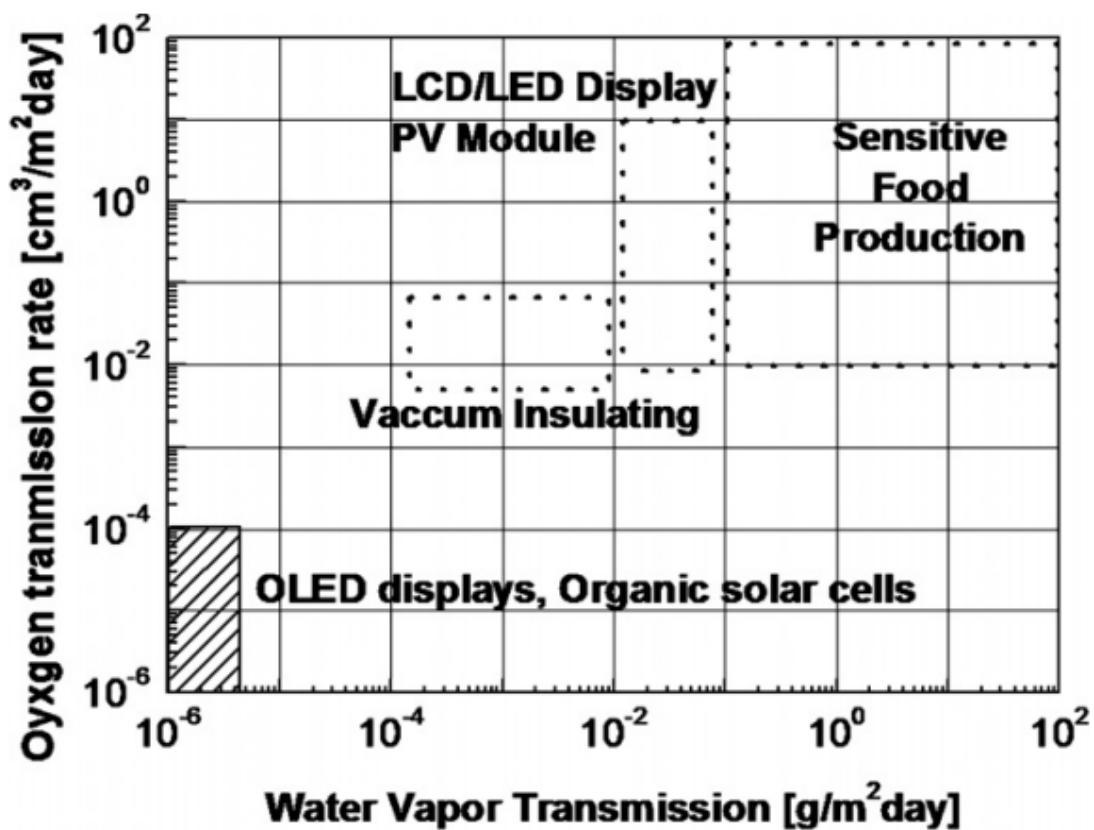
Figure 2.13. Barrier requirements for different applications[44].

Schaer et al. demonstrated that moisture is thousand times more effective than oxygen at room temperature by analyzing the degradation mechanism of OLEDs[40]. In general, Pinhole in cathode was formed by dark particles deposited during fabrication process. The water vapor penetrated through pinhole in cathode, diffused to interface between cathode and emission layer, and generated hydrogen gas by interaction with cathode. Because of pressure of hydrogen gas, bubble was created, and water vapor was transferred through bubble faster than diffusion. In the end, the bubble burst and created an additional water infiltration path. Related images were shown in Figure 2.14.
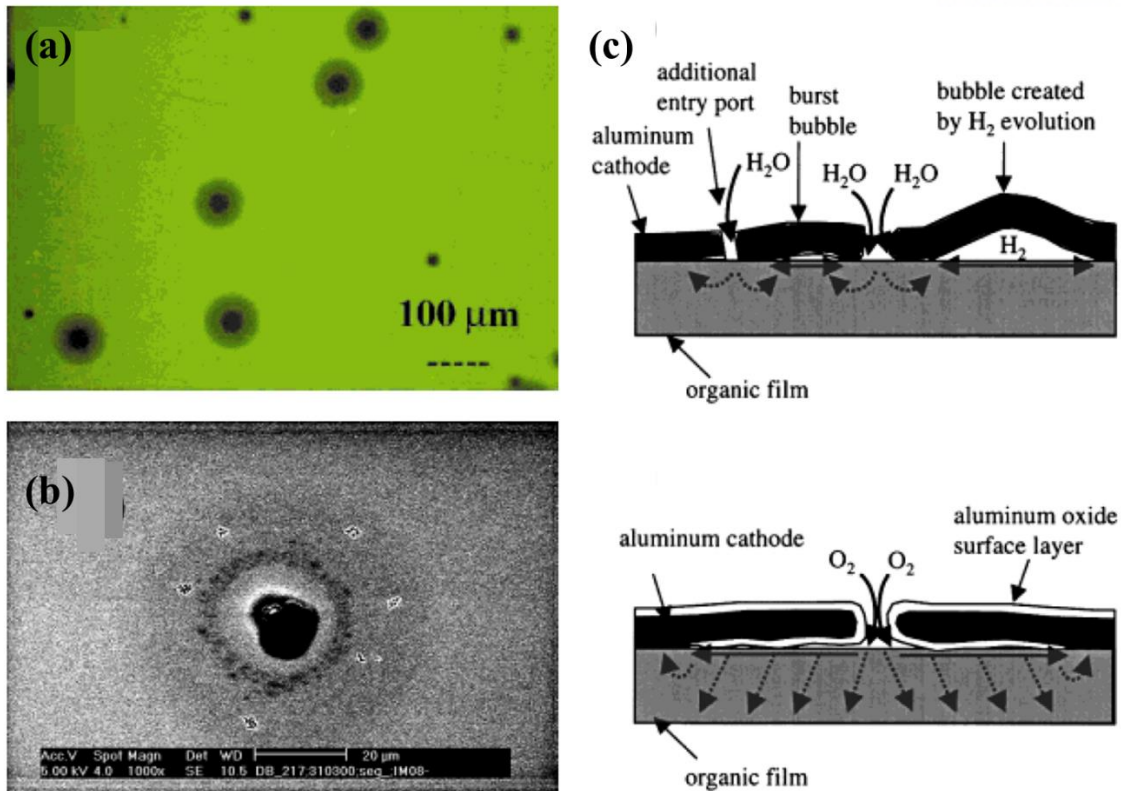
Figure 2.14. (a) Optical microscopy image of OLED working under pure oxygen atmosphere. Dark spots are composed of a black core (b) SEM image of aluminum cathode surface on which a black spot has formed under operation in a pure oxygen atmosphere. (c) Mechanism of dark spot formation during operation of an OLED under (upper) water vapor and (lower) pure oxygen atmosphere[40].

Generally, many light-emitting diodes are manufactured based on a rigid substrate. In this case, glass or metal lid is used as an encapsulating material by attaching to a device[45, 46]. Although glass increases the thickness of the device and eliminates the mechanical flexibility of the device, it completely prevents the penetration of moisture and oxygen due to excellent permeation properties. Structure of encapsulated rigid device was shown in Figure 2.15 (a)[47]. Glass was used as substrate and ITO layer used as anode was coated on substrate. Organic layer used as emission layer and top electrode were deposited on ITO layer. The fabricated device was transferred to a glove box in a nitrogen atmosphere. Lastly, glass or metal lid was attached on top of device using epoxy adhesive. The empty space between encapsulation material and top electrode was filled with nitrogen gas. In some case, several desiccants are used to absorb residual water[48].

However, in the case of encapsulation technique using rigid materials, there are some problems to be applied to the flexible devices which have been studied extensively in recent years. As shown in Figure 2.15 (b) and (c), it is much more effective to use the thin film encapsulation technology for the flexible device[47]. However, in the case of a single thin film, the moisture barrier properties are limited due to

the pinholes generated during the deposition process. Jamieson et al. deposited a 10 to 100 nm thick aluminum films on polyester using vacuum deposition method and measured barrier properties of aluminum layers[49]. Measured barrier properties have linear relation with density of pinhole defect on aluminum thin films. On the other hand, it has no relation with thickness of aluminum thin films. The main cause of degradation of barrier properties was pinhole generated by dust particle on polyester substrate during deposition process.
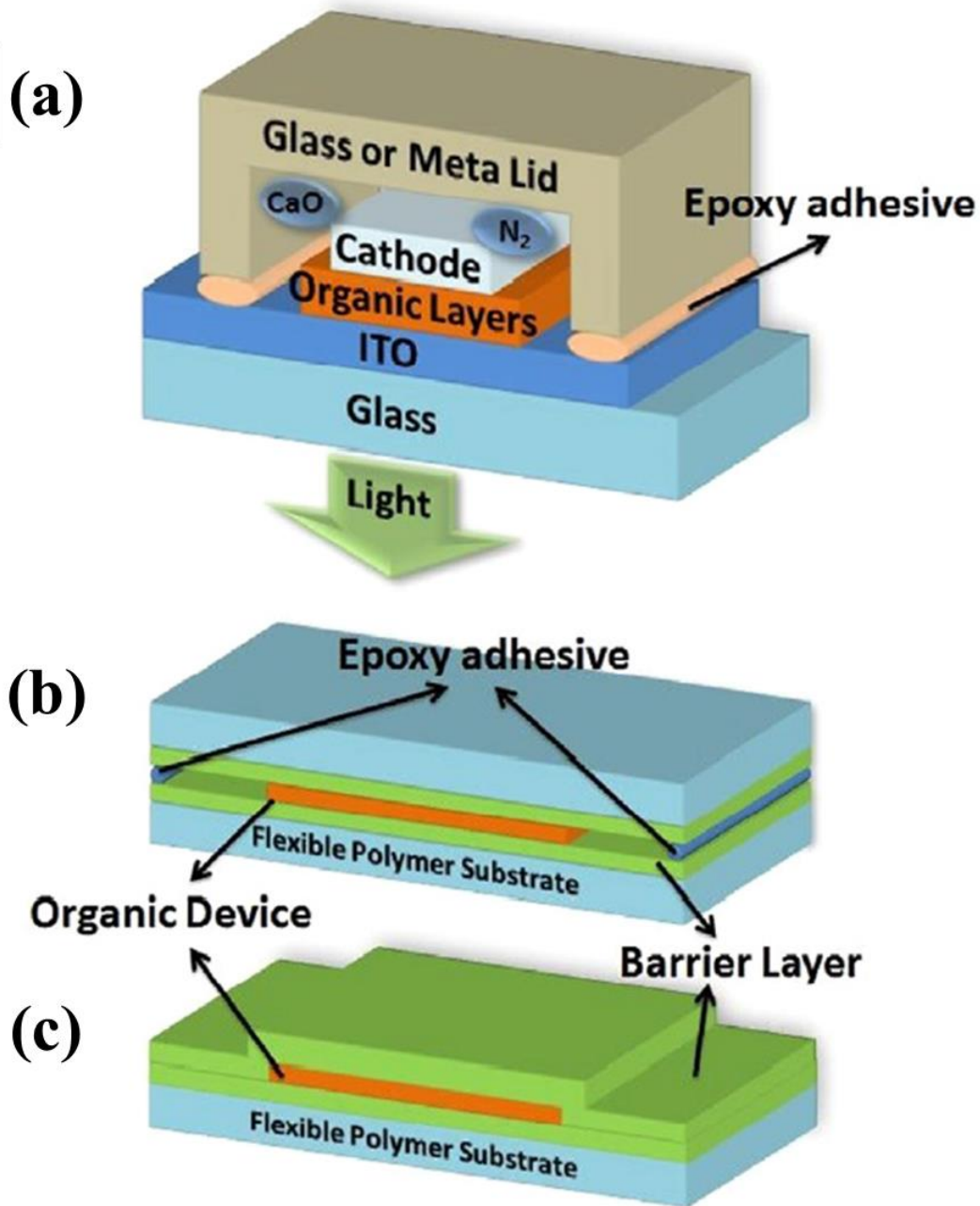
Figure 2.15. (a) Schematic side view of encapsulated OLED with traditional encapsulation, (b) coated flexible lid, and (c) thin-film[47].

In order to improve barrier properties, many researches have been carried out to deposit the organic material between the inorganic materials[50-52]. Multilayer structure was shown in Figure 2.16. There are two reasons why inorganic and organic hybrid encapsulation material has better barrier properties than single encapsulation thin film. The first is that the organic layer increases the penetration path of water permeation. The second is that the nanolaminates prevent the defects from spreading throughout the multilayer structure. Both characteristics are associated with improved barrier properties of encapsulation films[53, 54]. On the other hand, the multilayer structure limits the transmission of light due to inherent absorption of component materials and interference effect between constituent materials in multi-layer structure[55, 56]. The interference effect changes the color balance by reducing the light emission of the OLED devices. In order to have sufficient encapsulation performance and maximum highest light transmittance simultaneously, the multi-layer structure should be designed considering optical performance of constituent materials.
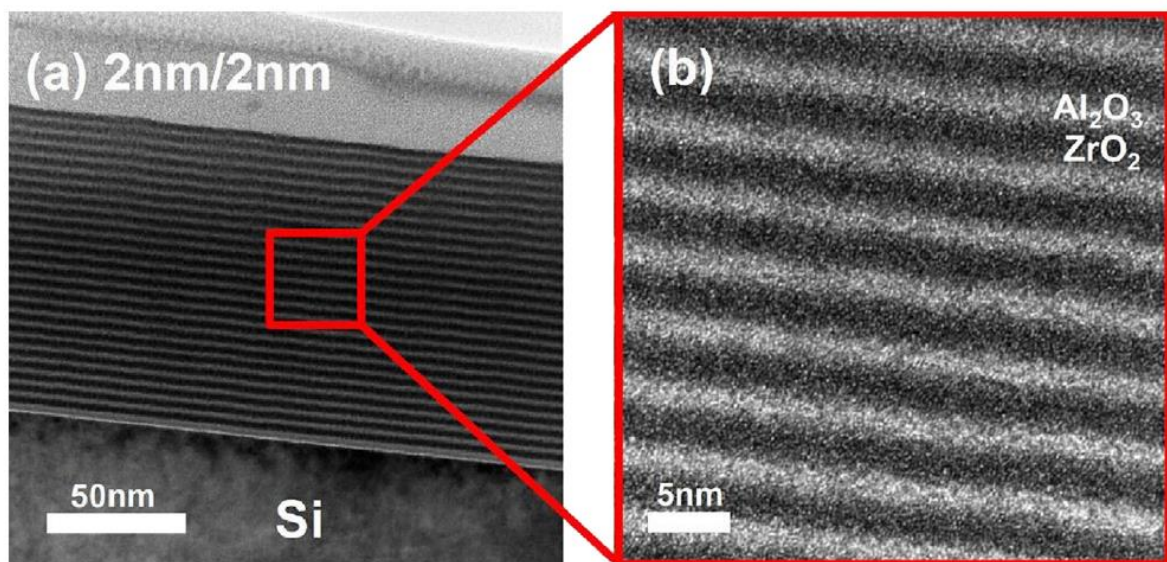
Figure 2.16. Cross sectional TEM images of 2nm/2nm multi-layer at (a) low resolution and (b) high resolution[47].

2.6 Stretchable substrate of OLEDs

Glass and silicon are representative substrates used in light-emitting diodes. However, due to the rigid nature of the substrate, it is impossible to use it in a flexible device. PDMS is widely used as a substrate material for flexible devices. Generally, devices are fabricated by transferring devices made from rigid substrates to flexible substrate. Another method is to mount the device on a PDMS substrate to ensure the flexibility of the device. As shown in Figure 2.17, island type device mounted on substrate was not deformed, and the deformation concentrated only on the elastomer substrate between island type devices[57].

In addition, PET, NOA, PDMS. Polyurethane, and Eco-flex have also been studied extensively for highly stretchable substrate materials. As shown in Figure 2.18, polyurethane substrates stretched up to 400% with carbon nanotube layer and Eco-flex substrates stretched up to 460% with silver nanowire[58]. Research has also been conducted on the effect of elastic substrates of stretchability. Vijay et al. coated PEDOT:PSS on various substrate materials such as PDMS, PMMA, SEBS, and rubber substrates and evaluated stretchability of substrates[59]. As show in Figure 2.19, Experimental results show that cracks and delamination occurred in most substrates with a strain of 2 to 5%, but SEBS deformed to 28% without cracks on PEDOT:PSS due to van der Waals interaction between SEBS substrate and PEDOT:PSS. Thus, when a flexible device is selected in accordance with the purpose and application, enough flexibility can be secured.

Polymer substrates provide higher deformation characteristics compare to glass and metal substrates, but do not provide resistance of moisture and oxygen permeation. devices are manufactured by transferring manufactured devices to a substrate. The moisture and oxygen permeability of commonly used polymer substrate materials is summarized in Table 2.2[48]. Due to the low humidity resistance of the polymer substrate, the device is easily deteriorated and is not functioning. In order to be used as a substrate of an OLED device, moisture resistance through addition of layers must be ensured [60, 61].

In addition, unlike glass substrates, polymer substrates are not polished and there is a problem of depositing devices directly because of roughness[62]. The thickness of the organic layer used in the OLED device is 100-200 nanometers, but surface roughness of commonly used PET substrate due to thermal stability is more than 150 nm. Therefore, planarization is required to use a polymer substrate having a smooth surface for device stability.

Since various considerations such as thermal stability, Young's modulus, chemical resistance, dimensional stability, moisture permeability, and elastic limit for use as substrates for OLEDs must be regarded, additional research of polymer substrates is required depending on the purpose and function for stretchable substrate of OLEDs.
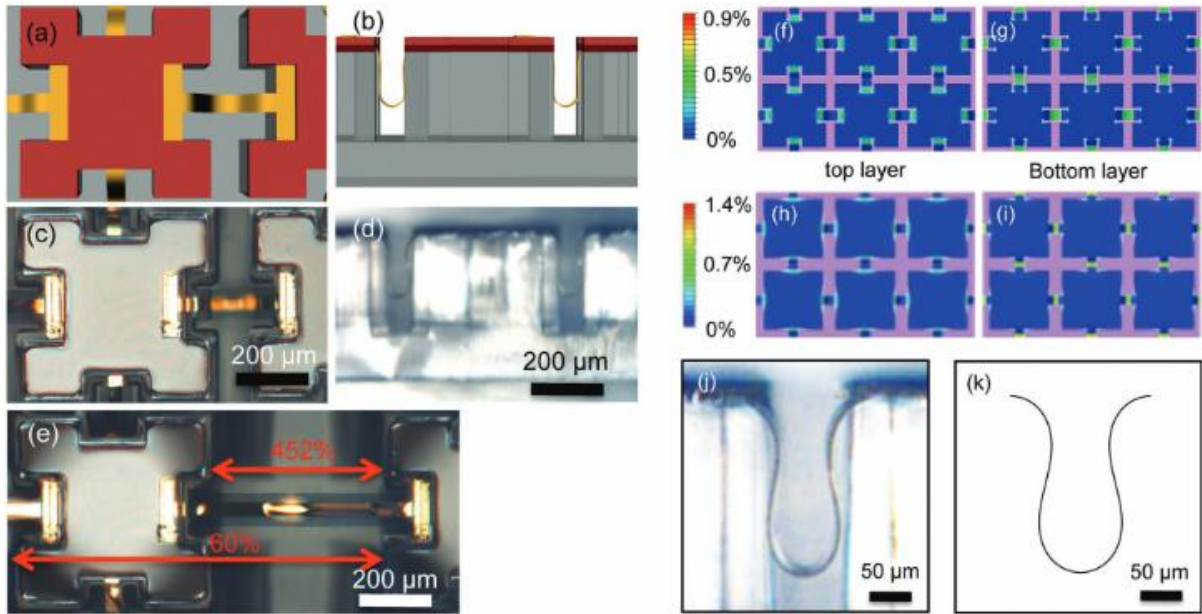
Figure 2.17. Schematic illustration of stretchable GaInP/GaAs photovoltaic modules, optical microscopy, and FEM results[57].
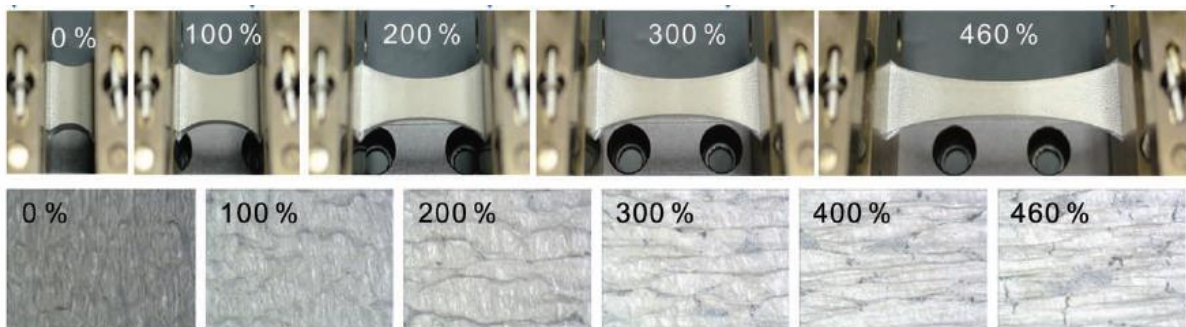
Figure 2.18. Surface images of electrode on pre-strained Eco-flex during stretching process[58].
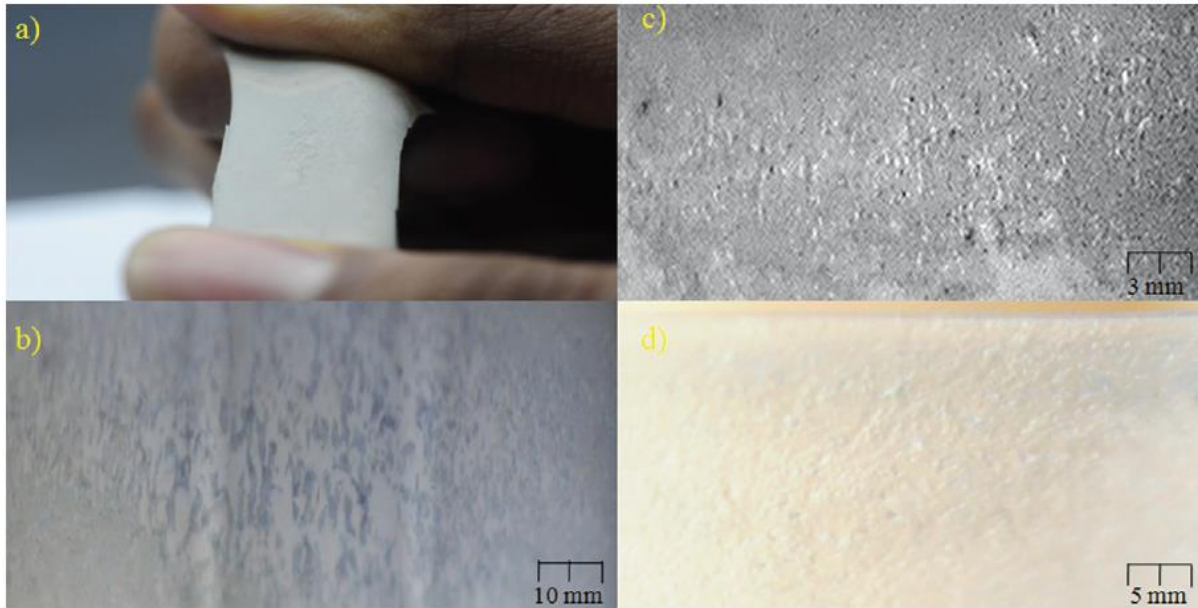
Figure 2.19. (a) Stretched image of PEDOT:PSS coated natural rubber substrate. Surface imager of PEDOT:PSS coated on (b) natural rubber substrate, (c) nitrile rubber, and (d) SEBS substrate during stretching[59].

Table 2.2. WVTR and OTR for various polymer materials as flexible substrate[48].

Polymer	WVTR (g/m/day) (37.8-40℃)	OTR (cm3/m2/day) (20-23℃)
Polyethylene	1.2-5.9	70-550
Polypropylene (PP)	1.5-5.9	93-300
Polyester (PS)	7.9-40	200-540
Poly ethylene terephthalate (PET)	3.7-17	1.8-7.7
PEN	14	0.04
Polyimide	7.3	3.0
15 nm Al / PET	0.4-21	0.04-17
SiO$_x$/PET	0.18	0.2-2.9
OLED requirement	1×10^{-6}	$1 \times 10^{-5} - 1 \times 10^{-3}$

2.7 Previous research for mechanical properties of silica thin films

Silicon dioxide thin films have been used in various fields such as microelectronic, optical, packaging industry for many years due to their various excellent properties such as corrosion resistance, optical transparency, and hardness. Since the silicon dioxide thin film is used in various areas, a high-quality silicon dioxide thin films should always be prepared in accordance with the purpose. The silicon dioxide thin film can be deposited by various methods such as physical vapor deposition (PVD, evaporating deposition sputtering deposition), chemical vapor deposition (CVD, traditional chemical vapor deposition, plasma enhanced chemical vapor deposition), sol gel method, and oxidation method.

Since silicon dioxide has various manufacturing processes, a thin film is formed under various conditions such as temperature, source, and environment. Different chemical reactions occur depending on the production environment and thus the quality of the thin film is changed. As simple example of the thermal evaporation method, the growth rate and chemical reaction of silicon dioxide are different between the dry oxidation method which is performed at 1000-1200°C using oxygen and the wet method which is made at 900-1000°C using moisture. Due to the slow production rate and few impurities in the manufacturing process, the dry thermal oxidation method has good density and quality.

The mechanical properties of the silicon dioxide thin films deposited by various methods have been studied in order to suit the purpose. The previously studied mechanical properties of silicon dioxide are summarized in Table 2.3. Though silicon dioxide can be manufactured by various methods such as nanowires, aerogels, and thin films depending on the use environment. Only the thin film form of silicon dioxide having thickness of nanometer to micrometer has been summarized. Mechanical properties were measured by various method such as bulge, nanoindentation, tensile test, cantilever bending, torsion test, and non-linear finite deformation theory. The image of the measurement method is summarized in Figure 2.20[63-65].

In most of the results, the silicon dioxide thin film shows brittle fracture behavior without plastic deformation. Tensile strength of bulk scale silicon dioxide thin films is known to be several hundreds of megaPascal depending on the manufacturing process[66]. Tensile strength of micrometer thick silicon dioxide thin film is 10 times higher than that of bulk scale silicon dioxide. The Elastic modulus is in the range of 60 - 70 gigapascals, similar to bulk materials, depending on the deposition method. Many researchers have studied the effect of fracture strength on the thickness of silicon dioxide thin films. As shown in Fig 2.21, though there was a slight increase in the breaking strength as the thickness decreased due to Weibull size effect, there was no significant effect of thickness on fracture strength regardless of the deposition method. On the other hand, measured fracture toughness of PECVD silicon dioxide is lower than that of thermally grown silicon dioxide. When deposited by PECVD, generated hydrogen bond interferes with the inter-atomic bond and the silicon dioxide structure is not formed well. The

mechanical properties of thin films prepared by PECVD process are lower than those of thermally grown thin films.

Although many studies have been made in the past, mechanical properties measured by tensile tests have not been analyzed due to the difficulty of sampling. For use as a structural material, it is necessary to study mechanical properties such as breaking strength and yield strength through tensile test.

Table 2.3. Mechanical properties of silicon dioxide thin films.

Deposition method	Thickness	Young's modulus (GPa)	Fracture strength (MPa)	Residual strength (MPa)	Testing method	Ref.
Thermally grown	1 μm	64.6 ± 3	350 – 489	354	Tensile test Stress relaxation	[67]
	1 μm	74	1850		Tensile test (torsion)	[64]
	0.4 μm	85 ± 13			Bending test	[68]
	1 μm	64			Bending test	[69]
	1 μm	83			Nanoindentation	
	< 2 μm	66			Bulge test	[70]
	2 μm	65.5 ± 2.8		270	Non-linear finite deformation theory	[71]
	2 μm			511	Buckled shape measuring method	[72]
PECVD	0.28 – 2.38 μm	70.6 ± 2.1	3700 ± 130		Bending Nanoindentation ($\sigma = H/3$)	[73]
		67.8 ± 3.5	2067 ± 200			
	1 μm	60.1 ± 3.4	364 ± 57		Tensile test	[74]
	0.65 μm		600 – 1900		Tensile test	[65]
	0.5 μm	59			Bending test	[75]
	0.5 – 2 μm	59 - 82			Nanoindentation	[76]
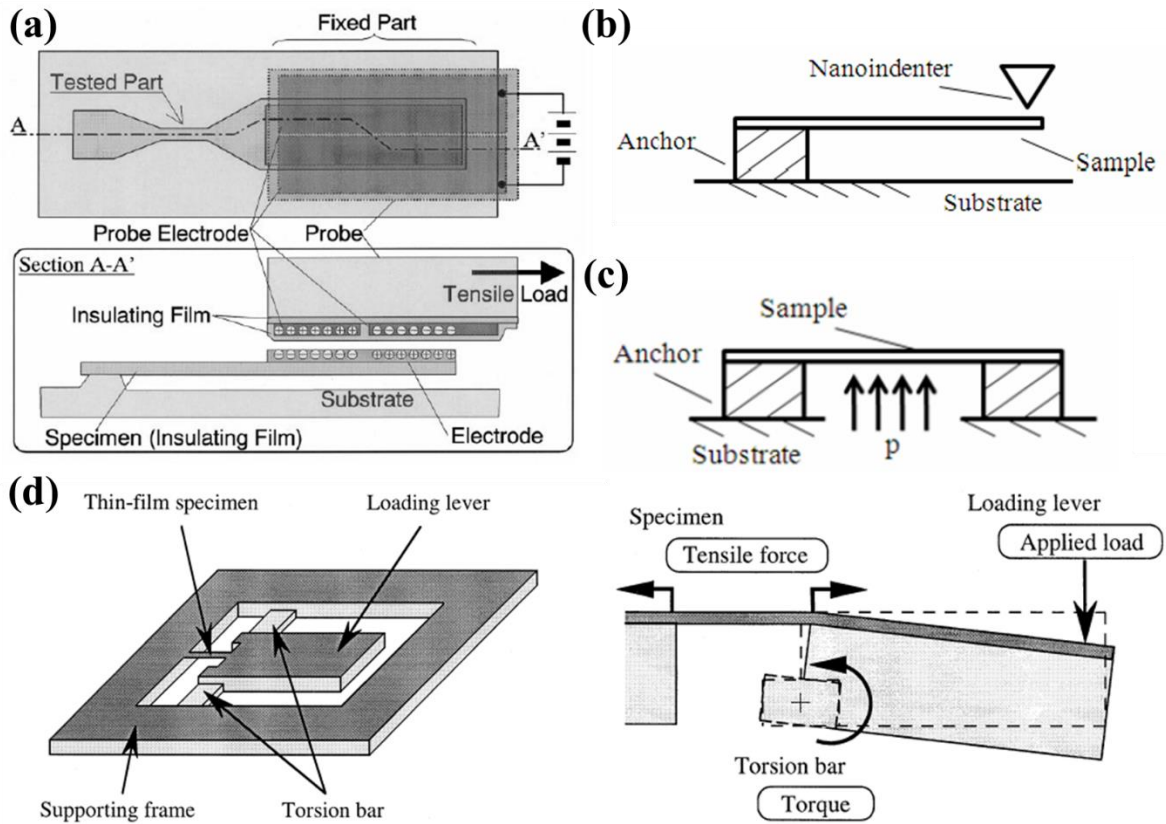
Figure 2.20. Schematics of testing method in previous researches. (a) Tensile test with electrical grip, (b) microbeam cantilever, (c) bulge test, and (d) torsion test[63-65].
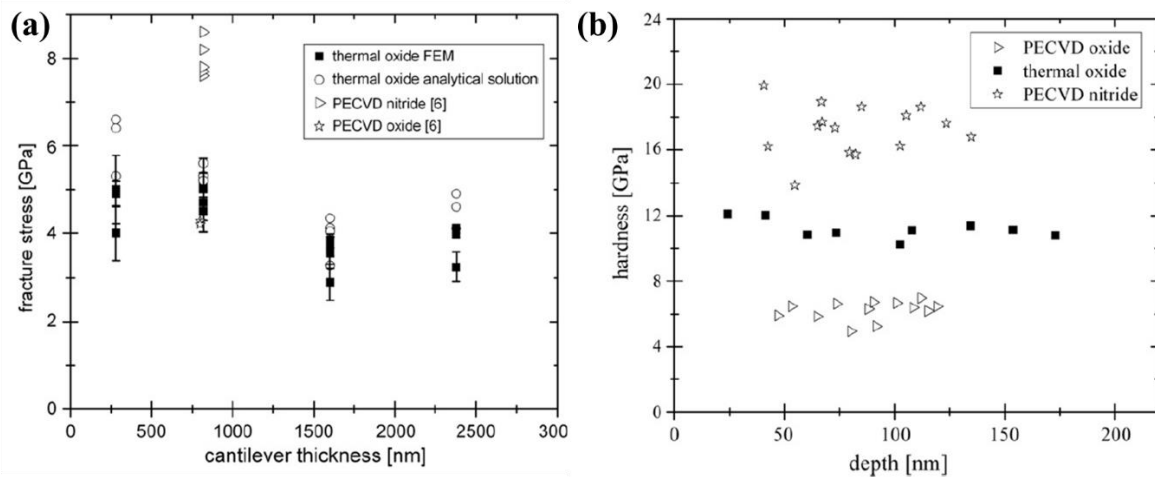
Figure 2.21. (a) Fracture stresses determined by cantilever bending and (b) hardness determined by nanoindentation of thermally grown silicon dioxide, PECVD silicon dioxide and PECVD silicon nitride[73].

2.8 Principle of sol-gel method for silicon dioxide

The sol gel process can be divided into three main methods. Method 1, gelation of colloidal solution. Method 2, hypercritical drying of gel after hydrolysis and polycondensation of alkoxide precursors. Method 3, Aging and drying under ambient condition after hydrolysis and polycondensation of alkoxide precursors. A sol is a dispersion of 1-100 nm solid particles in a liquid, and a gel is a solid network of polymer chains with lengths in excess of micrometers and sub-micrometer-sized pores.

Silica gel is formed by network growth of colloidal particles dispersed in liquid (method 1) or by simultaneous reaction of hydrolysis and condensation polymerization of organometallic precursor to form 3D network (method 2 and 3). If the pore liquid is removed in a gaseous form from the gel network below hypercritical conditions, network of gels does not collapse and forms low density aerogels. The aerogels occupy 98% of the pore volume and the density is as low as 80 kg.m.

If the pore liquid is removed in a gaseous form from the gel network at ambient pressure by thermal evaporation and shrinkage occurs, resulting material is called xerogel. If the pore liquid is alcohol-based, the product is called an alcogel. Gels are defined as dried when the adsorbed water is completely emptied and usually occurs at 100-180 degrees. The surface area of the dried gel is very large (over 400 m^2/g) and the average radius of the pores is very small (below 10 nm). The pore size can be increased by various methods such as thermal treatment, additions of HF to sol, and chemical washing during aging. The dried gel has a lot of hydroxyl on the pores of the surface by chemical adsorption Thermal treatment at range from 500 to 800 degree desorbs hydroxyl and decrease sensitivity of rehydration stress. As a result, gel is stabilized.

When the heat treatment temperature of the gel is increased, the number of pores and the connectivity are reduced due to the sintering of the viscous phase. This process is termed densification. During sintering, the density of gel increases and the porosity fraction decreases. When the pores are completely removed, the porous gel is changed to dense glass. Densification is completed at range from 1250 to 1500 degree for method 1, and at about 1000 degree for method 3. The silica glass fabricated by densification of porous gel has amorphous microstructure and is almost identical in structure and density to silica fabricated by fusing quartz crystal.

Fabrication process of step 1 to 7 for silica glass by sol-gel is described below.

Step 1 : Mixing.

Liquid alkoxide precursor as tetraethyl orthosilicate (TEOS, $Si(OC_2H_5)_4$) is hydrolyzed by mixing with water. The hydrated silica tetrahedra interact to form $\equiv$Si-O-Si$\equiv$ bonds by condensation polymerization.   Condensation polymerization, which is an additional tetrahedra connected, proceeds to form a silicon dioxide network. The moisture released from the reaction remains in pores of network. Hydrolysis and condensation polymerization occurred at multiple sites when the TEOS and H_2O solution begins to mix. The structure density is almost the same as that of fused silica. When sufficient bonding is formed, it becomes colloidal particles or sol. The size and cross-linking of sol particles are determined by the pH and R ratio ($R=[H_2O]/[Si(OR)_4]$). Schematic of chemical reaction is shown in Figure 2.22.
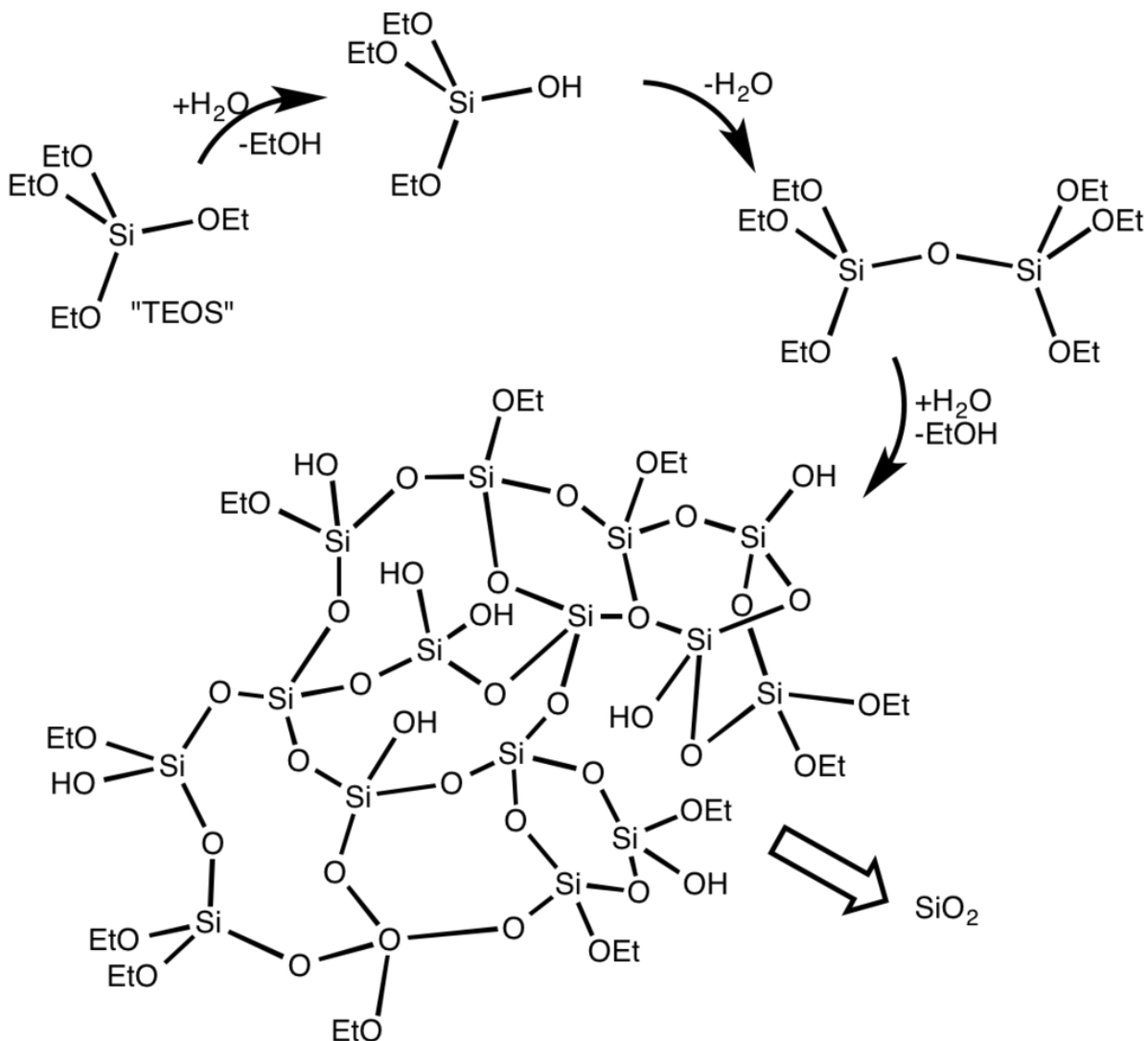
Figure 2.22. Schematic of hydrolysis and condensation polymerization of TEOS in sol-gel process

Step 2 : Casting

Since the sol solution is a liquid with a low viscosity, it is possible to cast the mold.

Step 3 : Gelation.

Depending on the time, the colloidal particles and the condensed silica are connected to form a three-dimensional network. The physical properties of the gel network depend on extent of cross-linking and particle size prior to gelation. Since the viscosity of the sol rapidly increases during the gelation, the viscosity can be adjusted using time.

Step 4 : Aging

Aging involves maintaining the state of gel solution for period time as a hour to days. Condensation polymerization continues during aging to increase thickness of interparticle necks and reduce porosity of gel network.

Step 5 : Drying

The liquid is vaporized from interconnected pore network by drying. If the pore is small, a large capillary stress is generated during drying. These stresses will cause defects in the gel unless drying process is managed by reducing surface energy of liquid by obtaining size of pore by controlling rate of condensation polymerization and hydrolysis.

Step 6 : Dehydration

Surface silanol (Si-OH) is removed from pore network by chemically stable porous solid. Gel with interconnected porosity is optically transparent and have enough strength to be used for optical components.

Step 7 : Densification

When the porous gel is heat-treated at a high temperature, the pores disappeared, and the density becomes equal to that of fused silica. Alkoxide gels were densified at 1000 degree. Purity and uniformity of silica fabricated by method 3 is superior to other methods.

2.9 Measurement method of mechanical properties for nanoscale thickness thin films

2.9.1 Hole-nanoindentation

Nanoindentation is a useful way of measuring the mechanical properties of thin films and two-dimensional materials. Sample fabrication process for hole-nanoindentation is simpler than sample fabrication process for other mechanical properties measurement method. Testing material was deposited on sacrificial layer and transferred to hole substrate by removing sacrificial layer. In case of two-dimension and thin film materials, it is important that sample were fabricated by same fabrication process because the mechanical properties are easily changed according to the microstructure.

The ratio between the diameter of the hole and the tip is important to measure mechanical properties[77]. When the ratio is less than 0.03, the hole indentation proceeds to point loading. However, if ratio exceeds 0.14, the loading mechanism changes from point loading to sphere loading due to increasing contact area during the experiment. Therefore, the ratio should be kept below 0.03 The associated graph is shown in Figure 2.23.

Deformation mechanism during hole-nanoindentation process is represented by linear (plate) solution or nonlinear (membrane) solution under influence of pre-strain, Poisson ratio, diameter of hole, and sample thickness[78]. If the ratio of sample thickness and diameter of hole exceeds 0.075, the nonlinear deformation behavior disappears regardless of other variables. For this reason, it is important to keep the ratio of sample thickness and diameter of hole below 0.075.

Mechanical properties of two-dimensional materials and thin films suspended on circular hole were evaluated by force-displacement curve measured by indenting using spherical indenter at center of hole[79]. The relationship between the force-depth curves and the properties of the suspended film being tested by hole-nanoindentation measurements can be described by the following equations:

$$F = \sigma_0(\pi a)\left(\frac{\delta}{a}\right) + E(q^3 a)(\frac{\delta}{a})^3, \tag{2.5}$$

$$\sigma_m = (\frac{FE}{4\pi R})^{1/2}, \tag{2.6}$$

where F is the applied force, δ is the deflection at center position, σ_0 is the pretension, E is the elastic modulus; $q=1/(1.05-0.15\upsilon-0.16\upsilon^2)$ is the dimensionless constant where υ is the Poisson's ratio, a is the radius of hole, σ_m is the maximum stress at center position, and R is the radius of tip. If the material undergoes a linear elastic deformation until fracture, it is fitted with the preceding formula. However, if the material contains plastic deformation, it will leave the fitting. Using the above phenomenon, the maximum stress at the point where the force-displacement curve exits the fitting is designated as the yield strength.
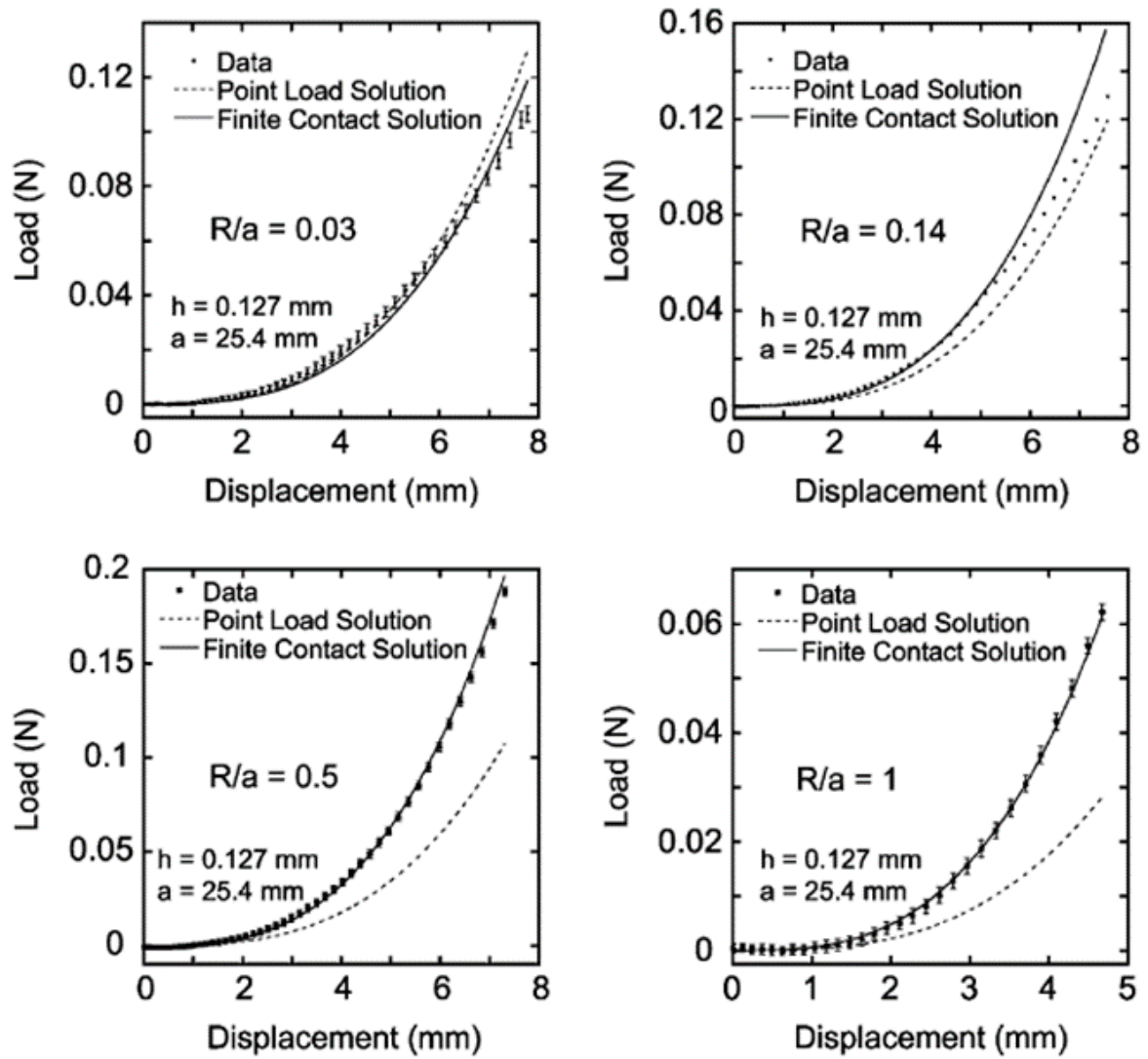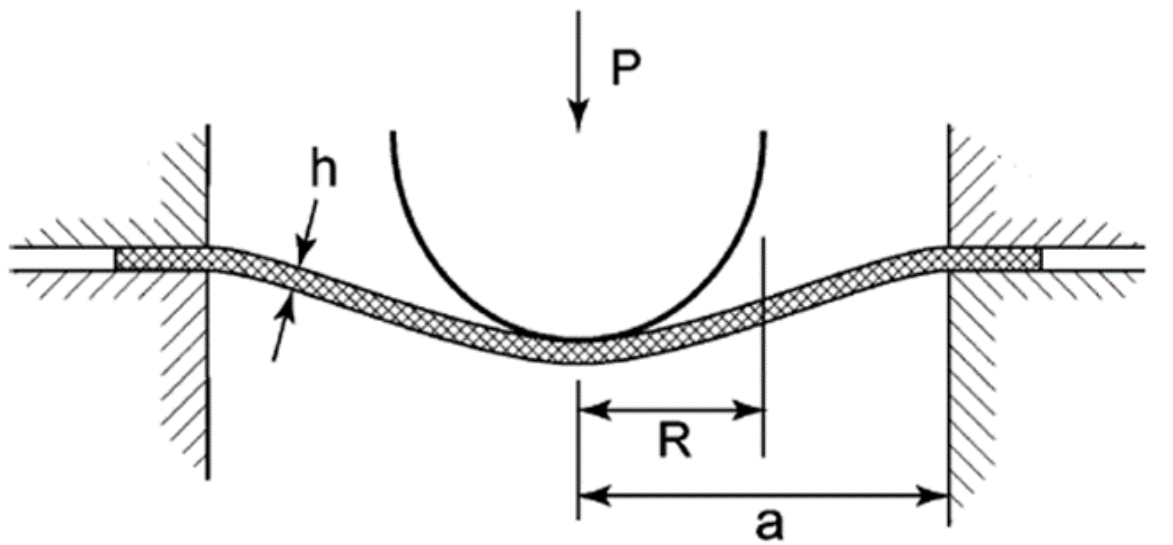
Figure 2.23. Change of load displacement curve according to ratio of tip and hole curvature[77].

2.9.2 Fabrication process of hole substrate

As mentioned above, since the deformation mechanism varies depending on the ratio of the thickness of the thin film and the diameter of the hole, it is important to select the diameter of the hole according to the thickness of the sample. As show in Figure 2.24, the hole substrate is set to four kinds according to the diameter of the hole, and the interval between the holes is set to 10 times the hole diameter. Design of hole substrate was patterned on silicon substrate using photo-resist AZ5214E (MicroChemicals GmbH, Ulm, Germany) with mask aligner MA/BA6 (SUSS MicroTech, Garching, Germany). Silicon substrate was etched up to 20 μm and photo resist was used to soft-mask during deep reactive-ion etching process using deep Si etcher Tegal 200 (Tegal, Petaluma, CA, USA) Finally, photo resist was removed with acetone. Cross-sectional image measured by scanning electron microscopy (SEM) are shown in Figure 2.24.
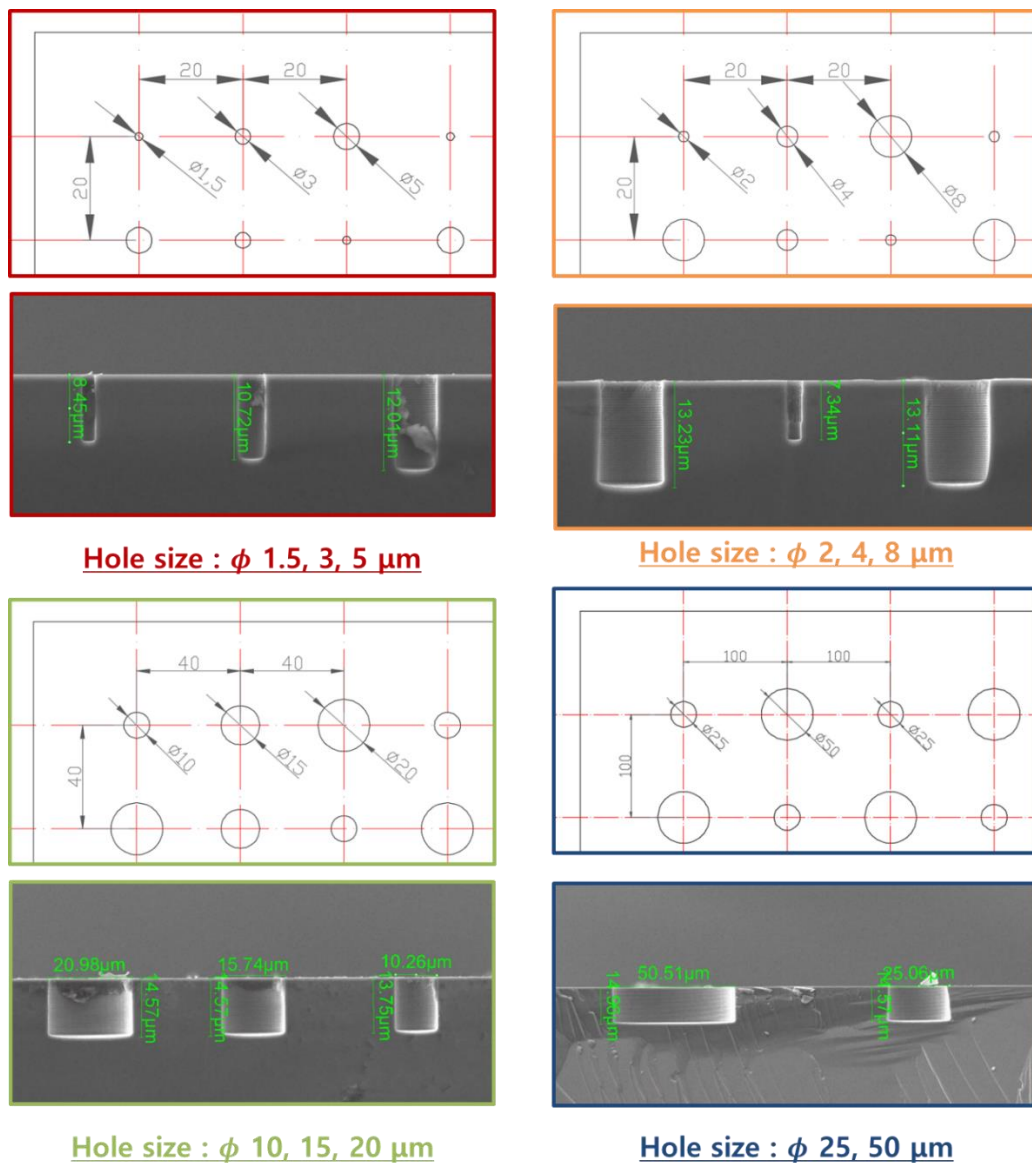
Figure 2.24. Design and cross-sectional image of hole substrates

2.9.3 In-situ tensile test in micro- and nano-scale

Mechanical properties such as elastic modulus, yield strength, yield strain, and fracture strain are required for life prediction and quality control. The tensile test has the advantage that it can apply uniform load and deformation to the sample and can measure the accurate mechanical properties. Tensile test was widely used to measure mechanical properties in bulk-scale. Standard for tensile test method were established early, and a lot of equipment for the experiment was developed in bulk-scale.

However, Tensile test is challenging at micro- and nano-scale due to difficulties in preparation of free-standing and stress-free state samples. In addition, there is a difficulty of experimental preparation such as sample alignment, gripping, deflection and load and strain measurement. Due to these disadvantages, mechanical properties of micro- and nano-scale materials have been measured by various other methods such as nanoindentation, bulge test, bending test, and torsion test.

Recent developments in technology have led to much research into the analysis of mechanical properties by tensile test. Actuators with micro-newton scale resolution have been developed and various strain analysis methods such as digital image correlation and optical encoders[80-82]. On-chip test devices based on MEMS device system was developed and has been extensively studied to supplement the experimental difficult[83, 84]. However, on-chip test devices cannot be used more than once. Also, it is difficult to apply it to various materials because it is limited in device manufacturing process. For this reason, the most recent on-chip test method is being studied in such a way that a sample is prepared separately and transferred to the device. However, this approach also creates alignment issues.

In this study, pico-indenter and Push-to-Pull device developed by Hysitron was used to perform tensile test. Push-to-Pull device was developed for MEMS device to measure mechanical properties by tensile test in scanning electron microscopy and transmission electron microscopy with pico-indenter. The Push-to-Pull device has been able to obtain the force-displacement behavior and real-time deformation image of tensile samples can be obtained with an SEM and TEM. It is also possible to perform tensile tests on organic materials which degrade easily by moisture in the air. Since nanoscale samples are very small, tensile test specimens must be fabricated using focused ion beam and transferred to Push-to-Pull device by Omni-probe system. Alignment issues were solved by aligning the sample and the device using the rotation function of the FIB equipment.

2.9.4 MEMs device fabrication process for in-situ mechanical test

Microelectromechanical systems (MEMS) device for in-situ tensile test was designed based on Push-to-Pull device (Hysitron, Minneapolis, MN, USA). Hysitron Push-to-Pull device is mainly used to tensile nanowires and has a very narrow gap between the mobile part and the fixed part of 2 μm. Since the sample size varies depending on the material, the gap is varied from 6 μm to 30 μm. Push-to-Pull device was fabricated using Silicon on insulator (SOI) wafer composed 10 μm-thick device layer, 1 μm-thick SiO_2 box layer, and 300 μm-thick Si handle layer. Device designs were patterned with photo resist by mask aligner MA/BA6 (SUSS MicroTech, Garching, Germany), Chromium layer was deposited by DC sputter SRN-120 (Sorona, Korea) on patterned photo resist, and lift-off process was performed on both sides of the SOI wafer. Deep reactive-ion etching process was performed on both side of SOI wafer using deep Si etcher Tegal 200 (Tegal, Petaluma, CA, USA) to stop at box layer. Finally, Silicon dioxide box layer was etched by Hydrogen fluoride (HF, J.T.Baker). Schematic of fabrication process and image of Push-to-Pull device was shown in Figure 2.25. The manufactured push-to-pull device was pressed with a sharp tip to confirm that the stiffness was linear and overlapped during loading and unloading. Figure 2.26 shows how to check the stiffness using UTM after device creation, and the device's stiffness when pressed up to 4 μm.

(a)

(b)
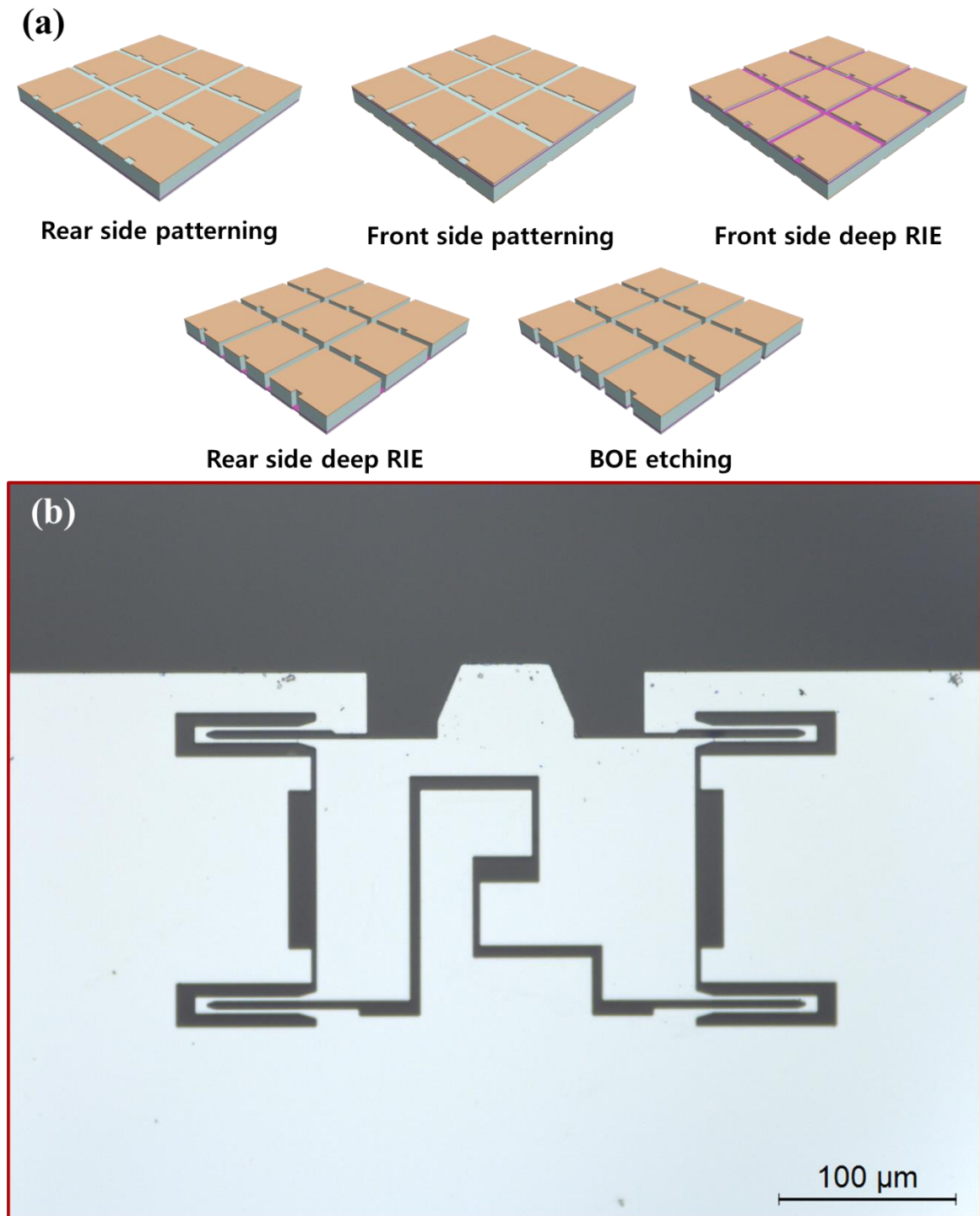
Figure 2.25. (a) Schematics of fabrication process of device and (b) image of Push-to-Pull device.
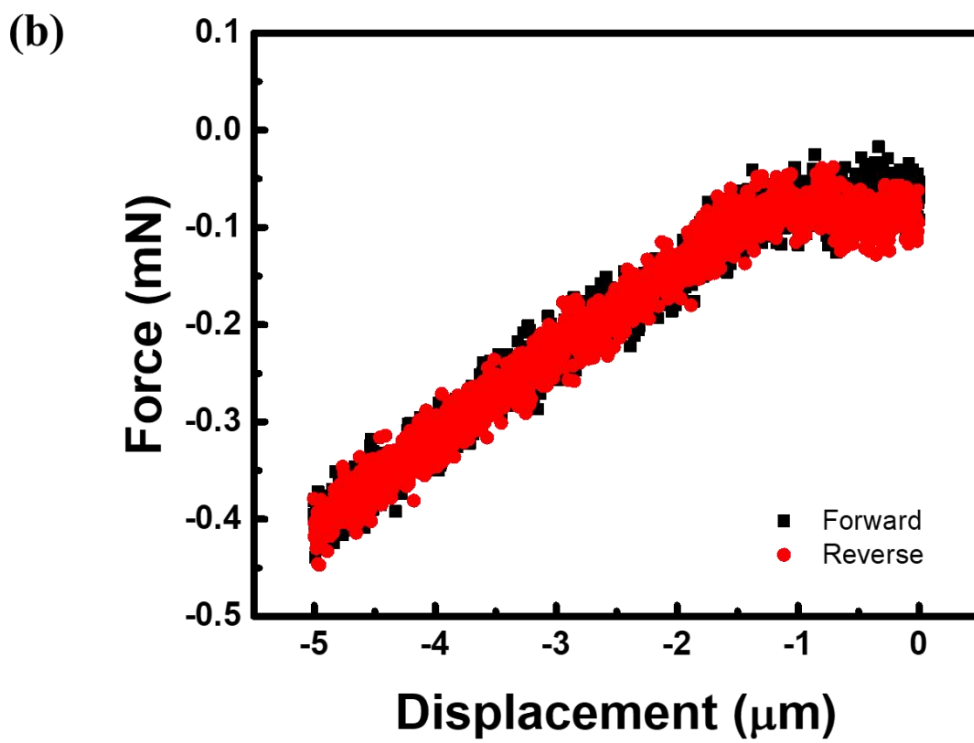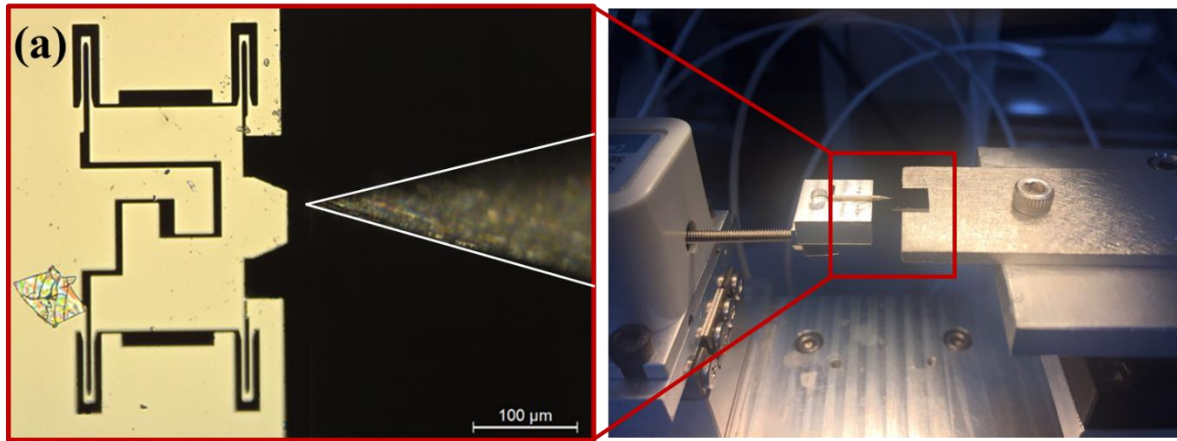
Figure 2.26. (a) Image of nano-UTM equipment set-up for stiffness measurement test and (b) graph of stiffness of Push-to-Pull device.

3. Flexibility of perovskite LEDs

3.1 Fabrication of perovskite LEDs

3.1.1 Materials

The synthesis of MABr and the preparation of the $MAPbBr_3$ solution have been described elsewhere[85]. The polymer SPW-111 (Merck Co.) and PFN (1-Materials) were obtained commercially and used without further purification. NOA63 (Norland Optics) was used for the encapsulation layer, and PET (PET 70 μm, AMG) was used as the substrate. All the reagents, namely, $PbBr_2$ (99%, Alfa Aesar), N,N-dimethylformamide (DMF, Aldrich), 2-propanol (IPA, Aldrich), acetic acid (Aldrich), chlorobenzene (Aldrich), 1,2 dichlorobenzene (Aldrich), PEDOT:PSS (PH1000, Clevios), Zonyl FS-300 (Aldrich), and AgNWs (1.0 wt% IPA suspension, Nanopyxis), were used as received without further purification.

3.1.2 Device fabrication

PEDOT: PSS was filtered with a 0.45 PVDF filter to make the PDZ. After the filtration process, PDZ was prepared by mixing 5 wt% DMSO and 0.5 wt% Zonyl in filtrated PEDOT:PSS. Next, PDZ layer was made by spin-coating on oxygen-plasma-treated PET substrates at 3000 rpm for 60 s. Coated PDZ layer annealed at 110°C for 10 min. The coating and annealing process was repeated to make three layers PDZ electrode. The precursor mixture was prepared by mixing MABr (Dyesol) and lead bromide ($PbBr_2$ Alfa Aesar) in a molar ration of 1:1. The resulting mixture was dissolved in a mixture of DMF and DMSO to form a precursor solution. Prepared precursor solution was spin-coated on PDZ layer. After 30 s of spinning, 50 μL of dichlorobenzene was dropped onto spinning sample to rinse DMSO off perovskite. SPW-111 dissolved in chlorobenzene was spin coated on perovskite layer. PFN dissolved in isopropyl alcohol and acetic acid by stirring at 75°C. Prepared PFN solution was spin-coated on SPW-111 layer. Finally, silver nanowires dissolved in isopropyl alcohol were coated on PFN layer by spaying process using air brush. The light emitting area of device was 13.5 mm^2. Encapsulation of devices were performed using NOA63 before testing. The whole production process is shown on Figure 3.1
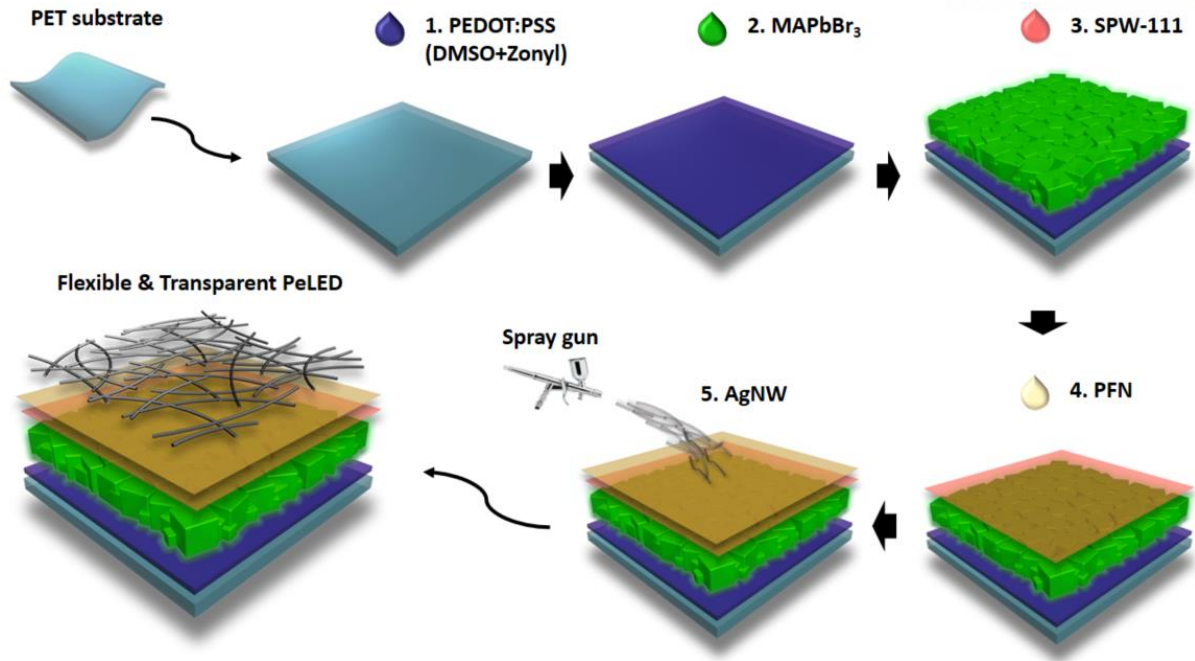
Figure 3.1. Schematic of process for fabrication FSPeLED[86].

3.2 Microstructure and optical properties of perovskite LEDs

3.2.1 Characterization of MAPbBr$_3$ films and FSPeLEDs.

Surface morphology of perovskite layer and multi-layer structure of FSPeLEDs are confirmed by scanning electron microscopy (Nanonova 230, FEI). The crystallinity of perovskite layer was analyzed using XRD measurement. A Cu-Kα radiation source installed in D8 Advanced diffractometer (Bruker) was used to record of XRD pattern as step size 0.01° and acquisition rate 5 min deg^{-1}. Source meter (Keithley 2400, Keithley) and a spectroradiometer (CS-2000, Konica Minolta Co.) were used to determine characteristic of FSPeLED device. Source meter (Keithley 2400, Keithley) was used to determine variation in luminance of FSPeLEDs under a constant applied current condition. Four-point probe (CMT-2000N, AIT) was used to determine sheet resistances of electrodes. Ultraviolet-visible-near infrared spectrometer (UV-1800, Shimadzu) was used to determine transmittances of device and electrodes. In this study, the transmittance at 550 nm, which is the wavelength of general green light, is represented as a representative value because the MAPbBr$_3$ used as the light emitting layer of the perovskite LEDs emitted green light.

Schematic of fabricated device and a cross-sectional image of an entire device measured by scanning electron microscopy are present in Figure 3.2. Flexible and semitransparent perovskite LEDs are realized using transparent and flexible constituent materials.

As shown in Figure 3.3, the uniformity and density of fabricated MAPbBr$_3$ layer on the PDZ anode was confirmed by X-ray diffraction and scanning electron microscopy imaging analyses. Diffraction peaks of MAPbBr$_3$ was represented by three individual diffraction peaks presented in Figure 3.3(a). Based on results of X-ray diffraction pattern and surface image of perovskite, it is confirmed that perovskite grew uniformly in cubic structure on PDZ layer
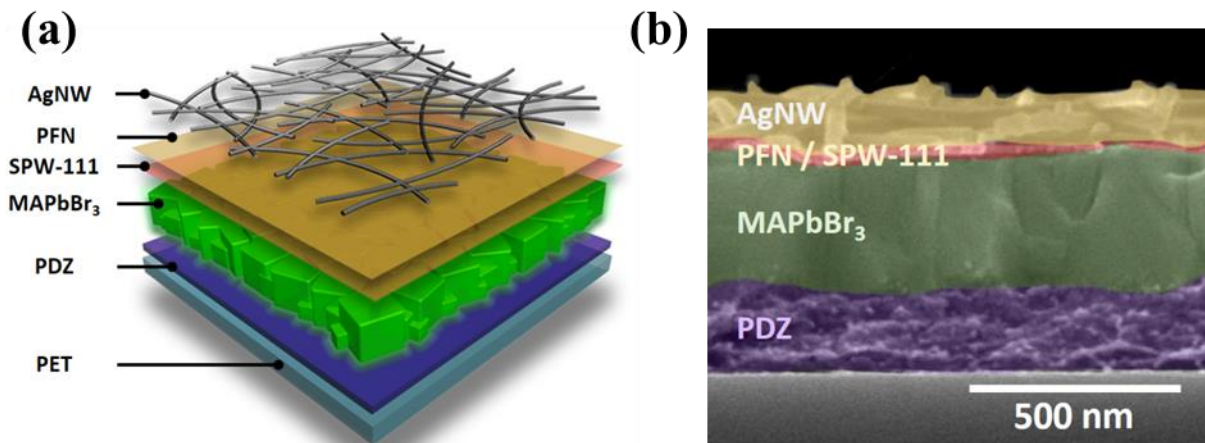
Figure 3.2. Schematic of flexible and semitransparent Perovskite LEDs (FSPeLEDs). (b) Cross-sectional SEM image of FSPeLEDs[86].
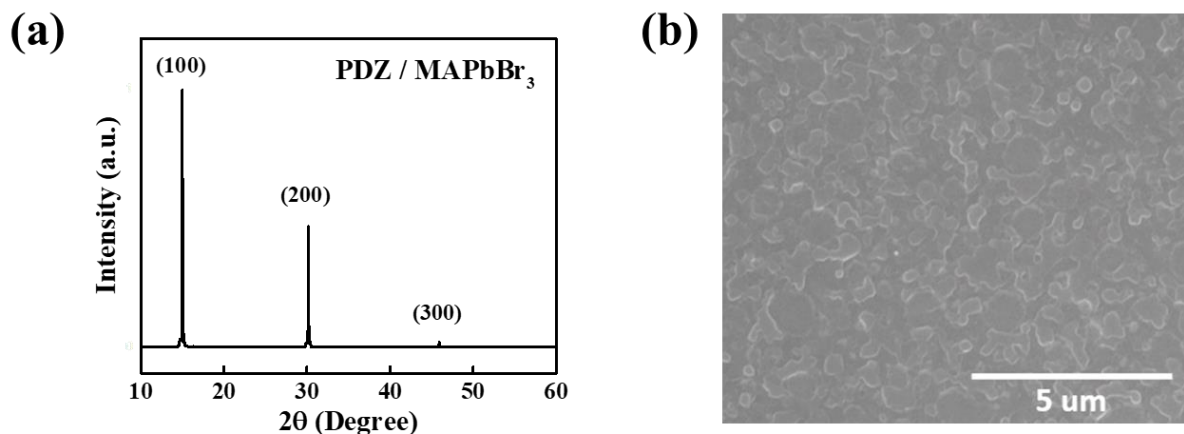
Figure 3.3. (a) X-ray diffraction (XRD) patterns and (b) SEM image of MAPbBr$_3$ on PDZ[86].

Anode of FSPeLEDs was fabricated using PEDOT:PSS doped by DMSO and zonyl instead of indium tin oxide (ITO). The PEDOT:PSS was doped with 5 wt.% DMSO and 0.5 wt.% Zonyl to increase conductivity of anode[87]. The fluorosurfactant Zonyl was specially doped in PEDOT:PSS so that PEDOT:PSS was well coated on hydrophobic poly(ethylene terephthalate) (PET) substrate[87]. The 200 nm thick PDZ layer as anode in fabricated device has high optical and electrical properties with low sheet resistance as 74 Ω sq^{-1} and transmittance as 85.7% as 550 nm shown in Figure 3.4 and Table 3.1. PFN and silver nanowire used as cathode in fabricated device has low sheet resistance as 20.5 Ω sq^{-1} and high transmittance as 81.3% at 550 nm shown in Figure 3.5 and Table 3.2. Both cathode and anode are transparent and very flexible. As shown in Figure 3.6, transparency of FSPeLEDs was confirmed by photograph and transmittance spectrum was determined. Transmittance of fabricated device was determined to be 48% at 550 nm.
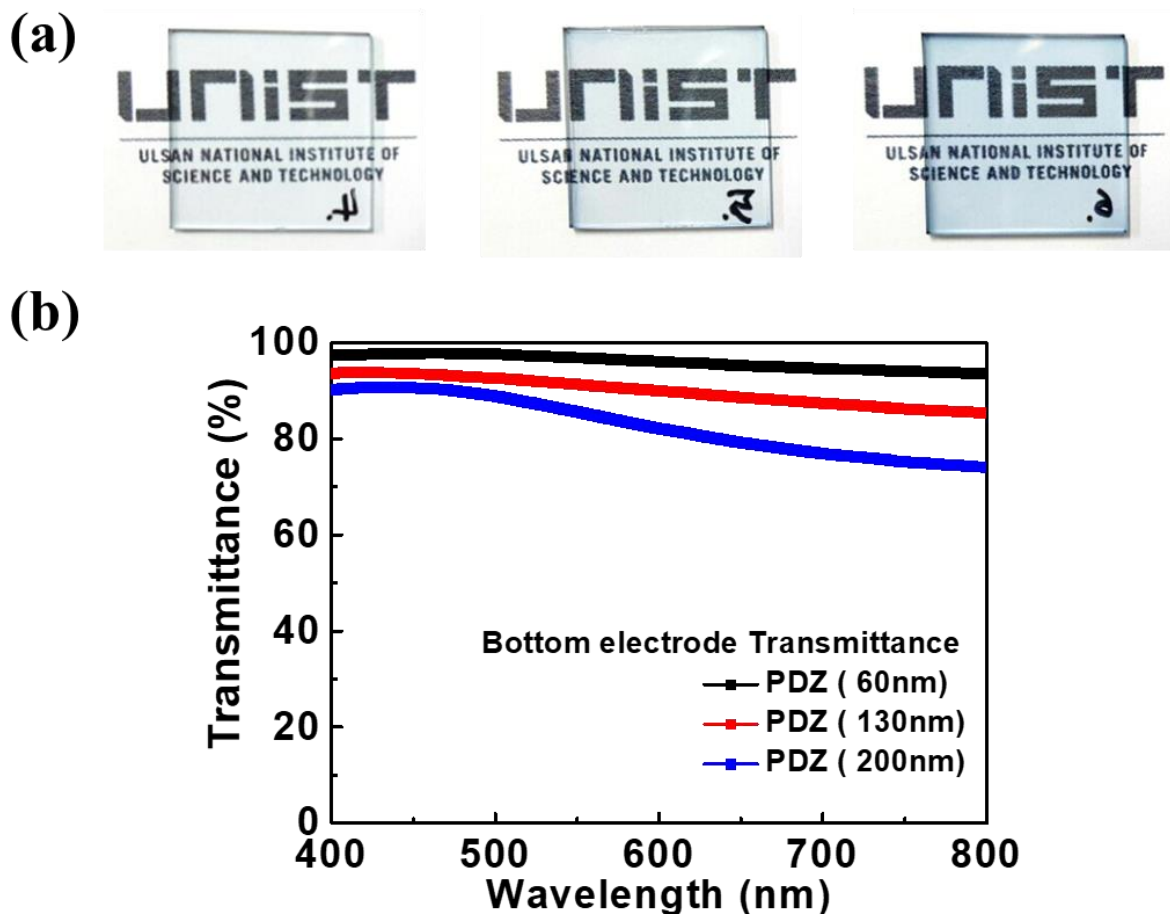
Figure 3.4. (a) Optical images and (b) transmittance spectrum of various thickness of PDZ electrode[86].

Table 3.1. Summarized electrode performance of various thickness of PDZ[86].

Thickness of PDZ layer	R_{sheet} ($\Omega/\square$)	Transmittance (%) @550nm
60 nm	240	96.8%
130 nm	110	91.3%
200 nm	74	85.7%
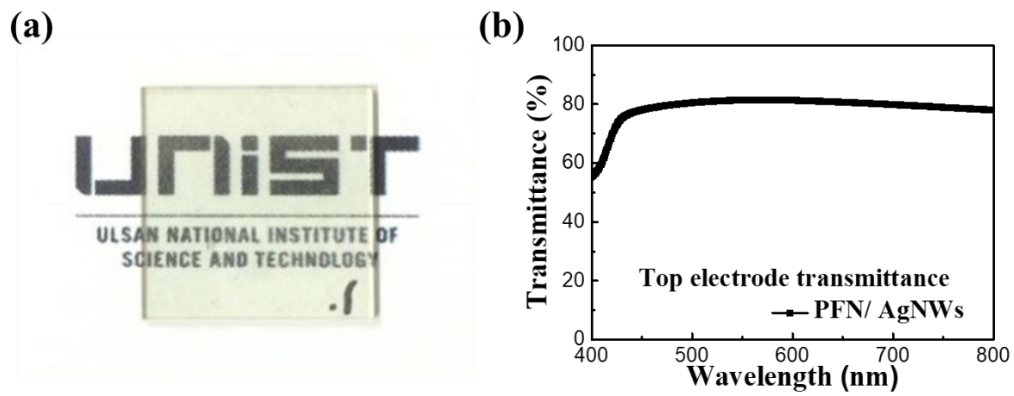
Figure 3.5. (a) Optical images and (b) Transmittance spectrum of AgNW electrode[86].

Table 3.2. Summarized electrode performance of AgNW[86].

Thickness of PDZ layer	R_{sheet} ($\Omega/\square$)	Transmittance (%) @550nm
130 nm	20.5	81.3%
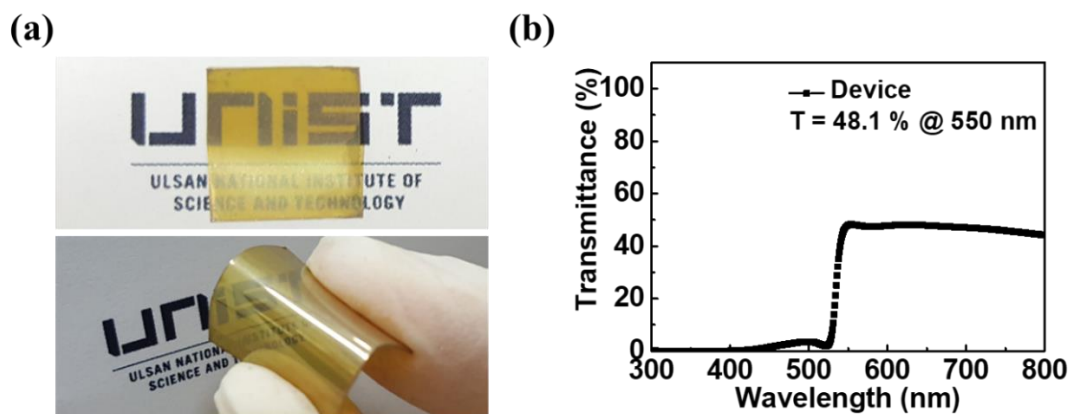
Figure 3.6. (a) Photographs and (b) transmittance spectrum of FSPeLEDs[86].

3.2.2 Device performance of FSPeLEDs

Device performance curves of FSPeLEDs are presented in Figure 3.7. Graphs denoted the current density versus voltage curve (Figure 3.7 (a)), the luminance versus voltage curve (Figure 3.7 (b)), and the luminous efficiency versus voltage curve (Figure 3.7 (c)), respectively. The fabricated perovskite element emits green light with a maximum peak at 537 nm. The narrowness of the peaks (FWHM = 20 nm) confirmed to high color purity of FSPeLEDs shown in Figure 3.7 (d). Maximum luminance, luminous efficiency, and maximum external quantum efficiency of FSPeLEDs was measured to be 1,260 cd m^{-2} (at 5.5 V), 0.79 cd A^{-1} (at 5.0 V), and 0.17% (at 3.0 V), respectively. Table 3.3 summarize the device performance parameters of the FSPeLEDs.
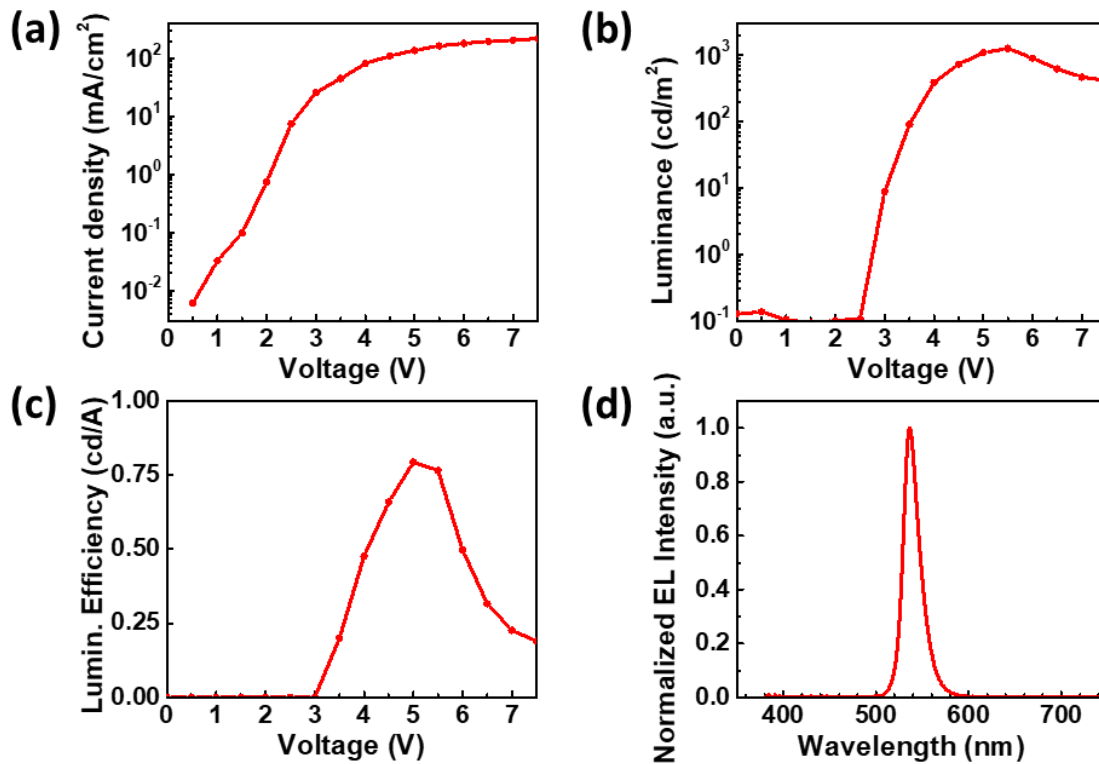
Figure 3.7. Device performance of FSPeLEDs with and without PFN. a) J-V, b) L-V, and c) LE-V characteristics of FSPeLEDs. d) EL spectrum of FSPeLEDs[86].

Table 3.3. Summarized device performance of FSPeLEDs[86].

Device configuration	L_{max} (cd/m^2)	LE_{max} (cd/A)	PE_{max} (lm/W)	EQE_{max} (%)
PET/PDZ/MAPbBr$_3$/PFN/AgNW	1,260 (5.5 V)	0.79 (5.0 V)	0.50 (5.0 V)	0.17 (5.0 V)

3.3 Flexibility of perovskite LEDs and top & bottom electrodes

3.3.1 Characterization of bendability of FSPeLEDs

Image of fabricated perovskite LEDs under a bending and twisting stress state are presented in Figure 3.8. These images showed that fabricated devices are semitransparent and very flexible. Photographs of FSPeLEDs under various bending radius of 10, 5, 2.5, and 1mm to confirm experimental condition of cyclic bending test are present in Figure 3.9 (a)

As shown in Figure 3.9 (b), the luminance changes of fabricated perovskite LEDs with different bending radius were determined during repeated bending in ambient conditions to confirm the mechanical bendability of FSPeLEDs. Since there is no difference in the results for samples with bending curvature of 2.5 mm or more in preliminary test, bending radius for the cyclic bending tests were set to 2.5 mm, and 1 mm. Cyclic bending test of FPSeLEDs were performed using a linear actuator (PI, Karlsruhe, Germany). Change of luminance was measured every 20 cycles and measured up to 400 cycles.

The luminance of FSPeLED became zero after 320 bending cycles at bending radius of 1 mm. On the other hands, the luminance of FSPeLEDs maintained 80% of initial luminance of FSPeLEDs after 400 bending cycles at bending radius of flat and 2.5 mm. Reason of these results are mechanical failure in component materials and interfacial separate phenomena during repeated bending at bending radius of 1 mm. The measurement interval of luminance at bending radius of flat was set equal to bending radius of 2.5 mm and 1 mm. Based on result of change in luminance at bending radius, encapsulation was not perfectly good by 50 μm-thick Norland optical adhesive 63 (NOA63). Therefore, I thought that decrease in luminance of FSPeLEDs with bending radius of flat and 2.5 mm occurred by reaction with moisture and oxygen due to incomplete encapsulation.
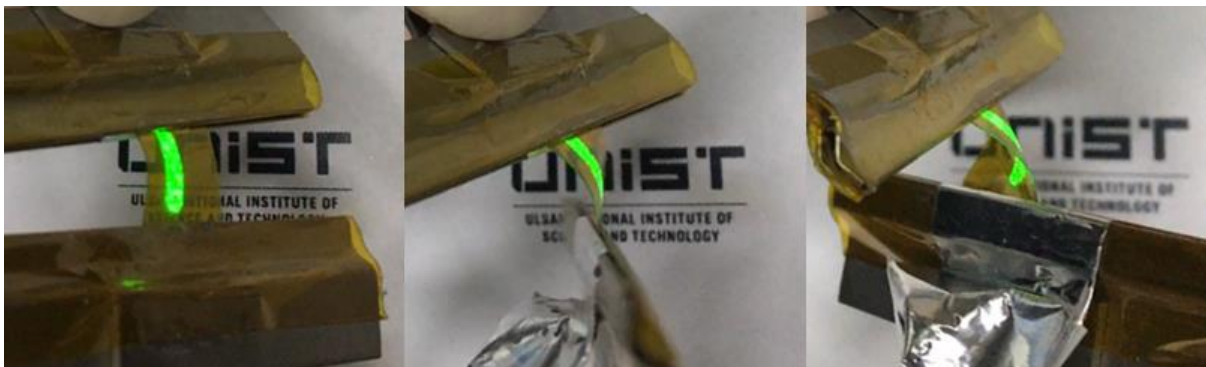
Figure 3.8. Photographs of FSPeLEDs under twisted bending stress that shows luminescence in both side direction[86].
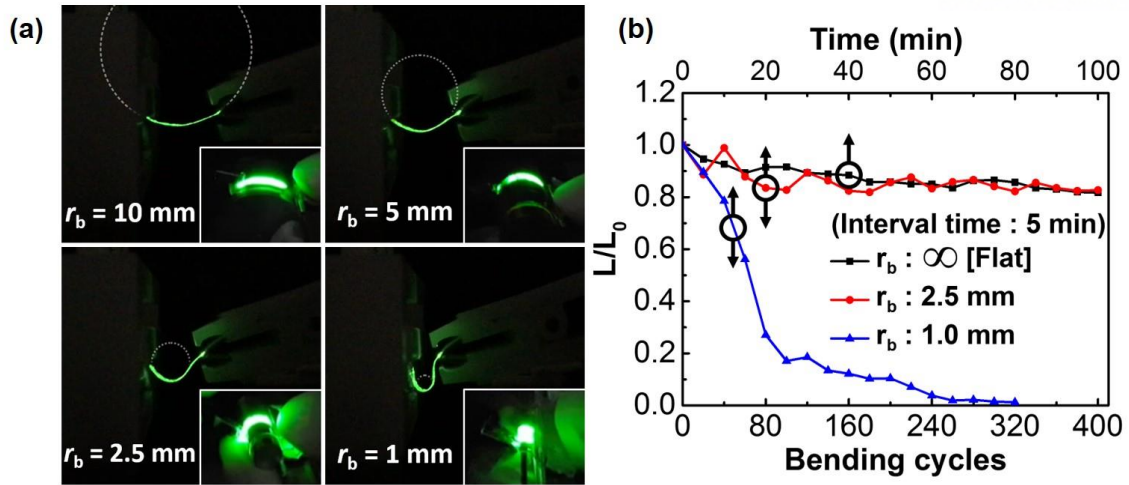
Figure 3.9. Cyclic bending test of FSPeLEDs. (a) Side-view images of emissive FSPeLEDs with different r_b. (white dashed circles are visual aids. inset: diagonal views of emissive FSPeLEDs wrapped around cylindrical objects of described r_b). (b) Change in luminance under cyclic bending of FSPeLEDs[86].

3.3.2 Characterization of bendability of electrodes

Repeated bending tests were performed for PDZ and PFN/AgNW used as flexible electrodes in FSPeLED. Changes in sheet resistances are presented in Figure 3.10. The flexible electrodes are positioned between PET used as substrate and NOA63 used as encapsulation material used in repeated bending tests for FSPeLEDs. Stress applied in flexible electrodes during cyclic bending test is similar to that stress applied in repeated bending test for FSPeLEDs. Repeated bending tests of top and bottom electrodes were also performed using a linear actuator (PI, Karlsruhe, Germany) under ambient conditions. Bending radius of 1.0 mm was used. Resistance measurement of electrode was carried out up to 1,000 times every 100 times of repeated bending. Change of sheet resistance of electrode were measured by four-point probe.

The flexibility of the PDZ anode and the PFN/AgNW cathode were determined by measuring the changes in the sheet resistances of PDZ (see Figure 3.10 (a)) and the PFN/AgNW (see Figure 3.10(b)) up to 1,000 bending cycles. The maximum change in the sheet resistance per unit initial sheet resistance was measured to be 0.127 for the cathode and 0.135 for the anode. This result proves that the PDZ and PFN/AgNW electrodes are highly flexible, as shown in Figure 3.10. This means that one or more of the other components of the perovskite LEDs such as SPW-111 and $MAPbBr_3$, does not sustained applied stress during repetitive bending at a bending radius of 1 mm, thereby reducing the luminance of FSPeLEDs..
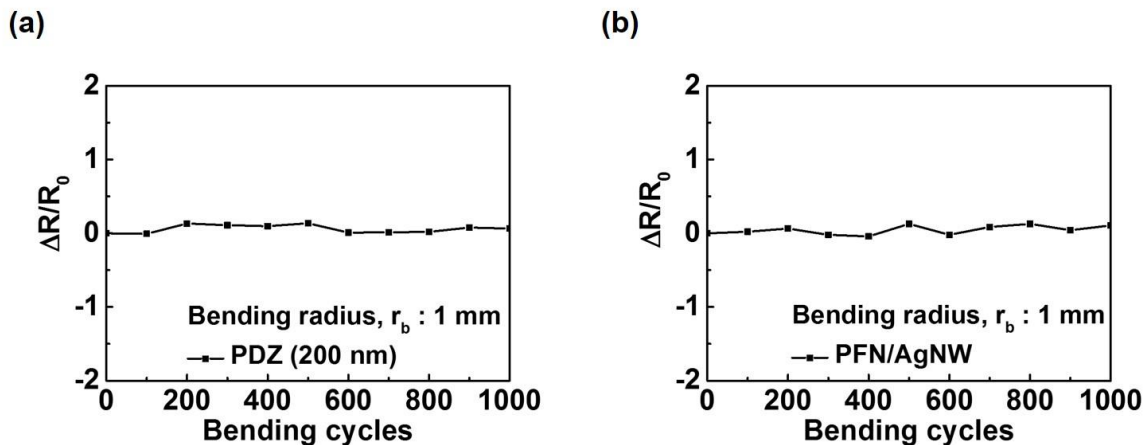
Figure 3.10. Cyclic bending test. Changes in sheet resistances of (a) PDZ and (b) PFN/AgNW layers with r_b of 1.0 mm because of cyclic bending under ambient conditions[86].

3.4 Mechanical properties of constituent materials by hole-nanoindentation test

3.4.1 Sample fabrication process for hole-nanoindentation

   As shown in Figure 3.11, the SPW-111, PDZ, and MAPbBr$_3$ samples for the hole-nanoindentation measurements were prepared by the transfer method. The materials were coated on sacrificial layers - PEDOT:PSS for SPW-111 and PMMA for PDZ and MAPbBr$_3$ - using the same procedures as those used for fabricating the FSPeLEDs, in order to ensure that the test samples had similar microstructures and thicknesses as in the devices. It is important to note that these materials were prepared by same procedures as those employed for fabricating the FSPeLEDs that they, PDZ, MAPbBr$_3$, and SPW-111 suspended on the holes, are expected to have identical microstructure and thickness in the device. The material layers were separated from the substrates by removing the sacrificial layers and were transferred onto hole-patterned silicon substrates. The diameters of the holes were 4 micrometer for SPW-111, 5 micrometer for PDZ, and 50 micrometer for MAPbBr$_3$, respectively. The ratio of the hole radius and the sample thickness was kept at less than 0.01. The nanoindentations measurements were carried out using a PI-87 SEM picoindenter (Hysitron, Minneapolis, MN, USA) with a load capacity of 10 mN. A cube corner type tip with a tip curvature of 90 nm was used. The displacement rate was controlled based on the thickness of the material being tested.

Spin coating   **Removal of sacrificial layer**   **Transfer (on hole-patterned wafer)**   **Hole-nanoindentation**
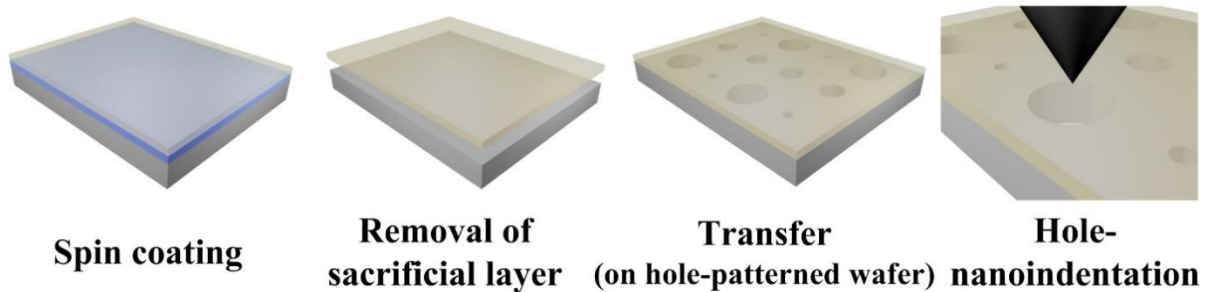
Figure 3.11. Schematic of process for fabricating samples for hole-nanoindentation measurements[86].

3.4.2 Confirm method of elastic deformation range of hole-nanoindentation

Hole-nanoindentation was performed by point loading deformation until fracture. During the hole nanoindentation, machine compliance occurs in which the load is reduced due to thermal drift phenomenon in the chamber. Correction is required because the measured load is less than the load on the actual sample. The indentation section can be divided into four regions approach, loading, unloading with contact and unloading without contact. As shown in range from the approach to unloading with contact of Figure 3.12 (a) and (b), the load is constantly decreasing displacement rate. Unloading proceeds at a fast rate programmatically. The rate of load reduction caused by thermal drift be evaluated by the equation as

$$d_l = \frac{F_s - F_c}{t_s - t_c}, \tag{3.1}$$

where d_l is rate of load drop during indentation, F is force, t is time, and subscripts s and c mean contact and separation, respectively. As shown in Figure 3.12 (c), the load acting on the actual sample was obtained through load reduction correction.
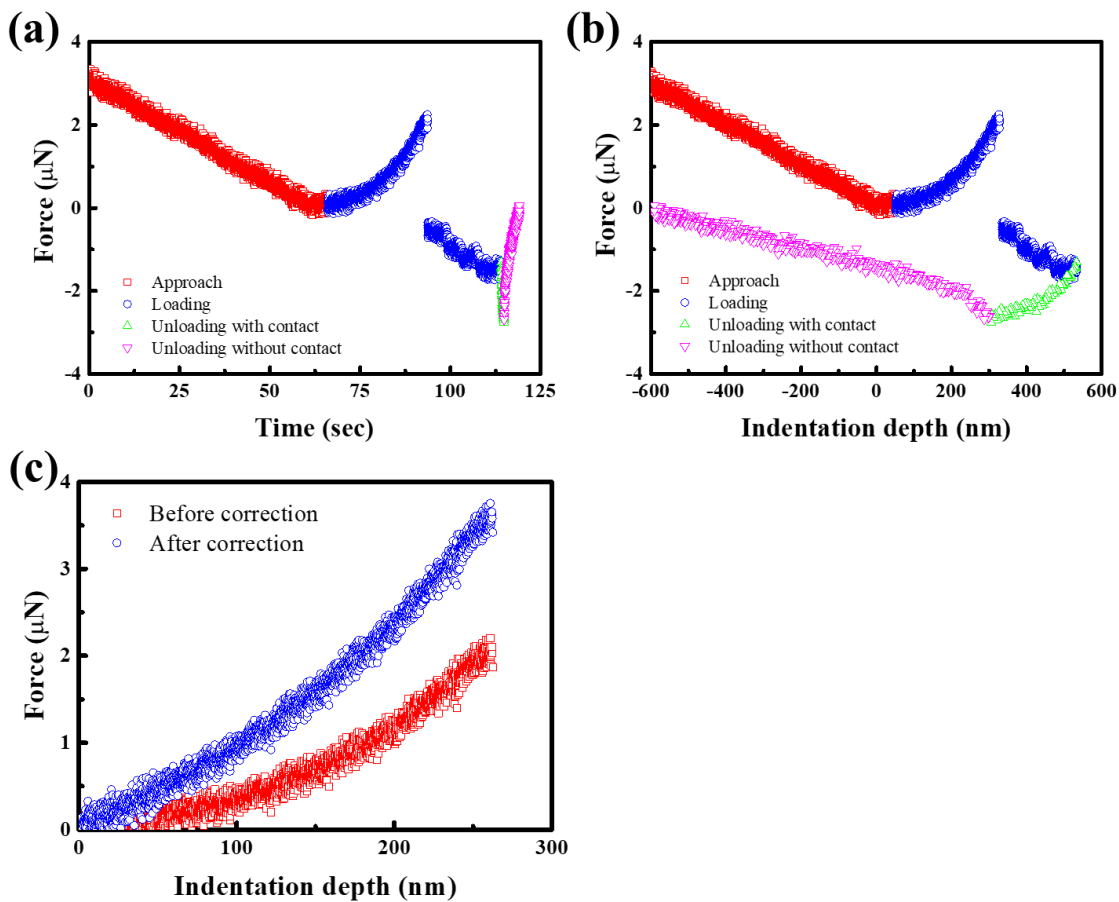
Figure 3.12. (a) Force-time and (b) Force-indentation depth curves of SPW-111 during hole-nanoindentation. (c) Force-indentation depth curves of SPW-111 before and after load correction.

Materials such as graphene, which mainly generate brittle fracture, undergo elastic deformation until fracture, but in the case of polymer materials, elasticity and plastic deformation occur together during hole-nanoindentation test. In order to accurately analyze the elastic limit of the material, it is important to find the point where the plastic deformation occurs. Elastic modulus was evaluated by equation as

$$F = \sigma_0(\pi a)\left(\frac{\delta}{a}\right) + E(q^3 a)\left(\frac{\delta}{a}\right)^3, \tag{3.2}$$

where F is the applied force, δ is the deflection at center position, σ_0 is the pretension, E is the elastic modulus; $q = 1/(1.05 - 0.15\upsilon - 0.16\upsilon^2)$ is the dimensionless constant where υ is the Poisson's ratio, a is the radius of hole to load-displacement curves[79]. As shown in Figure 3.13, if the sample undergoes plastic deformation above a certain indentation depth, the graph fitted by equation does not match the graph fitted by measured values. The elastic modulus differs from preceding range.
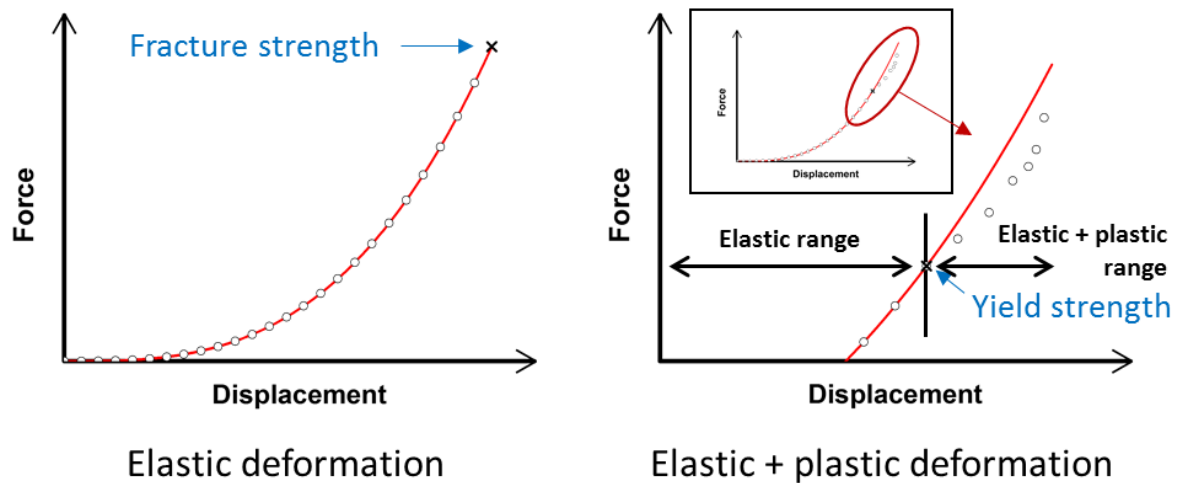
Figure 3.13. Correlation between hole-nanoindentation and fitting curves of (a) elastic deformation, (b) elastic and plastic deformation.

As shown in Figure 3.14, the elastic modulus and pre-strain of SPW-111 and PDZ were obtained by fitting with Equation (3.2) by increasing the range up to fracture. Elastic modulus and pre-strain of SPW-111 and PDZ according to indentation depth were presented in Figure 3.14 (b) and (d) and summarized in Table 3.4 and 3.5, respectively. At very low indentation depths, the fitting results are inaccurate due to the lack of data. As a result, the elastic modulus of the SPW-111 was also maintained until fracture. The elastic modulus of the PDZ was maintained until 700 nm and then decreased. SPW-111 does not undergo plastic deformation until fracture. The elastic limits of PDZ were analyzed at 700 nm.
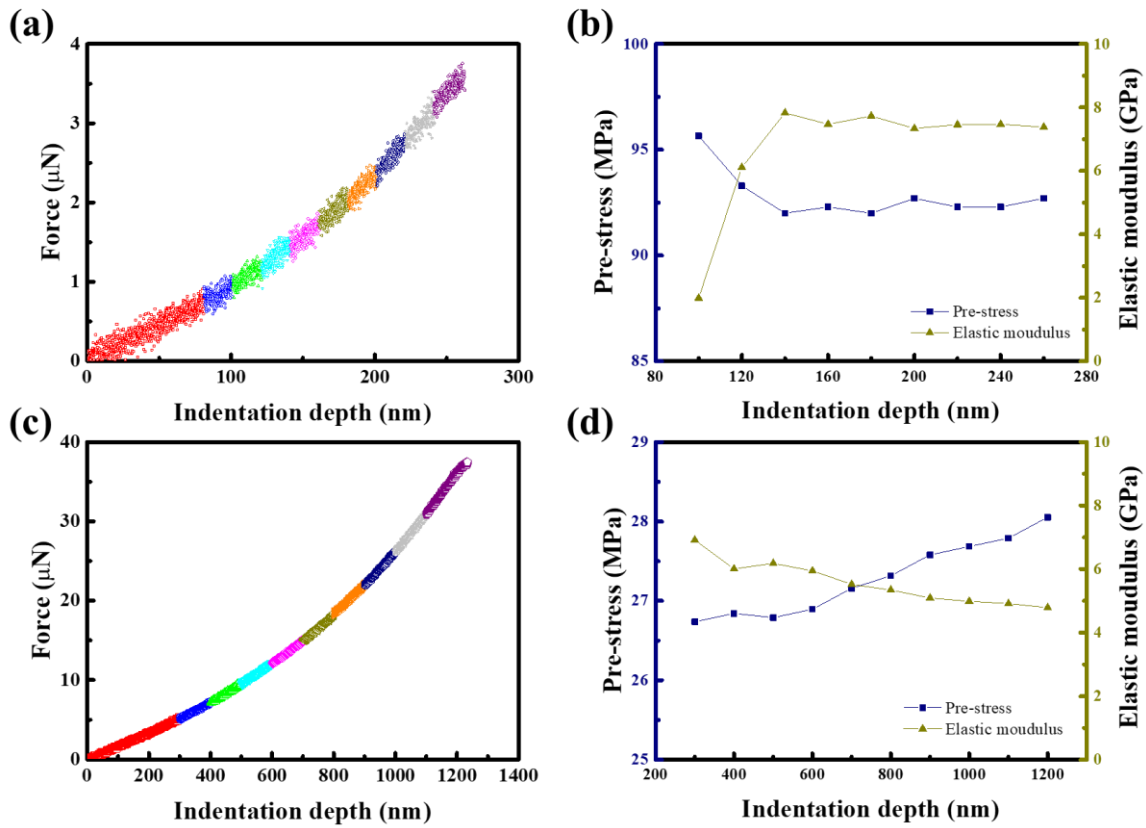
Figure 3.14. (a) and (c) Division of fitting ranges of force-indentation depth curves. (b) and (d) Pre-strain and elastic modulus of testing materials depending on fitting range. (a) and (b) are graph of SPW-111 and (c) and (d) are graph of PDZ, respectively.

Table 3.4. Pre-stress and elastic modulus according to fitting rang of SPW-111.

Fitting range	80	100	120	140	160	180	200	220	240	260
Normalize depth	31%	38%	46%	54%	62%	69%	77%	85%	82%	100%
Pre-stress (MPa)	73	95.7	93.3	92	92.3	92	92.7	92.3	92.3	92.7
Elastic modulus (GPa)	-4.1	1.99	6.11	7.83	7.47	7.73	7.34	7.46	7.47	7.38

Table 3.5. Pre-stress and elastic modulus according to fitting rang of PDZ.

Fitting range	300	400	500	600	700	800	900	1000	1100	Max
Normalize depth	25%	33%	42%	50%	58%	67%	75%	83%	92%	100%
Pre-stress (MPa)	23.68	24.42	24.84	24.95	25	25.21	25.42	25.79	26.16	26.79
Elastic modulus (GPa)	11.6	7.25	5.72	5.38	5.28	5.02	4.85	4.55	4.32	3.98

3.4.3 Characterization of mechanical properties by hole-nanoindentation

At least five reproducible force-indentation depth curves were obtained for each material. Figure 3.15 (a) shows a nanoindentation being made on a perovskite MAPbBr$_3$ layer suspended on circular hole. Figure 3.15 shows SEM images for hole-nanoindentation and typical force-depth curves for PDZ, MAPbBr$_3$, and SPW-111 in elastic deformation range. The elastic modulus and yield strength of the suspended films, which were indicative of the maximum strength in the elastic deformation range, were determined by fitting Equations (3.2) and

$$\sigma_m = (\frac{FE}{4\pi R})^{1/2}, \tag{3.3}$$

where F is the applied force, E is the elastic modulus, σ_m is the maximum stress at center position, and R is the radius of tip, to the nanoindentation force-depth curves, as shown in Figure 3.15 (b). SEM images of before and after hole-nanoindentation were shown in Figure 3.16. The elastic modulus and yield strength were 5.47 (±0.25) GPa and 606 (±23) MPa for PDZ, 28.15 (±2.94) GPa and 506 (±58) MPa for MAPbBr$_3$, and 7.53 (±0.25) GPa and 792 (±82) MPa for SPW-111, respectively. The values of the elastic modulus and yield strength are also listed in Table 3.6. If constituent material shows linear elastic deformation in uni-axial tensile loading, yield strain is calculated as 11.1 (±0.4)% for PDZ, 1.81 (±0.19)% for MAPbBr$_3$, and 10.5 (±0.8)% for SPW-111 with elastic modulus and yield strength measured by hole-nanoindentation. Based on the results of the cyclic bending tests for electrodes and hole-nanoindentations, it can be concluded that MAPbBr$_3$ is the weakest of all the constituent materials of FSPeLEDs.

The yield strain of a material, which is an elastic deformation limit, and a critical parameter affecting the mechanical robustness of the material under bending and stretching, cannot be measured directly by hole-nanoindentation measurements but is determined through uniaxial tensile tests. Nanoindentation is a useful way of measuring the mechanical properties of thin films and two-dimensional materials. However, the yield strain as determined by hole-nanoindentation could be inaccurate compared to that determined through uniaxial tensile testing, as several experimental issues have been reported with regards to hole-nanoindentation measurements, such as the concentration of stress around the contact region with the nanoindenter tip, determining the effective tip radius with accuracy, and friction between the suspended film and the tip/substrate hole edge[77, 78, 88, 89].
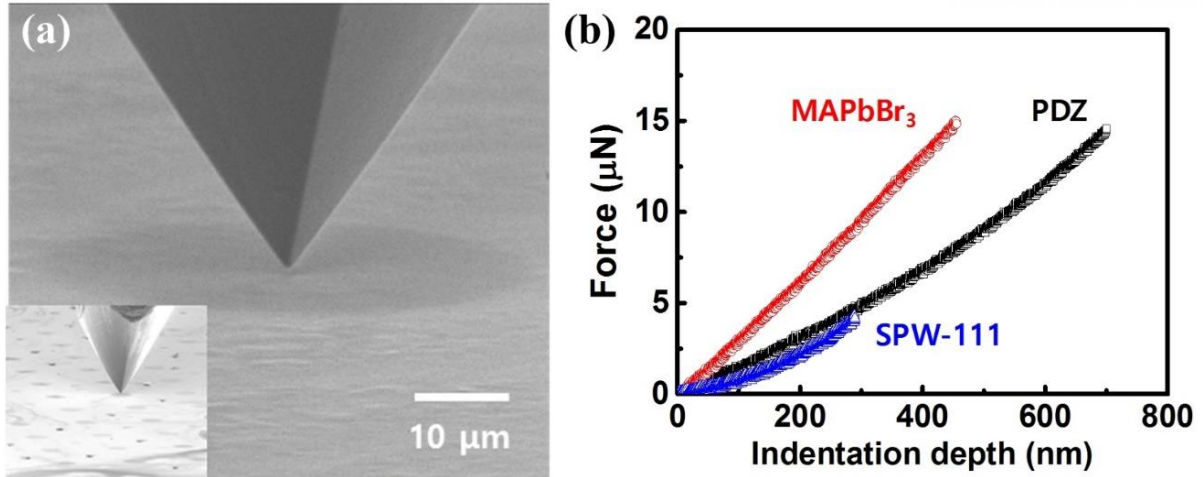
Figure 3.15. Hole-nanoindentation tests performed on PDZ, MAPbBr$_3$, and SPW-111 layers suspended on hole-patterned substrates. (a) SEM images of nanoindentation made on suspended perovskite MAPbBr$_3$ layer, and (b) typical indentation force-depth curves for PDZ, MAPbBr$_3$, and SPW-111 as measured by nanoindentation tests; the elastic modulus and yield strength values were determined based on these curves[86].
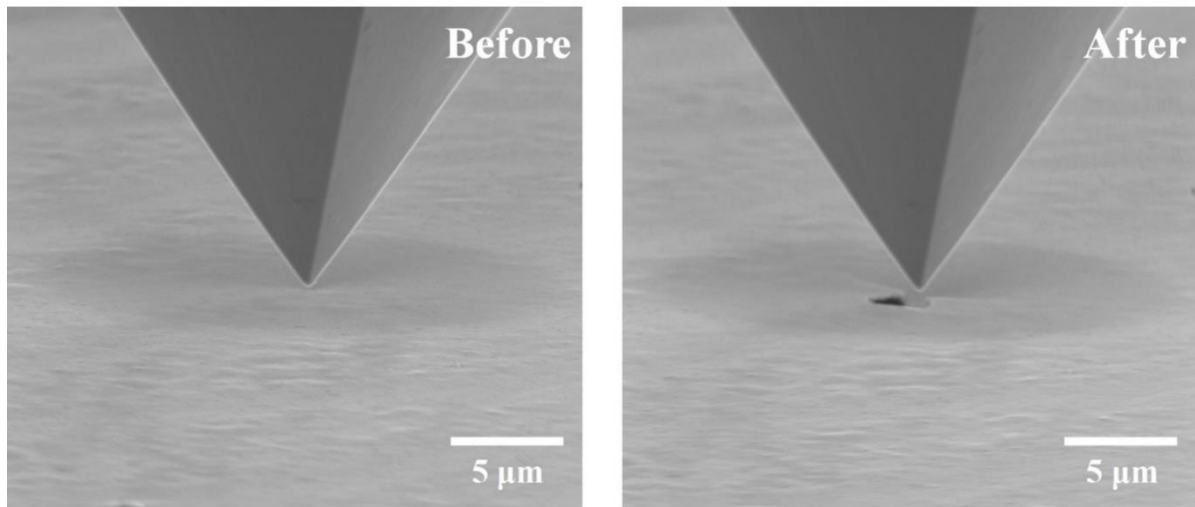
Figure 3.16. SEM image of hole-nanoindentation sample before and after testing[86].

Table 3.6. Mechanical properties of constituent materials of FSPeLEDs measured by hole-nanoindentation[86].

Materials	Elastic modulus (GPa)	Yield strength (MPa)	Yield strain (%)
PDZ	5.47±0.25	606±23	11.1±0.4
MAPbBr$_3$	28.15±2.94	506±28	1.81±0.19
SPW-111	7.53±0.25	792±82	10.5±0.08

3.5 Mechanical properties of perovskite layer by in-situ micro tensile test

3.5.1 Sample fabrication process for in-situ tensile test

The tensile test was carried out in order to measure the mechanical properties more accurately because of the disadvantage that the yield strength could not be obtained by using the hole indentation mentioned above. The tensile test was carried out only on the MAPbBr$_3$ with the lowest elastic limit as a result of the hole indentation.

As shown in Figure 3.17, dog-bone-like tensile samples with a gauge length of 12 μm were prepared by focused ion beam (FIB) milling and transferred and attached to the push-to-pull device using the micromanipulation system of the FIB. The MAPbBr$_3$ layer was prepared as described above and transferred onto a hole-patterned substrate. Since the perovskite is easily degraded by the ion-beam, sample was fabricated using a low current. In more detail about FIB milling process, shape of the gauge part was fabricated with 100 pA. When fabricated using high currents, the side of gauge section was not cleaned and was rough. The gauge section was fine milled using 50 pA. Next, the grip part which does not directly affect the experiment was formed using 300 pA. Finally, cutting area were formed using 300 pA. Tensile samples were cut off from hole-substrate. Tensile samples were transferred and attached to the push-to-pull device using the micromanipulation system of the FIB. Images of fabrication process were shown in Figure 3.18.

In-situ micro-tensile tests were performed using a PI-87 SEM picoindenter installed on a Quanta 200 FE-SEM system (FEI, Hillsboro, OR, USA) with a push-to-pull MEMS device. The in-situ micro-tensile tests were performed at a constant displacement rate of 6 nm s^{-1}.
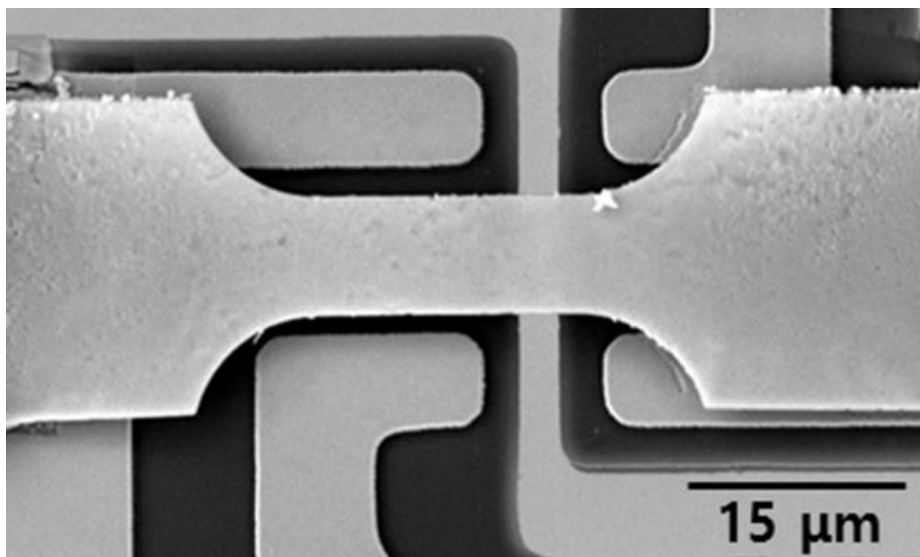
Figure 3.17. SEM image of tensile test sample of MAPbBr$_3$ attached on Push-to-Pull device[86].
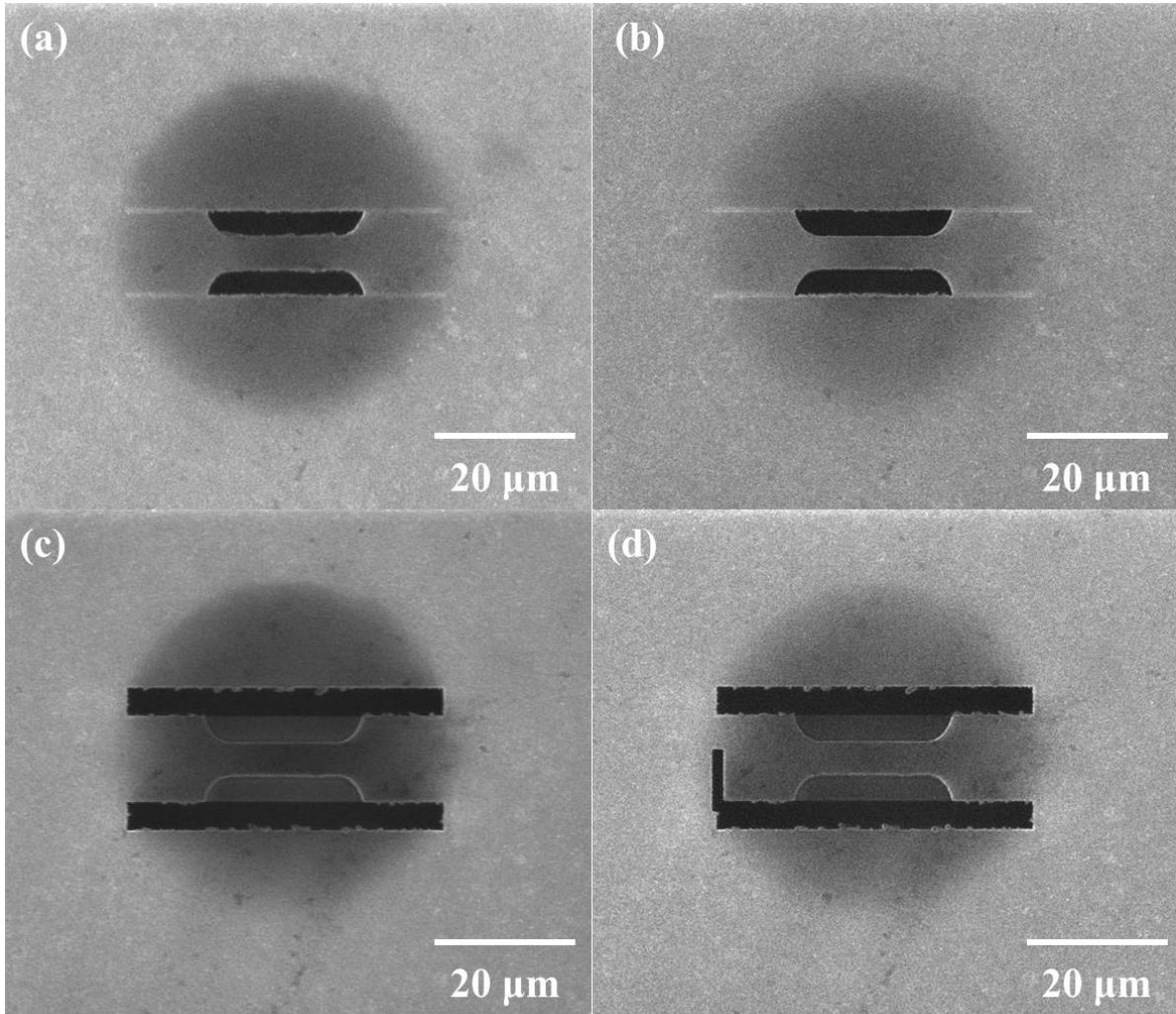
Figure 3.18. Fabrication process of samples for tensile test of MAPbBr$_3$ using focused ion beam milling process. (a) Fabrication of gauge section, (b) cleaning gauge section, (c) fabrication of grip section, and (d) fabrication of cutting area.

3.5.2 Correction method of machine and device compliance for in-situ tensile test

Micro-tensile tests were performed to measure accurate elastic limit of MAPbBr$_3$. When a tensile test is performed using a push to pull device, the load acting on the sample and the stiffness of the device are measured together. Calibration is required to use only the load applied on the sample. As shown Figure 3.19, The load displacement graph is divided into five sections such as approaching, loading with sample, loading without sample after fracture, and unloading with and without contact. In range of loading with sample, stiffness of Push-to-Pull device can be obtained by using the slope of the overlap range of the loading without sample and unloading with contact. Using the obtained stiffness, only the load acting on the sample can be obtained by excluding the load acting on the device in the loading with sample range.

Displacement obtained by equipment is measured together with device and device compliance. The strain was analyzed by digital image correlation method using real - time video obtained during the tensile test. Perovskite sample images at the start point of the experiment, immediately before fracture and immediately after fracture are shown in Figure 3.20 (a) and (b). The fracture strain of each sample was analyzed using images of same state as in Figure 3.20 (a) and (b).
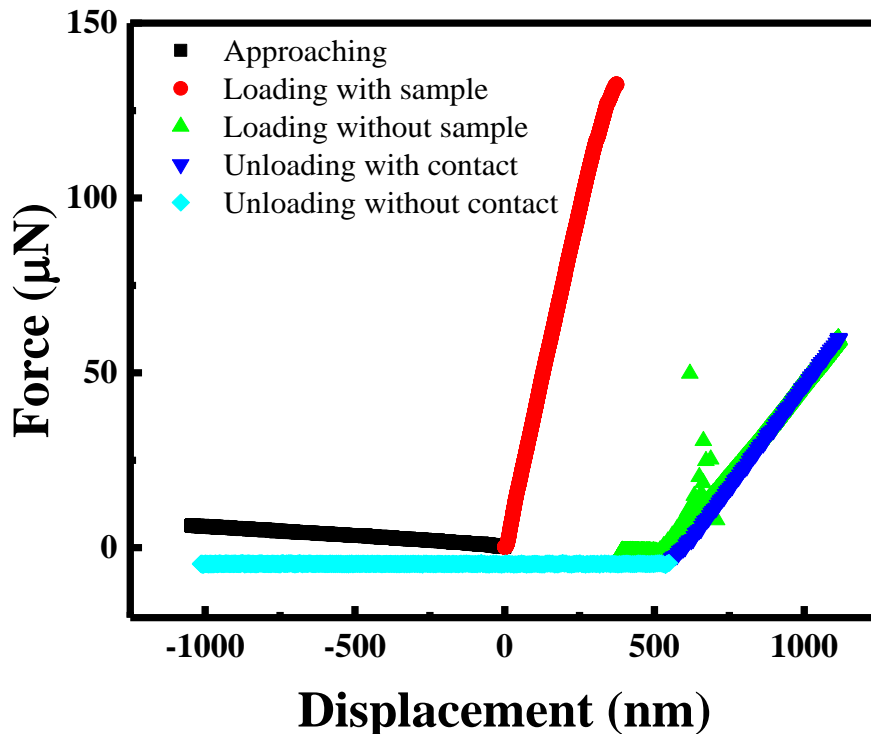
Figure 3.19. Force-displacement curve of MAPbBr$_3$ during tensile test

(a)

$\varepsilon = 0\%$

(b)

$\varepsilon = 1.2\%$

(c)

5μm
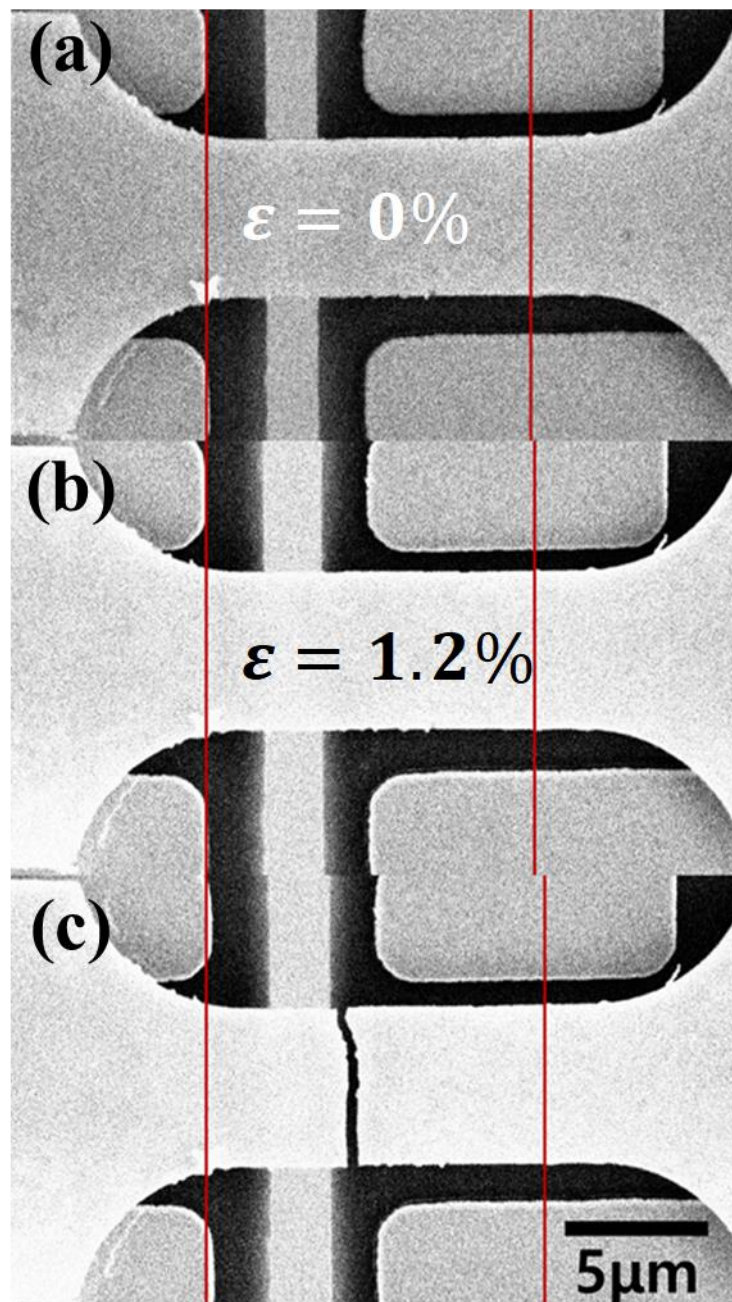
Figure 3.20. Images of MAPbBr$_3$ for tensile test at (a) starting point, (b) immediately before fracture, and (c) immediately after fracture[86].

3.5.3 Characterization of mechanical properties by in-situ tensile test

Corrected stress-strain curve is presented in Figure 3.21. MAPbBr$_3$ exhibited linear elasticity and negligibly low plasticity and fractured at a strain of 1.1 ($\pm$0.14)%. Its elastic modulus was 4.38 ($\pm$0.23) GPa and fracture strength was 45.4 ($\pm$7.5) MPa. As shown in Figure 3.22, failure occurred by intergranular fracture owing to rapid crack propagation along the grain boundaries. The grain boundary can be considered as a weak part of the perovskite.

Reported values for elastic modulus of MAPbBr$_3$ range from 17.7 to 30.2 GPa, and those for yield strength is between 103 and 120 MPa that are calculated by one third of hardness[90]. Because these values were determined through DFT calculations and nanoindentation measurements performed on single-crystalline MAPbBr$_3$, it is difficult to evaluate the properties of the MAPbBr$_3$ layer in LEDs, which contains numerous grain boundaries and defects. On the other hand, with respect to in-situ micro-tensile testing, the gauge section in the uniaxial stress state during the tests contains enough grain boundaries such that it can be considered to represent the actual MAPbBr$_3$ layer.
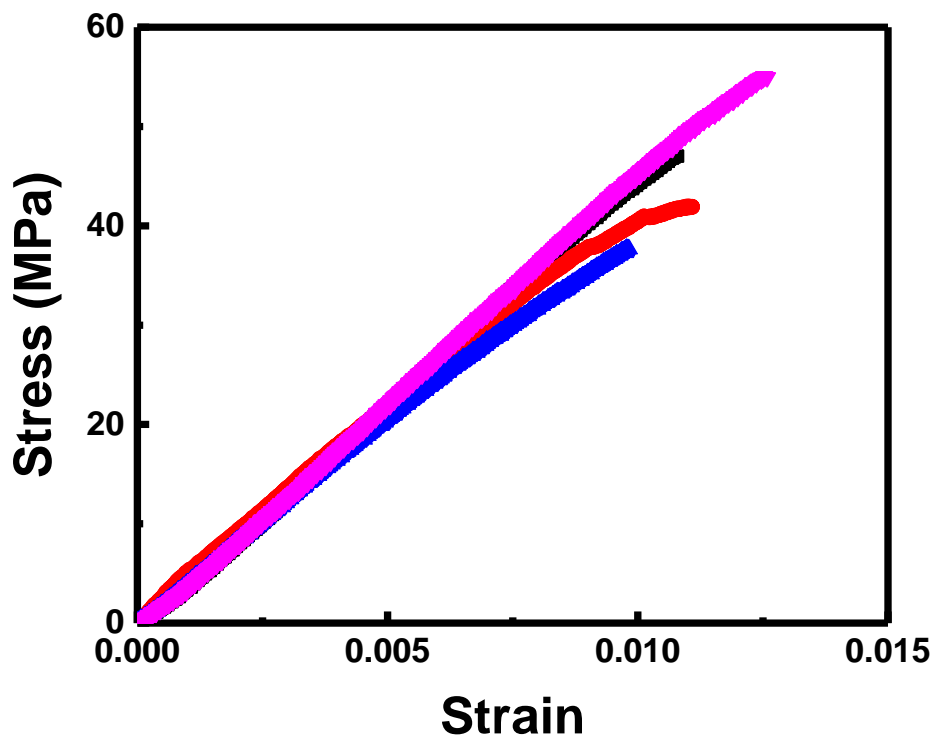
Figure 3.21. Stress-strain curves of MAPbBr$_3$
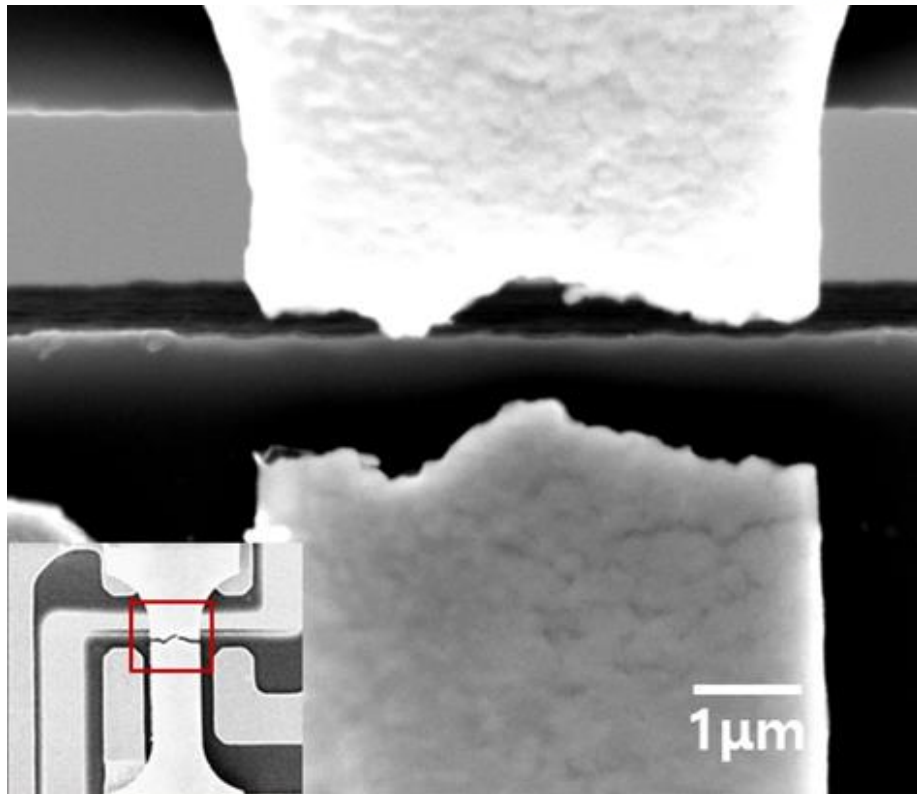
Figure 3.22. SEM image of MAPbBr$_3$ after tensile test[86].

3.6 Evaluating of critical bending radius

3.6.1 Neutral plane

Perovskite LEDs consisted of 400-nm-thick MAPbBr$_3$, 50-nm-thick PDZ, 40 nm-thick SPW-111, 50-μm-thick NOA used as encapsulation material, and 70-μm-thick PET substrate. Neutral axis can be obtained by equation as

$$t_b = \frac{-E_s t_s^2 + \sum_{i=1}^{n} E_i t_i (2h_{i-1} + t_i)}{2(E_s t_s + \sum_{i=1}^{n} E_i t_i)}, \tag{3.5}$$

where E and t are elastic modulus and thickness of constituent materials[30, 31]. Elastic modulus of PDZ and SPW-111 measured by hole-nanoindentation, elastic modulus of perovskite measured by tensile test and typical elastic modulus of NOA and PET were used for analysis, respectively. The position of the neutral line was analyzed to be located at position x from the top surface of the substrate.

3.6.2 Critical bending radius

The critical bending radius, r_c, is given by

$$r_c = (d_f + d_n)/\varepsilon, \tag{3.6}$$

where d_f is the thickness of the film (i.e., the thickness of the MAPbBr$_3$ layer) and d_n is the distance from the neutral plane to bottom surface of film. The distance from the neutral line to the perovskite was 10 μm, the thickness of the film 400 nm and the breakage strain 1.1% were used for the calculations.

The critical bending radius, r_c, of the MAPbBr$_3$ layer in the FSPeLEDs was calculated to be 0.96 mm. As described above, the luminance of FSPeLEDs decreased gradually by cyclic bending tests for r_b of 1 mm, but not for an r_b of 2.5 mm. Bending radius of 1 mm is close to calculated critical bending radius, rc of 0.96 mm, which suggests that the observed decrease in the luminance of the FSPeLEDs for bending radius of 1 mm is most likely caused by the gradual introduction of local fractures in the MAPbBr$_3$ layer.

4. Flexibility of silica for encapsulation substrate

4.1 Fabrication of Silicon dioxide thin film by sol-gel process

4.1.1 Materials

The tetraethyl orthosilicate (TEOS, Alfa Aesar), isopropyl alcohol (IPA, Omnisolv) and distilled water (H$_2$O, Omnisolv) were obtained commercially and used without further purification. Hydrochloric acid (J.T. Baker) was used for the catalyst, and 300 μm thick double side polished silicon wafer (Cemat) was used as the substrate.

The following materials were used to make OLEDs for the exposure test. All the reagents, namely, NOA63 (Norland Optics), super yellow light-emitting PPV copolymer (Merck Co.), sulfuric acid (J.T. Baker), PEDOT:PSS (PH1000, Clevios), and AgNWs (1.0 wt% IPA suspension, Nanopyxis), were used as received without further purification.

4.1.2 Silicon dioxide thin film fabrication

The synthesis of sol-gel solution was mixed in Teflon jar. The mixed solution was soaked in 80°C water for 3 hours while stirring at 500 rpm. The hot plate was protected with a windshield to prevent the influence of wind in the hood during the soaking process. The prepared solution was transferred to a vial and aged for 4 days. Prior to coating process, aged solution was filtered twice with a 0.45 μm and 0.20 μm PVDF filter, respectively. After the filtration process, spin-coating process was performed using spin-coater maintained for IPA condition for 20 minutes or more to prevent volatilization of IPA solution because the IPA easily evaporated in the air. The filter process and the maintenance of the IPA condition in the spin coater are essential processes for reducing the number of defects present in the silicon dioxide film and uniformly coating of the film. The defect image of the sample with and without the filter process and IPA condition is shown in Figure 4.1. The solution was dropped on the substrate using a disposable syringe and sol-gel solution was spin-coated onto 30 × 30 mm^2 silicon substrates at 2000 rpm for 40 s. Next, coated samples were annealed at 1000°C for 1 hour in nitrogen flow condition by tube furnace (TF-500H, Intech). After the heat treatment, the sample was immediately cooled in air and then subjected to sample cleaning. As indicated in the critical thickness theory mentioned earlier, the thickness may be thinner in order to improve the mechanical properties of the silicon dioxide thin film. However, in case of sol-gel process, ununiformly nanoparticles are produced in the solution. Because these nanoparticles are difficult to remove completely through the filtering process, they remain in solution and act as impurities in the heat treatment process to form a crack. Therefore, silicon dioxide thin film was coated to several layers for fill the generated defects, and then stacked layer was formed as a single layer through a heat treatment process. Schematic of coating

process was shown in Figure 4.2. The same coating and heat treatment process was repeated three times without last heat treatment. Finally, densification was performed on fabricated samples at 1000 °C for 4 hours in nitrogen flow condition by tube furnace.

All mechanical properties and moisture permeability measurements except transmittance measurement samples were based on this sample. The transparency measurement sample was prepared in the same manner by changing the substrate to a quartz sample. the entire fabrication process of the silica thin films is described in Figure 4.3.
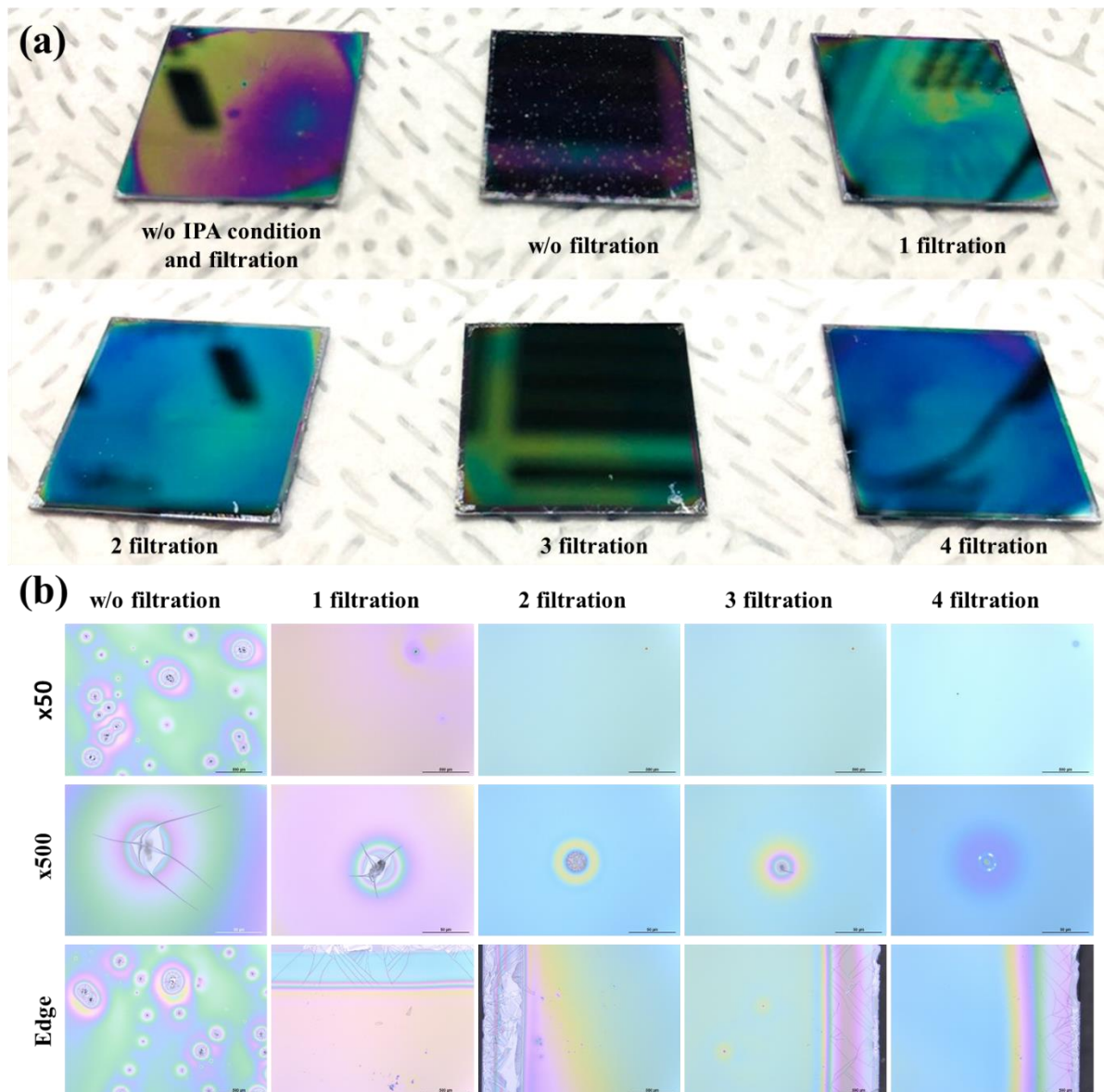
Figure 4.1. (a) Entire sample images of surface change by filtration and coating condition. (b) images of surface change of silicon dioxide thin films by filtration process measured by optical microscopy.

| 1st layer coating | 2nd layer coating | 3rd layer coating | Densification |

0h 1h 2h 3h 4h 5h 6h 7h 8h 9h

Solution filtration & Coating   Annealing   Densification
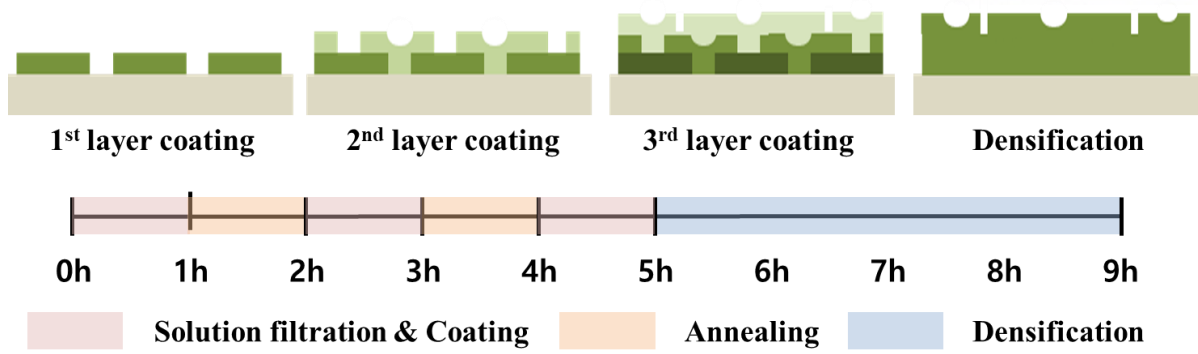
Figure 4.2. Schematic of multi-layer coating process for filled defect on silicon dioxide thin film

Metal Alkoxide Solution → Hydrolysis Polymerisation → Sol → Coating → Xerogel film → Heat → Dense Film
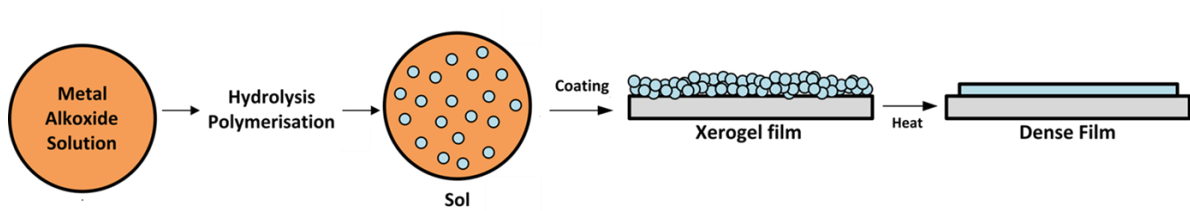
Figure 4.3. Schematic of fabrication process of sol-gel for silicon dioxide thin films.

4.2 Microstructure and optical properties of silicon dioxide thin films

4.2.1 Characterization of silicon dioxide thin film

  Morphology and elemental composition of silica thin films are determined by SEM (Nanonova 230, FEI). The roughness of silicon dioxide thin films was measure using atomic force measurement (Multimode V, Veeco). The microstructure of silicon dioxide thin films was confirmed by high-resolution transmittance electron microscopy (JEM-2100F, JEOL). Ultraviolet-visible-near infrared spectrometer (UV-1800, Shimadzu) was used to measure transmittances.

4.2.2 Microstructure and elemental component of silicon dioxide thin films

  Images measured by scanning electron microscopy are shown in Figure 4.4 and elemental components are summarized in Table 4.1. Samples for SEM and elemental component measurement were fabricated by undercut process using XeF_2 etcher (Advanced Communication Device, CA, USA) Elemental components of thin films were measured with silicon substrate and without silicon substrate, respectively. In the region where the substrate is present, the atomic ratio of Si and O is 68 at% to 32 at%, and the atomic ratio of Si and O is 37 at% to 63 at% in the region without the substrate. It is considered that the ratio of Si is high because secondary electrons are measured up to the Si molecules of the substrate during the component analysis. In the free-standing film region, the ratio of silicon to oxygen is about 1: 2, indicating that the silicon dioxide thin film is well formed.

  Sample image for TEM measurements and image and diffraction pattern of silicon dioxide thin films measured by transmittance electron microscopy is shown in Figure 4.5. Samples for TEM measurement were fabricated by focused ion beam system using XeF_2 etched sample and transferred to TEM grid using Ohmniprobe manipulation system. TEM measurements were performed at 300keV. No evidence of grain boundaries or crystallinity was observed in the images, and the diffraction pattern was ring-shaped, indicating that the microstructure of the silicon dioxide thin film was amorphous.

Table 4.1. Element components of silicon dioxide thin films with and without silicon substrate.

Element component	Si	O
With silicon substrate	68 at.%	32 at.%
Without silicon substrate	37 at.%	63 at.%
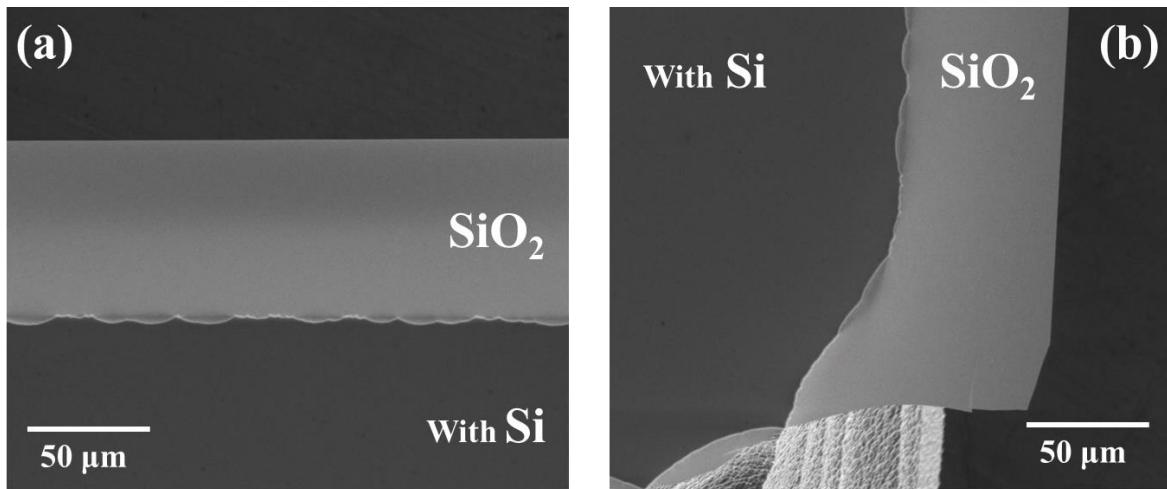
Figure 4.4. (a) Top view image and (b) tilt view image of free-standing silicon dioxide thin films images measured by scanning electron microscopy after XeF$_2$ etching process.
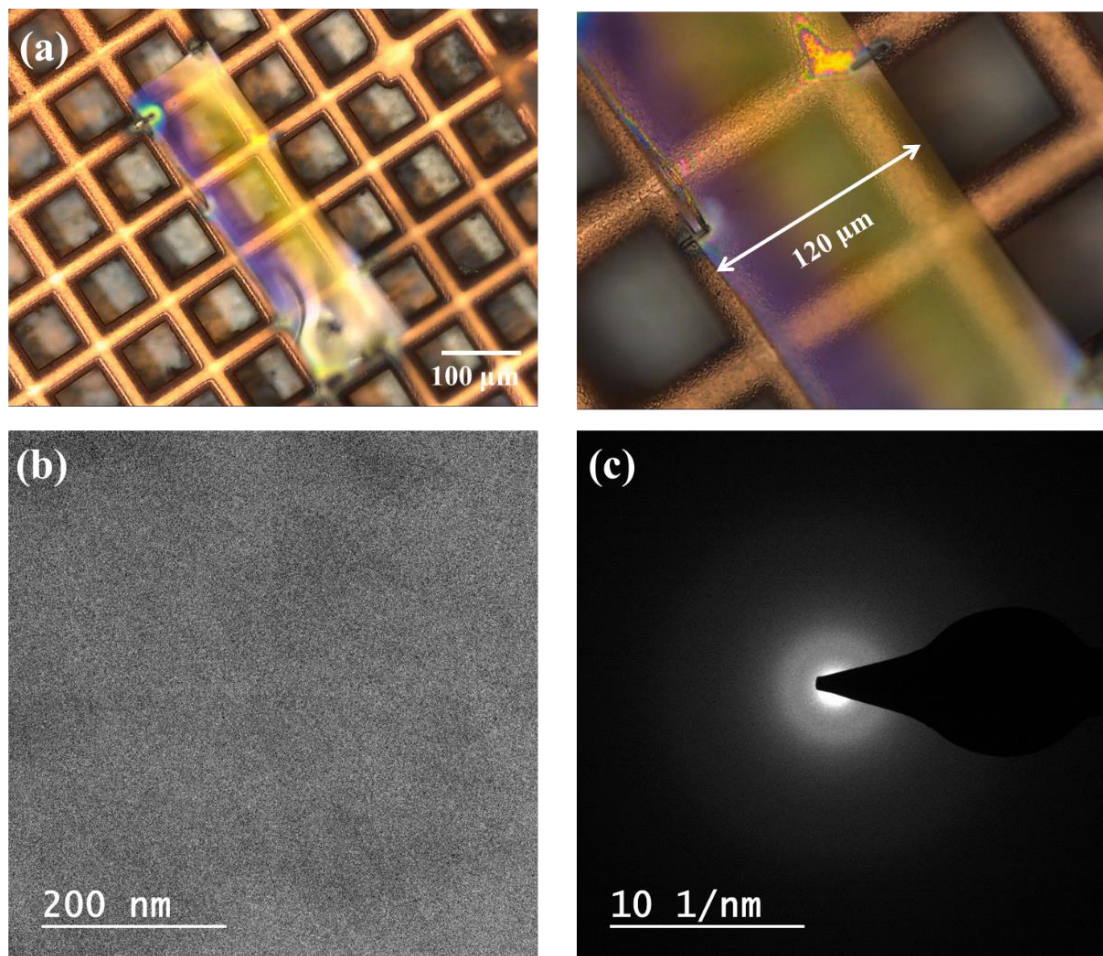
Figure 4.5. (a) Optical microscopy images of silicon dioxide thin films on TEM grid. (b) High resolution image and (c) diffraction pattern of silicon dioxide thin films measured by TEM.

4.2.3 Surface roughness of silicon dioxide thin film

If the roughness of the material is relatively high relative to the thickness, it may affect the reflection of light and mechanical deformation behavior. It is important to minimize surface roughness. The roughness of the fabricated silicon dioxide thin films was measured as 0.157 ± 0.008 nm and image of roughness measurement are shown in Figure 4.6.

4.2.4 Optical property of silicon dioxide thin film

Images of transparency measurement samples and graph of transparency of silicon thin films coated on quartz substrate are shown in Figure 4.7. In shown Figure 4.7 (b), the cracks in the thin film at the corners of the substrate were formed during the heat treatment process by thick coating of the thin film during the silver spin coating process. Transmittance of silicon dioxide thin films were measured in range of 400 nm to 780 nm. Transparency of the quartz substrate was also measured in the same manner as the reference sample. The measured transmittance of silicon dioxide samples was normalized by using the transmittance of the quartz substrate and was shown Figure 4.7 (c). The transmittance of the silicon dioxide thin film was analyzed with a transmittance of about 99% compared to the quartz substrate at 550 nm. It can be seen that silicon dioxide thin film has high transparency and does not sacrifice transparency when used as a sealing material.

4.2.5 Thickness of silicon dioxide thin film

Thickness of silicon dioxide thin films was measured at 700 nm by thickness measurement ST4000-DLX (K-MAC, Korea).
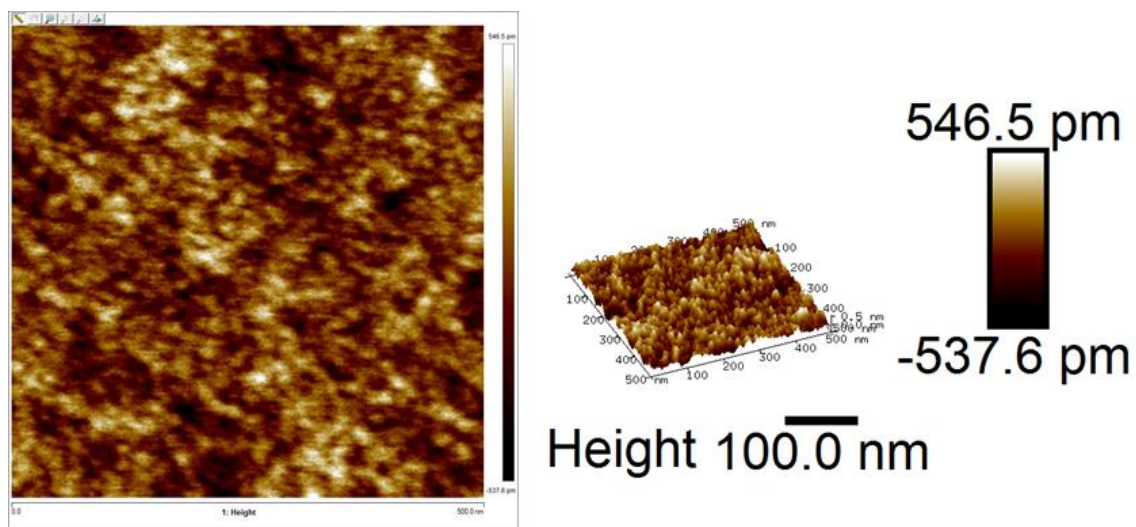
Figure 4.6. Image of 2D and 3D AFM measurement result of silicon dioxide thin films.
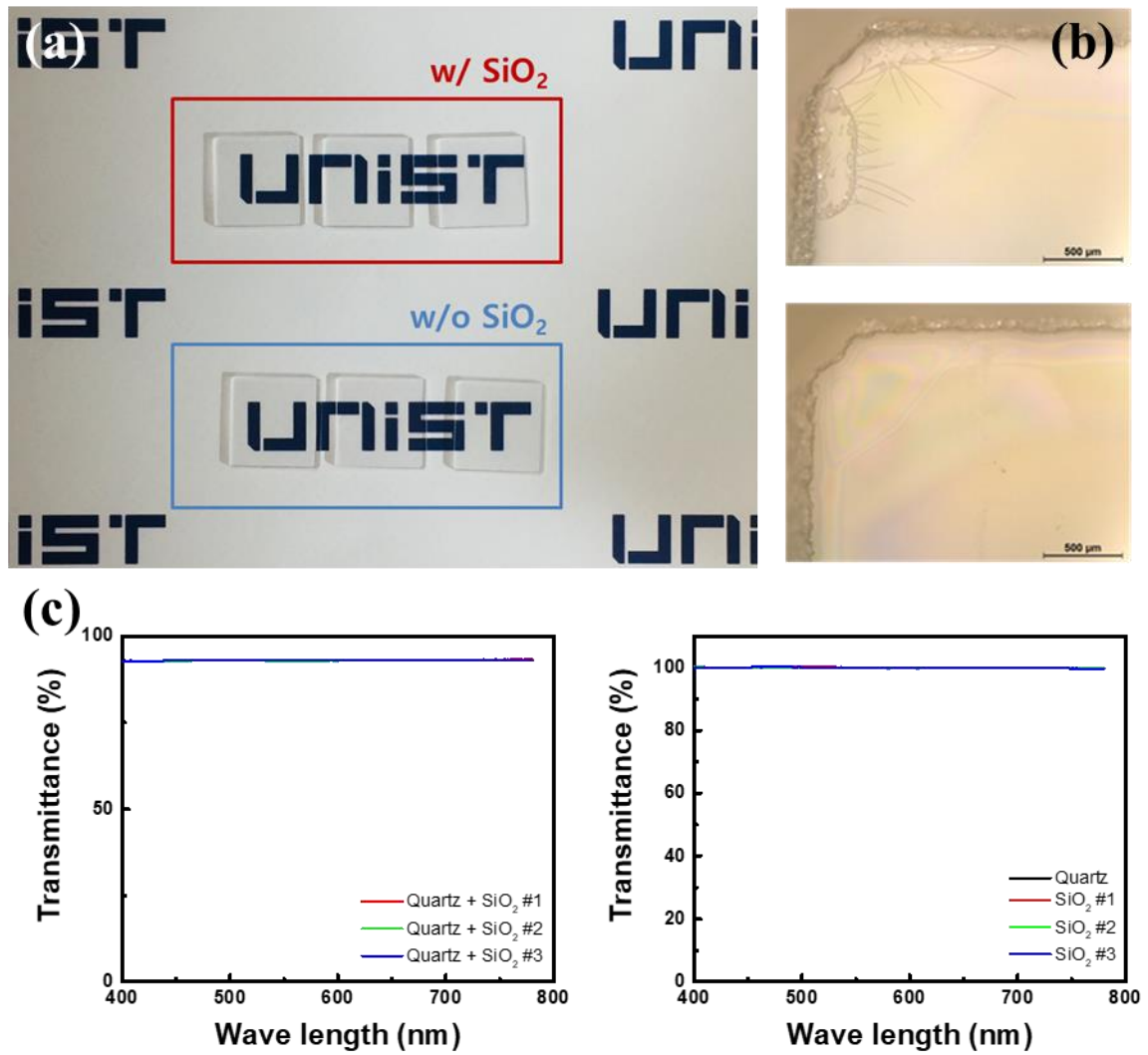
Figure 4.7. (a) Photograph image of samples for transparency measurement samples and (b) image of corner portion of silicon dioxide thin films on quartz substrate (upper) and quartz substrate (lower) measured by optical microscopy. Graph of transmittance of silicon dioxide thin films on quartz substrates (left) and normalized silicon dioxide thing films (right).

4.3 Permeability properties of silicon dioxide thin films

4.3.1 Fabrication process silicon dioxide samples for WVTR measurement by MOCON

In order to use the silicon dioxide thin film prepared by sol gel process as an encapsulating material, the moisture permeability of the thin film should be analyzed. Schematic of fabrication process for water vapor transmittance rate was shown in Figure 4.8.

In order to measure the moisture permeability with MOCON, the area of free-standing silicon dioxide film should be over 5cm^2. Free-standing area was obtained by forming a hole in a silicon substrate on opposite side of silicon dioxide coated surface. In the center of the sample, a hole mask was patterned by photo-resist, followed by deposition of chromium, followed by a lift-off process to form a hard mask for the etching process. NOA61 (Norland Optics) was coated on silicon dioxide layer at 500 rpm for 40 s and cured by UV light. NOA was used as a supporting layer because silicon dioxide thin films were easily broken in a free-standing state. Silicon substrate was etched in a hole shape until the remaining thickness was about 10 to 20 μm. Finally, residual silicon was removed by XeF$_2$ etching process.

Entire sample and optical microscopy images were shown in Figure 4.9. The phenomenon of wrinkling formation in the free-standing area was caused by residual stress in the silicon dioxide thin film. In the sol-gel process, silicon dioxide is coated in a solution state and changed to a thin film form at 1000℃, and then cooled to room temperature. Residual stress is occurred due to the difference in change of volume caused by the difference in coefficient of thermal expansion between silicon substrate and silicon dioxide thin films. Since the silicon has a higher thermal expansion coefficient than silicon dioxide, compressive residual stress is generated in the silicon dioxide thin film during cooling process.

On the other hand, in the case of NOA coated on the silicon dioxide thin film, a volume reduction occurred in the UV curing process, and a tensile residual stress was generated in the silicon dioxide thin film. The tensile residual stress depends on the thickness of the coated NOA61. The residual stress generated in the silicon dioxide thin film can be offset by controlling the thickness of NOA61. When NOA was coated with millimeter thickness by casting method, tensile residual stress was generated more than compressive residual stress and cracks were formed on silicon dioxide thin film. When the thickness of NOA was very thin by spin coating at high rpm, the wrinkle structure was formed due to the compressive residual stress. The NOA thickness was optimized to control the residual stress to obtain a flat silicon dioxide thin film.
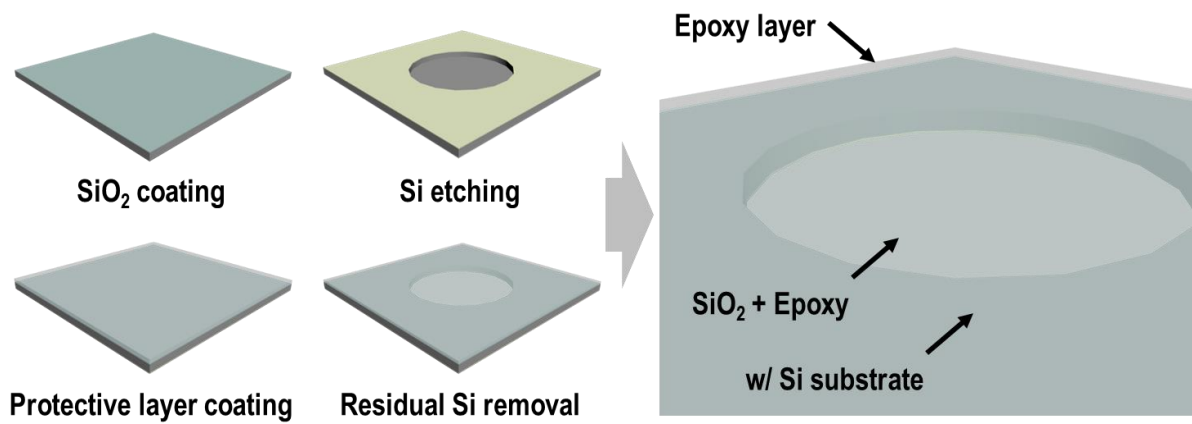
Figure 4.8. Schematic of sample fabrication process for water vapor transmittance rate by MOCON.
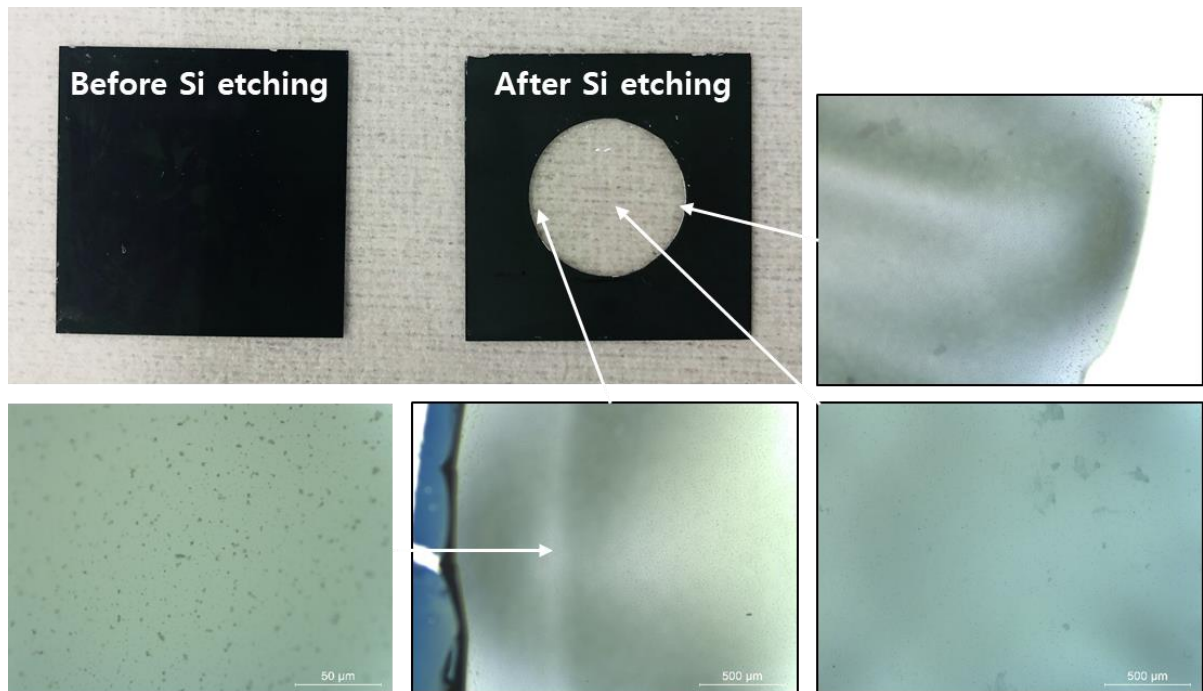
Figure 4.9. Entire image and optical microscopy images of samples for water vapor transmittance rate by MOCON.

4.3.2 Water vapor transmittance rate of silicon dioxide thin films

Water vapor transmittance rate was measured by MOCON. For accurate measurements, sample was attached to aluminum supporting foil to prevent passage of moisture outside open area. The measurement was carried out at a relative humidity of 100% and a temperature of 23°C. The amount of water permeated through the membrane was analyzed at intervals of 30 minutes to 1 hour.

Generally, when water vapor permeability is measured by MOCON, if more than three points of the measured results show similar values, the value can be regarded as the moisture permeability of the sample. The graph of measurement results was shown in Figure 4.10 and water vapor transmittance rate was measured as 1.5×10^{-2} g/m^2 · day. The WVTR value was measured with the silicon dioxide thin film on the NOA film. WVTR of the NOA substrate was found to be within the range of several grams, measured WVTR values is specified as the WVTR value of the silicon dioxide thin film.

However, the WVTR value of 1×10^{-6} g/m^2 · day required for encapsulation materials for organic light emitting diodes was still insufficient. The defects formed by silicon dioxide nanoparticles in the sol-gel solution were covered by multilayer coating and densification process, but defects were not completely covered and acted as the penetration path of the water. If the thickness of the silicon dioxide thin film is increased to completely remove the defect, a lower WVTR value can be obtained. However, when the thickness is increased, the elastic limit is expected to be lowered. It is expected that it will be appropriate to extend the moisture permeation path by using a multilayer structure with organic materials to improve the moisture resistance. However, only the monolayer was studied in this study.
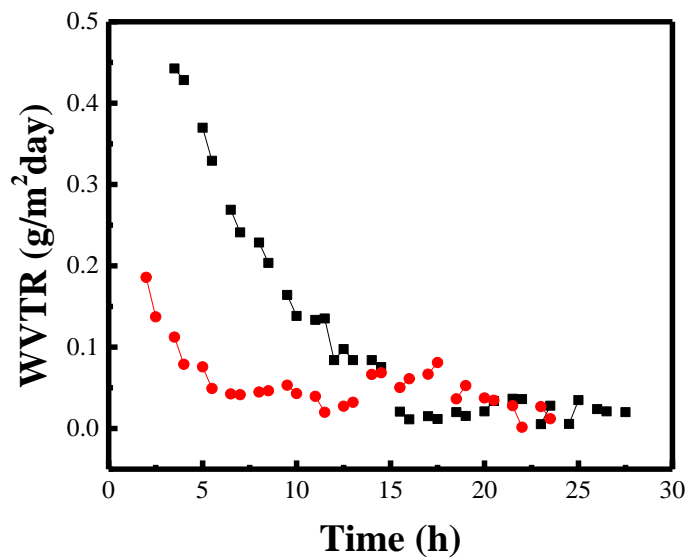
Figure 4.10. Graph of water vapor transmittance rate of silicon dioxide thin films by MOCON.

4.4 Mechanical properties of silicon dioxide thin films

4.4.1 Sample fabrication process and testing condition of in-situ micro tensile test

To measure accurate tensile properties through tensile test, it is necessary to prepare samples in exact form so that the load and strain can be analyzed by uniform deformation in a specific area. Tensile test specimen of dog bone shape was prepared for in-situ micro tensile test to measure the mechanical properties of the silicon dioxide thin film. Schematic of fabrication process was shown in Figure 4.11. After cutting the center of coated sample, cut side surface of silicon substrate was etched to an enough extent to produce a tensile sample using the XeF_2 etching process. The silicon dioxide thin film was cut into a rectangular shape using a focused ion beam and then transferred to Push-to-Pull device with 15μm device gap using an Omni-probe manipulation system. Since the thin silicon dioxide thin film is highly affected by the electron and ion beam, the beam current was minimized to a maximum of 50 pA during the sample preparation. The samples attached to the device were fabricated into dog shapes using the ion milling process. First, the shape of the grip part was made with a high current (50 pA). Then, the fine milling was performed by using a low current (30 pA) to remove defects generated in the milling process in the gauge section. Images of fabrication process were shown in Figure 4.12. Geometry of fabricated sample for micro tensile test was 6 μm in gauge length. The size of the sample was made according to the standard tensile specimen specification, and the length of the gage portion was set according to the thickness of the sample.

The tensile test was carried out using a PI-87 pico-indenter installed in the SEM, and the tensile test was conducted out until fracture at a displacement speed of 6 nm s^{-1} (strain rate: 10^{-3}/s). The test was carried out after waiting for 10 minutes with alignment to prevent drift effects. In order to analyze exact elastic limit, a repeated tensile test was carried out by dividing interval in units of 100 nm. For actual strain analysis, the tensile test procedure was recorded as a video in real time.
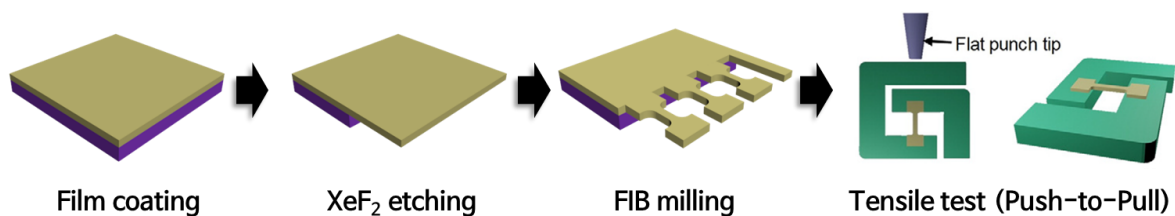
Figure 4.11. Schematic of sample fabrication process for in-situ micro tensile test.
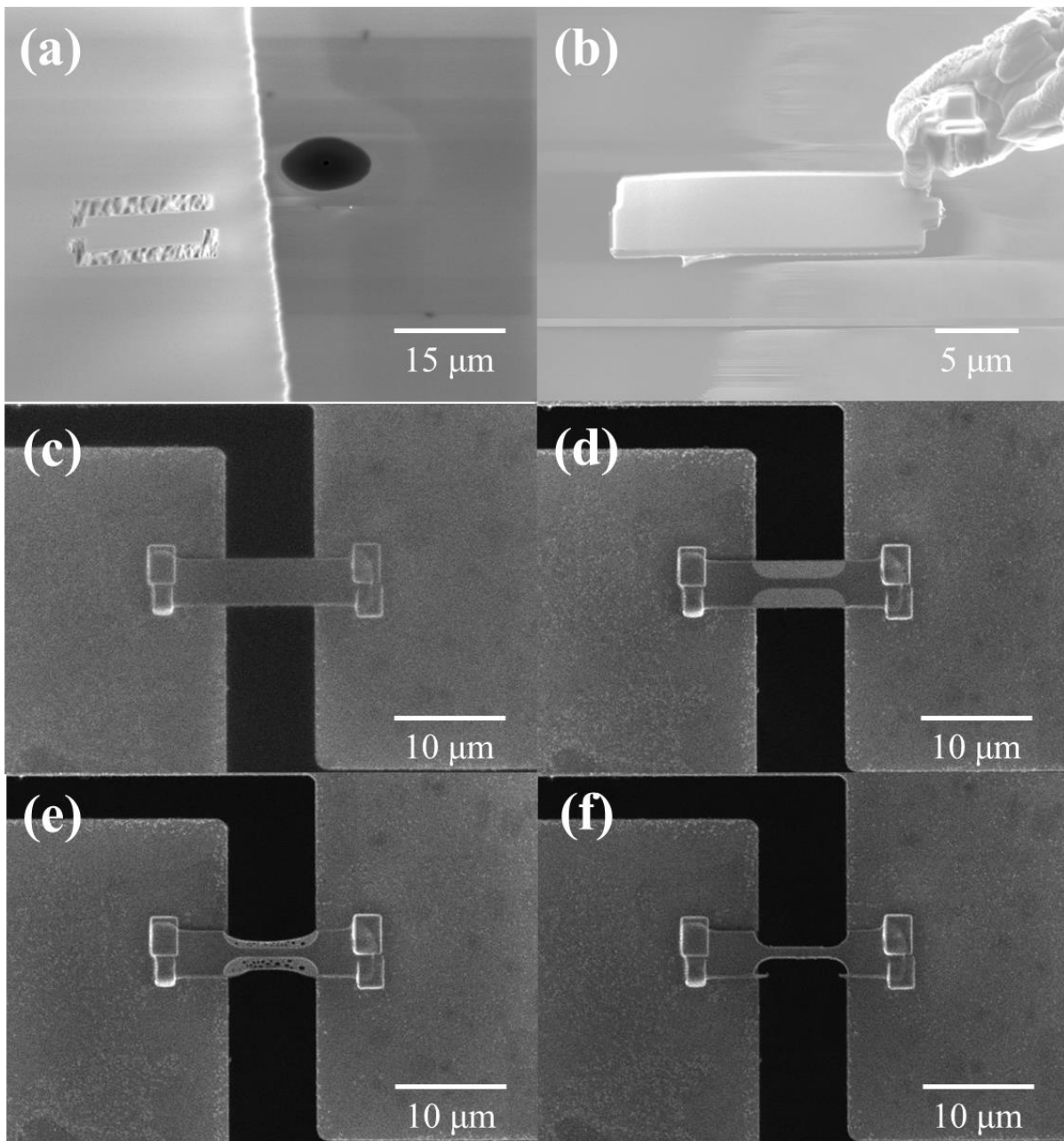
Figure 4.12. Image of fabrication process for tensile test sample by FIB. (a-b) The silicon dioxide thin film is cut into a rectangular shape and attached to the omni probe to move to the device. (c-f) Patterning for dog-bone pattern on the Push-to-Pull device and fine-milling on the gauge section.

4.4.2 Result of in-situ micro tensile test

The tensile test was carried out using dog-bone shaped sample shown in Figure 4.13. As results of repeated tensile tests, reproducible data was obtained and described in Figure 4.14 (a). When a tensile test is conducted using a Push-to-Pull device, the device's stiffness is measured simultaneously with the load applied to the sample. Stiffness of the device was measured in the absence of a sample and the actual load value was corrected. Since the strain and strain can be measured with the equipment and the compliance of the device, the actual strain is analyzed by performing the digital image correlation analysis using the still shot obtained from the video shot in real time. The stress-strain curve was described by correcting load and strain values to acting on actual sample.

Silicon dioxide thin film undergoes elastic deformation until the fracture and fracture occurs through the brittle fracture. Its elastic modulus was 88.65($\pm$10.37) GPa and fracture strength was 2.7 ($\pm$2.3) GPa. As shown in Figure 4.15, failure occurred by brittle fracture behavior owing to rapid crack propagation. As mentioned in section 2.7, the elastic modulus of the silicon dioxide thin films reported in previous studies was 59 to 85 GPa and the fracture strength was 350 to 2067 MPa. The fracture strain of the silicon dioxide thin film was high in this experiment because the thickness of the material was relatively thin compared to the material measured in the previous experiment. Generally, when a load is applied to a material, a defect such as a pinhole or a grain boundary existing in the material acts as initiation point of the crack. The generated crack propagates, and the sample is broken. As the thickness of the material decreases, the defects in the sample are stochastically decreased and the strength is increased.

For materials used as general structural materials, the elongation at break is important. However, when applied as an encapsulating material in a flexible device, since the device can be degraded due to moisture penetration through a crack generated by plastic deformation, the elastic limit that can be deformed without causing breakage is important. Since the material in the stress-strain curve shows elastic deformation behavior, plastic deformation may occur at the same time. To analyze the exact elastic limit, a cyclic loading tensile test was carried out with increasing displacement by 100 nm. As loading curves of repeated tensile test shown in Figure 4.14 (b). Repeated tensile tests were performed by fully unloading and reloading the device to the point where the tip and the tip were completely separated, and the load became zero. In graph of cyclic loading test, the unloading curves of the repeated tensile test procedure were excluded because they did not overlap because of machine compliance. The machine compliance of the loading curve corrected the stiffness of the device, indicating only the load acting on the actual sample. From the results of the repeated tensile test, it was confirmed that the loading curves all overlap to the breaking point of the material. Based on these results, silicon dioxide thin film was elastically deformed to the fracture. The elastic limit obtained as a result of the tensile test

is evaluated to be enough for application to a flexible device.
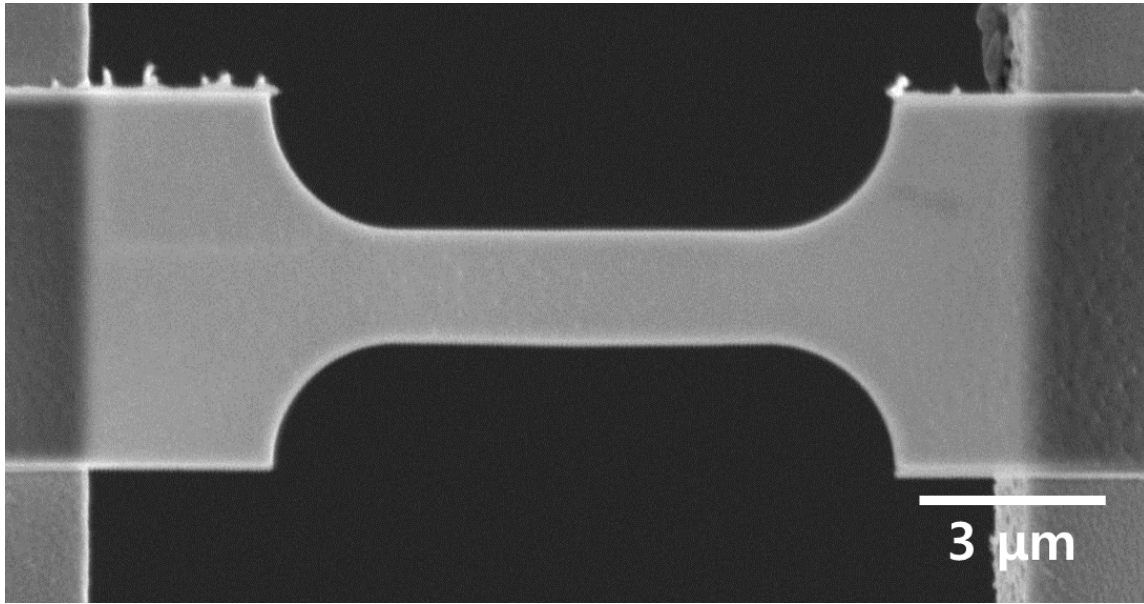
Figure 4.13. Entire sample image of silicon dioxide for tensile test sample.
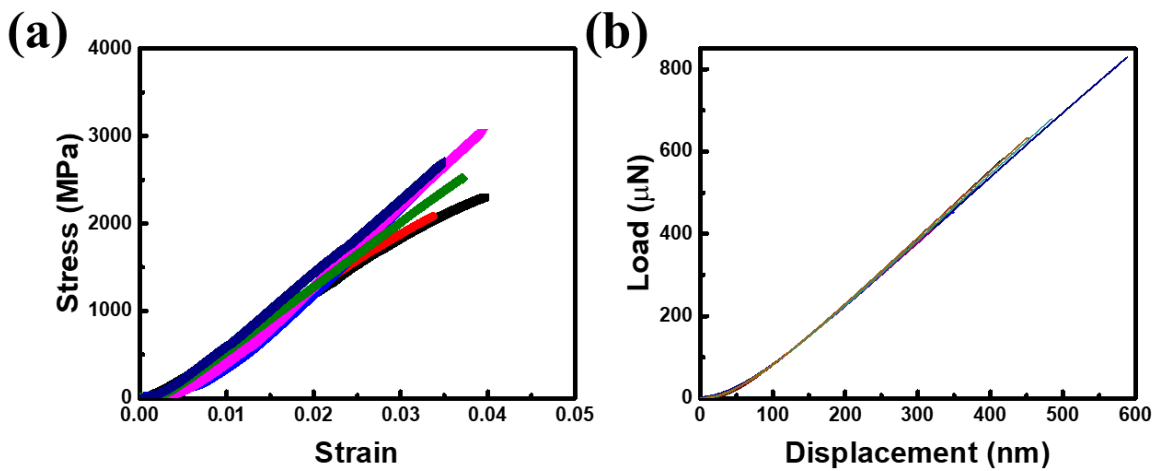
Figure 4.14. Graph of (a) tensile test result until fracture and (b) loading curve of cyclic loading test up to 600 nm in 100 nm increments.
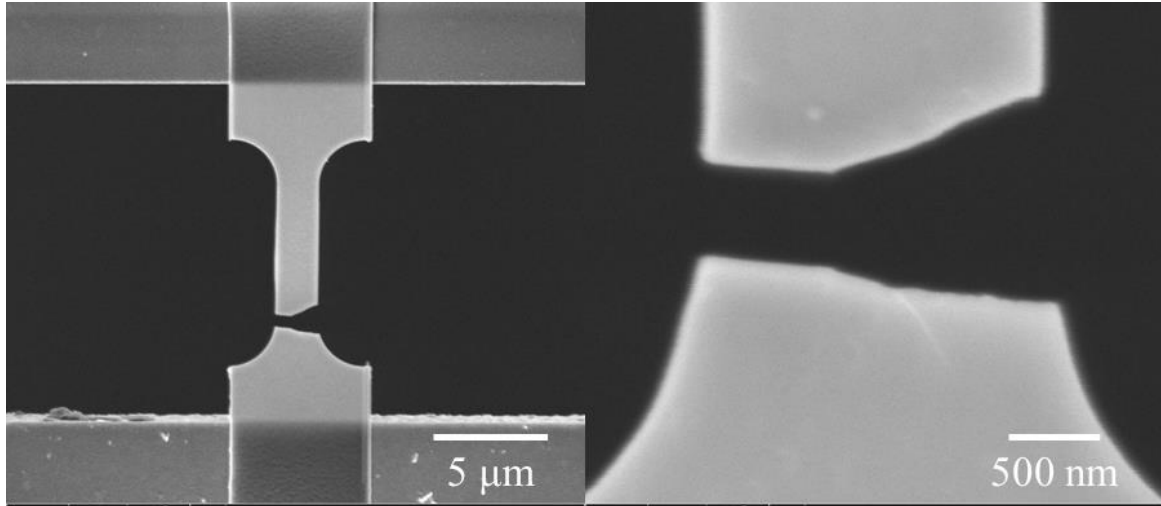
Figure 4.15. SEM image of tensile test sample (left) and fracture area in gauge section after tensile test (right).

4.4.3 Electron beam effect on silicon dioxide thin films

In the case of the silicon dioxide thin film, many studies have been made on the difference in deformation behavior when exposed to electron beam in the measurement of mechanical properties. In general silicon dioxide thin films have low elastic limit and show brittle fracture behavior, but plastic deformation occurs when deformed under electron beam exposure.

Mkhoyan et al. explained about full recovery of electron beam damage on silicon dioxide thin films[91]. Electron beam was exposed using scanning transmission electron microscopy (STEM) at 100 kV. Simultaneously recording ADF images and EELS spectra of component were also used to measure change of chemical composition in exposed area. As shown in Figure 4.16, electron-beam-induced damage was fully recovered in two minutes. The intensity difference before and after beam irradiation is shown in Figure 4.16 (f). The intensity of the damaged area immediately decreased after the irradiation and intensity of surrounding area was increased. This result indicates that the mass of damaged area was moved surrounding the damaged area without changing the total mass. ADF images and intensity were explained to the same state as before irradiation and after 2 minutes of electron beam irradiation. EELS spectrum of Figure 4.17 showed that oxygen molecules are formed by electron beam irradiation and disappear during beam-off state. The results summarized in Figure 4.16 and 4.17 established that damage generated by the electron beam formed dangling bonds pair and molecular oxygen and moves back to suitable bonding site during the beam off state.

Zheng et al. demonstrated bonding switching mechanism using molecular dynamic simulation for very thin silica wire[92]. Highlight actions of silicon and oxygen bonds were shown in Figure 4.18. Electron beam broken bonding between silicon and oxygen atoms and created dangling bond of silicon atom and non-bridging oxygen atom. Non-bridging oxygen atom formed bonding with different silicon atom and simultaneously another oxygen separated from latter silicon atom. Consequently, bonding defect generated by energetic beam impart flexibility to silicon dioxide unit cluster for rotation and relocation. Flow stress was reduced, and large ductility mediated due to bond-switching mechanism.

Mackovic et al. demonstrated influence of electron beam on mechanical properties of silicon dioxide sphere using in-situ TEM technique and finite element measurement (FEM) simulations[93]. The experiment was conducted for three case such as low-dose irradiation and beam-off compression, high-dose irradiation and beam-off compression, and high-dose irradiation and beam-on compression. As shown in Figure 4.19 and 4.20, high-dose irradiation and bean-off compression samples had a higher maximum load than low-dose irradiation and beam-off compression. This result indicates that high-dose irradiation hardened silicon dioxide sphere due to densification of silica sphere. Densification occurs due to rearrangement of the silica networks randomly arranged during beam irradiation. At this time, silica network ring clusters were transformed from 5-7-5-7 weak silica ring cluster to 6-6-6-6 rigid

silica ring cluster. On the other hand, maximum load value of compression test in beam-on state was significantly lower than that of both compression test in beam-off state. This result due to defect generation mechanism such as pairs of dangling bonds between silicon and oxygen and formation of oxygen vacancy during beam irradiation. The electron beam support defect generation and plastic deformation, reducing load required for plastic deformation of silicon dioxide sphere.
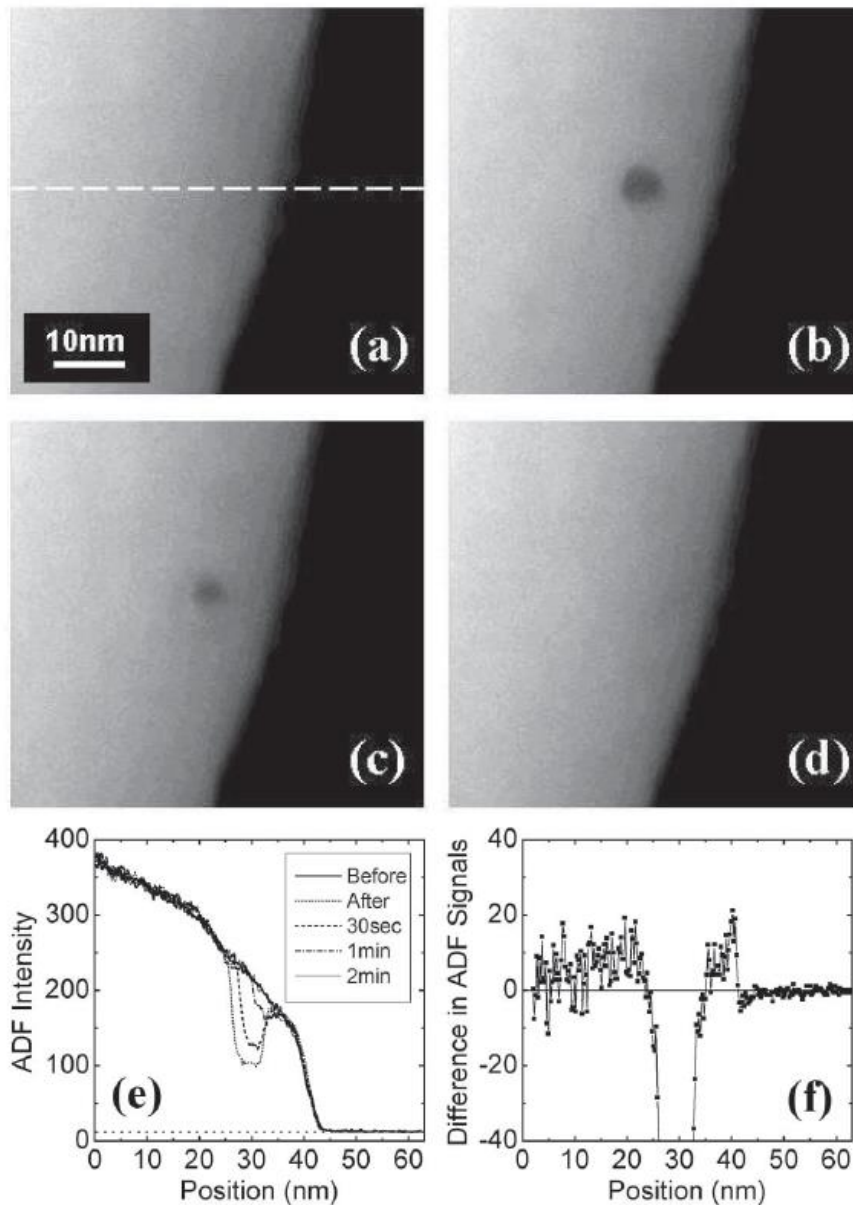
Figure 4.16. ADF images of glass particle. (a) before, (b) after 2min of electron-beam damage, (c) after 30 sec and (d) 2 min of recovery with beam turn off. (e) Line scans of ADF intensities across damaged area. (f) difference between line scans form (b) and (a)[91].
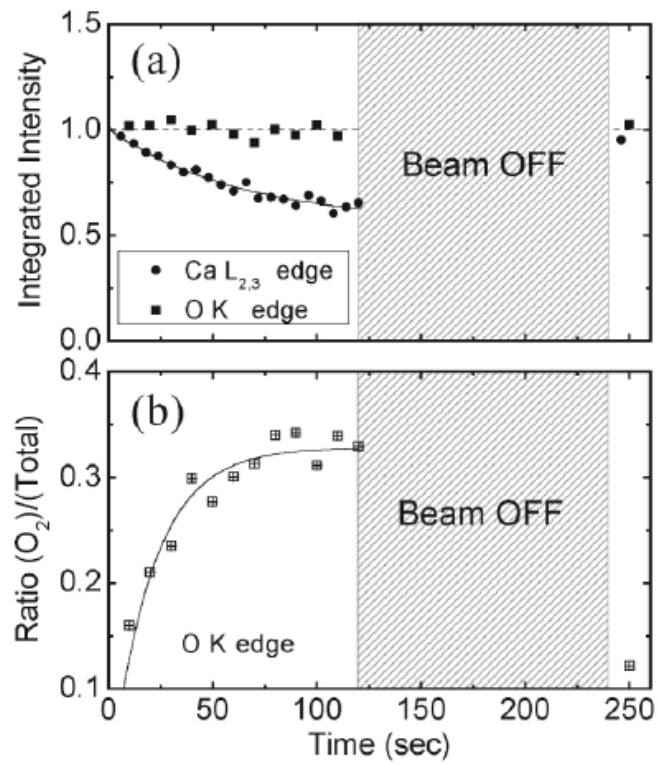
Figure 4.17. Changes in integrated intensity of Ca $L_{2,3}$ edge and O K edges with electron-beam exposure. (b) Integrated intensity ratio of the O K edge in O_2 to total intensity of O K edge[91].
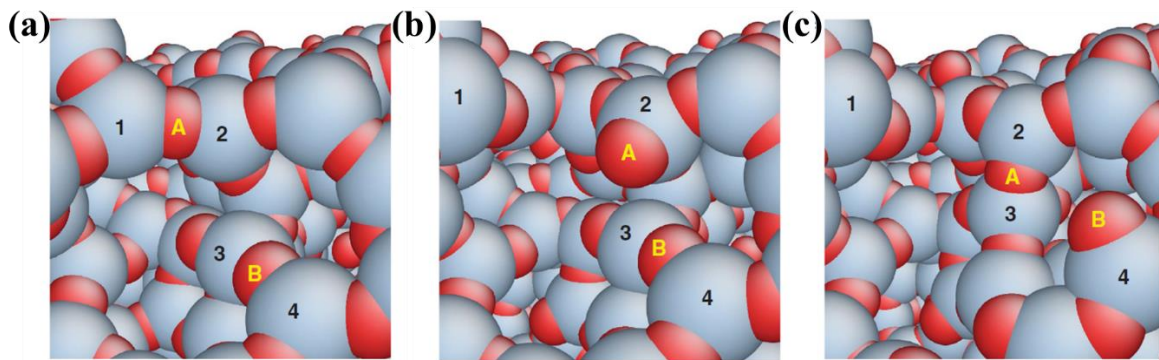
Figure 4.18. A representative bond-switching event revealed by molecular dynamic (MD) simulation[92].
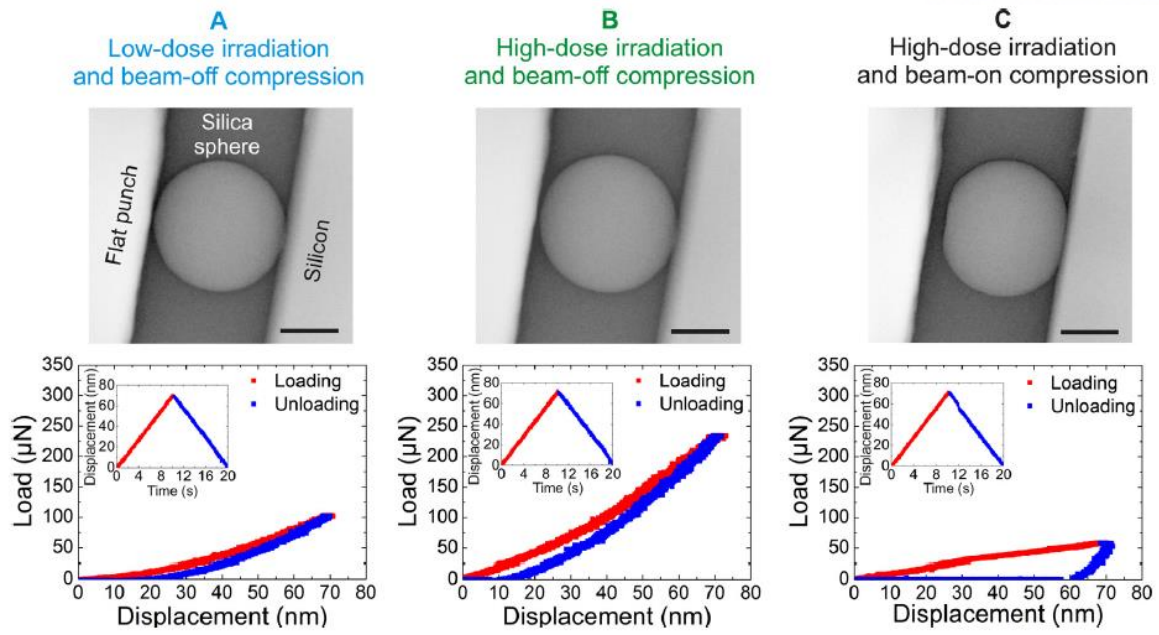
Figure 4.19. Electron beam hardening of nanoscale silicon dioxide. TEM image after compression test and load-displacement curves for each testing condition[93].
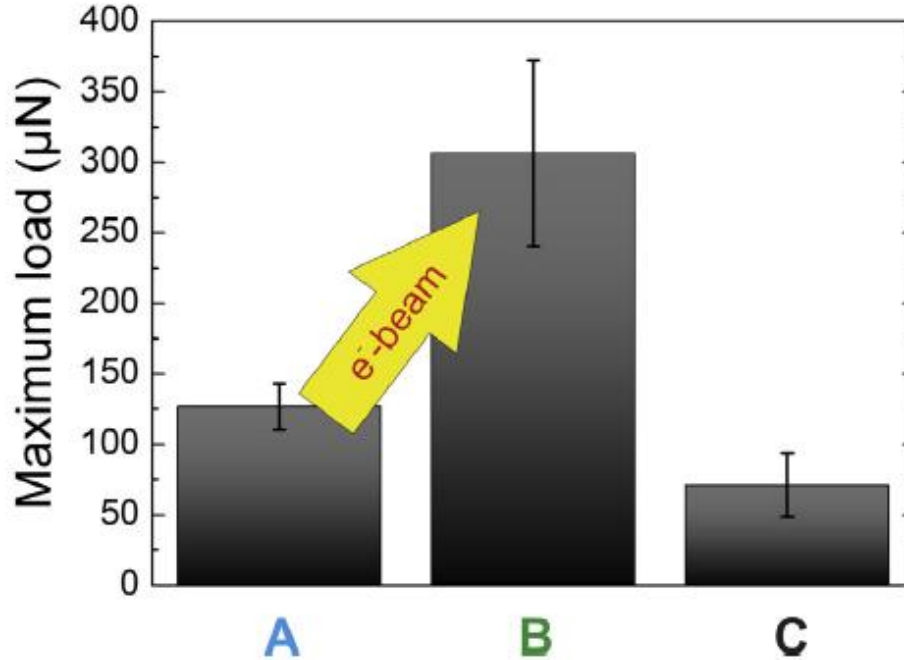
Figure 4.20. Maximum load vale of silicon dioxide spheres compression test for each testing condition[93].

4.4.4 Influence of electron beam on silicon dioxide thin films during micro tensile testing

In this study, additional tests were carried out to confirm the effect of electron beam on the silicon dioxide thin film. The sample preparation process was the same as the tensile test. Even if tensile samples are produced by the same fabrication process, since the size of the tensile test specimen is very small, it is difficult to confirm the influence of the accurate electron beam due to the difference in the sectional area where the load acts due to errors in the fabrication process. For this reason, the experiment was carried out with the electron beam on / off state using the same sample.

As shown in previous studies, bonding between silicon and oxygen separated by an electron beam is restored in a few minutes. In the beam-on state, the alignment of the device and the tip was carried out to carry out the repeated tensile test. The acceleration voltage was maintained at 5 kV in the beam on state. Using the mechanical properties obtained from the tensile test results, cyclic loading tensile tests were carried out within the range where the specimens did not break and carried out with increasing strain length at intervals of 100 nm in the same manner as tensile test method. After cyclic loading test in e-beam on condition, the electron beam was turned off to maintain the blank state for 10 minutes. The repeated tensile test was performed until fracture in the same manner as the beam on condition. In the beam off state, it is impossible to analyze the strain through video analysis. The effect of electron beam was analyzed using the load-displacement curve.

Load-displacement curves were shown in Figure 4.21. Experimental results show that the load on the sample at same displacement acts on the beam-off state higher than the beam-on state. At 200 nm and 300 nm, the load was measured as 192 and 331 μN in the beam-on state and 220 and 376 μN in the beam-off state, respectively. The load of about 10% was reduced due to the electron beam. The samples were elastically deformed, and the fracture strain was not different in the beam-on and beam-off state. The fracture strength of the silicon dioxide thin film in electron beam off condition was analyzed to be higher than that of the electron beam off condition. In this study, the elastic limit of the material is important for the application as a sealing material in the flexible element. Therefore, result obtained by the tensile test was used for the elastic limit which is not affected by electron beam.

In previous studies, experiments were performed in in-situ TEM environment with an acceleration voltage of about 300 kV. The silicon dioxide sample was affected by the electron beam and showed additional deformation behaviors such as plastic deformation and load drop which does not appear when there is no electron beam condition. In the cyclic tensile test, the acceleration voltage was kept low at 5 kV, experimental results showed only a reduction in load without any deformation behavior under beam on and off condition.
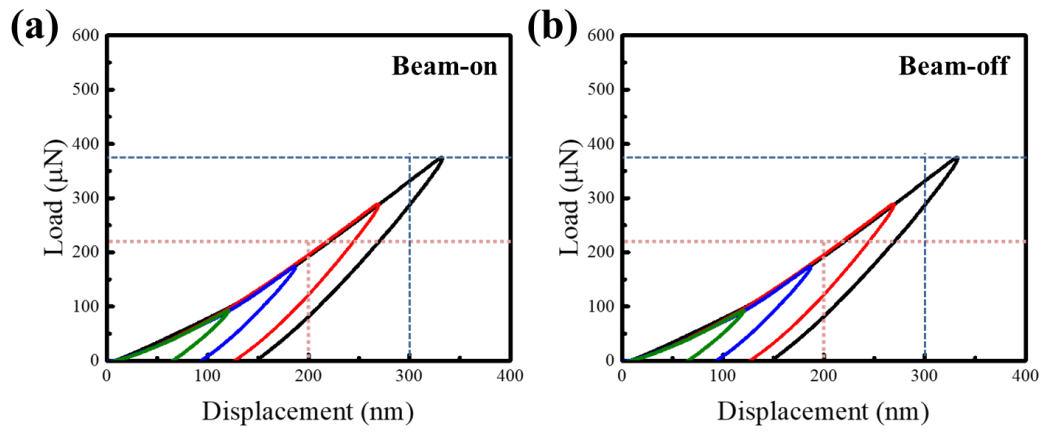
Figure 4.21. Graph of cyclic loading test of (a) beam-on and (b) beam-off condition.

4.4.5 Sample fabrication process for cyclic bending test

In the case of a flexible device, it is subjected to repeated bending deformation, so that the silicon dioxide thin film must be deformed without being broken even under repeated bending in order to be used as an encapsulating material for flexible substrate. In the case of a simple deformation, when the external force is removed below the elastic limit, it returns to its original state. However, in the case of repetitive deformation, crack is propagated by the fatigue phenomenon during repetitive deformation. Therefore, in order to be applied to a flexible device, the deformation behavior of the material should be analyzed in the repeated deformation state. For application to flexible devices, a sample separated from a rigid substrate was prepared. In this study, a silicon dioxide thin film deposited on a polymer substrate was fabricated for the repetitive bending experiment in the following manner.

Schematic of fabrication process of samples for cyclic bending test was shown in Figure 4.22. Chromium was deposited on the center of the fabricated 3×3 cm^2 sample at 1.5×1.5 cm^2 size as protective mask during following process. Opened area of silicon dioxide thin film was etched by ICP process using CF_4 and CHF_3 gas at 1500W. After removing the chrome mask, a chromium thin film was deposited at the position where the silicon dioxide thin film was removed and used as a protector layer of NOA61 during XeF_2 etching process. Silicon substrate was roughly etched in 2×2 cm^2 size on the opposite side of the silicon dioxide coated surface by Bosch process using oxygen, SF_6, and C_4F_8 gas at 3000W using deep silicon etcher. Remaining silicon substrate was etched by XeF_2 etching process. After XeF_2 etching process, chromium protector layers removed by Cr etchant. Finally, Sample was attached on SUS supporting plate by Kapton tape and was separated by cutting the NOA between silicon dioxide thin film and remained silicon substrate.
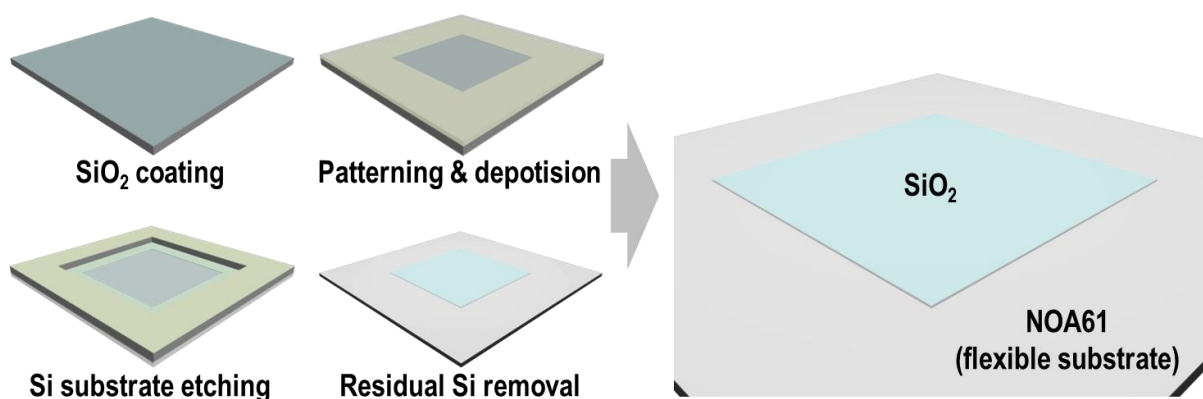
Figure 4.22. Schematic of sample fabrication process of silicon dioxide thin films for cyclic bending test.

4.4.6 Testing condition of cyclic bending test

   Repeated bending experiments were carried out using self-production equipment. The equipment has been modified appropriately based on repeated machine developed by B. J. kim[94]. The machine is designed to use the rod to translate the rotational motion generated by the motor to the support plate as a linear motion. As shown in Figure 4.23, supporting plate was positioned with both ends fixed between two parallel plates. While the upper plate remains stationary, the lower plate performs a linear motion transmitted from the motor. The sample was prepared by depositing a 700 nm thick silicon dioxide thin film on 100 μm thick NOA61 with a 100 μm thick metal support layer. The critical bending curvature of the silicon dioxide thin film was estimated to be 3.1 mm when analyzed using the method described in section 2.4 above. The distance between two plates was set considering the elastic limit of the silicon dioxide thin film and was set to 3, 4, 5, 7, 10 mm which applied a tensile strain of 3.8, 2.9, 2.3, 1.6, 1.2% on silicon dioxide thin film. Compressive and tensile strain is applied to samples attached on inner and outer surface of supporting plate, respectively. Testing samples were attached on inner surface of supporting plate for apply compressive stress to sample because compressive strain is generally applied on encapsulation material used with substrate during mechanical bending deformation due to its position from neutral axis.

   As shown in Figure 4.24, three different deformation sections are created in the supporting jig by the linear motion of the lower plate. Deformation sections consisted of zone A which is not deformed area, zone B which is repeatedly deformed are, and zone C which continuous bending deformed area. Zone c also remained undamaged area by cyclic bending deformation because the same strain acts continuously. When the strain is applied below the yield strength of the silicon dioxide thin film, cracks do not occur by cyclic bending test. In case of zone B, bending and unbending are repeated according to the repetitive linear deformation of the lower plate, and the strain is repeatedly changed in the sample. As shown in Figure 4.25 and Table 4.2, the length of zone B depends on the stroke of the lower plate and the distance between plate. After confirming the position of zone B considering various factors, the sample was attached on zone B and the experiment was conducted. The reference position was the center of the supporting plate when the stroke was zero. The sample was attached at 20 mm from reference point.

   The test was carried out so that the bending deformation was applied to sample as 1 cycle per second. The repeated bending deformation progressed up to 10,000 cycles depending on the bending curvature. Crack initiation and propagation were measured by optical microscopy.
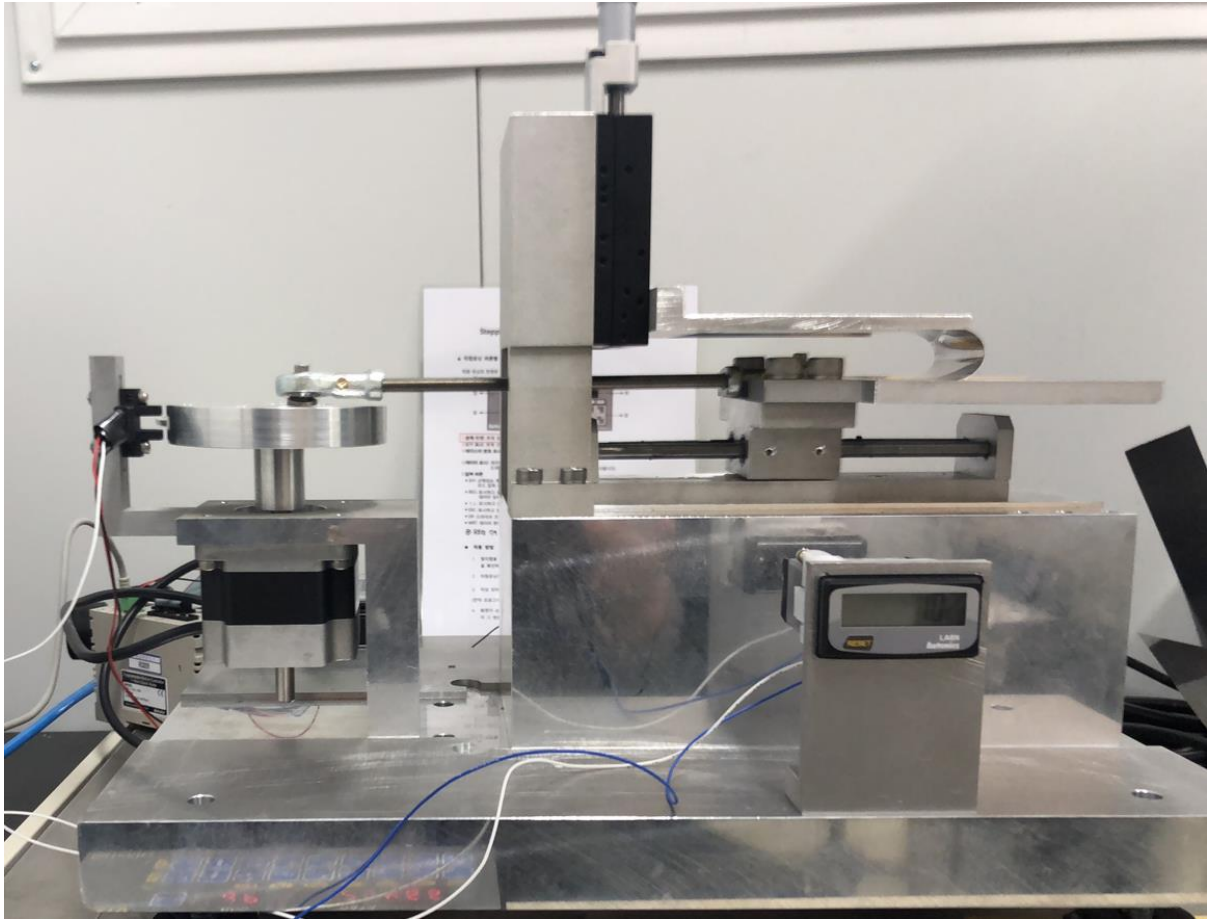
Figure 4.23. Image of cyclic bending machine.
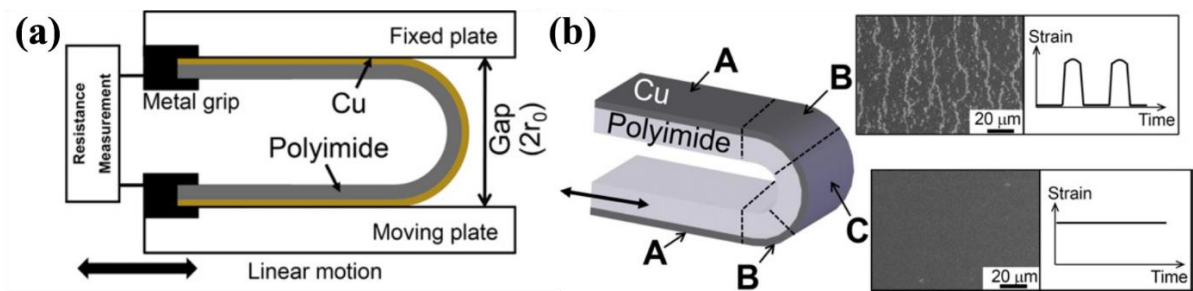
Figure 4.24. Schematic illustrations of cyclic bending machine and (b) deformation zone of supporting plate. Undeformed zone (A), cyclic bending zone (B), and continuous bending zone (C)[94].
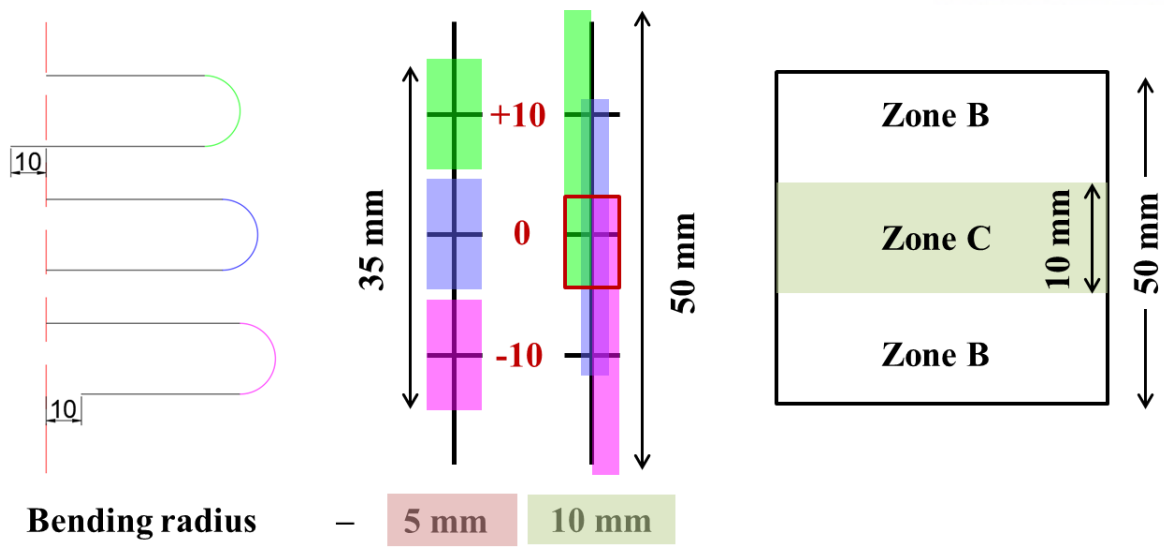
Figure 4.25. Schematic of distance of zone A and B on supporting plate at 20 mm stroke.

Table 4.2. Length of zone B and Zone C according to bending radius.

Bending radius (r, mm)	Circumference/2 (πr, mm)	Zone B (mm)	Zone C (mm)
2	6	26	0
4	12	32	0
6	18	38	0
8	24	40	4
10	30	40	10

4.4.7 Result of cyclic bending test

   The repeated bending experiments were conducted by controlling the bending curvature applied to the device by controlling the distance between the two plates as shown in Figure 4.26. Bending radius was defined as half of distance between upper and lower plate. The bending curvature was reduced from 10 mm to 3 mm. Repeated bending was performed up to 10,000 cycles at each bending radius. Confirmation of defect initiation was performed with an optical microscope after bending at 100, 200, 500, 1,000, 2,000, 5,000, and 10,000 cycles.

   As shown in Figure 4.27, a portion of chromium and silicon dioxide thin film overlaps was created due to the inaccuracies of the shadow mask process during sample preparation. In the case of chromium deposited on NOA61, cracks occur in deformation due to residual stress difference. Cracks are also generated even in the portion where chromium and silicon dioxide were overlapped. Therefore, the cracks in the chromium easily propagate to the silicon dioxide thin film during cyclic deformation. For this reason, cracks generated in chromium and propagated to silicon dioxide thin films were excluded from the results of repeated bending deformation.
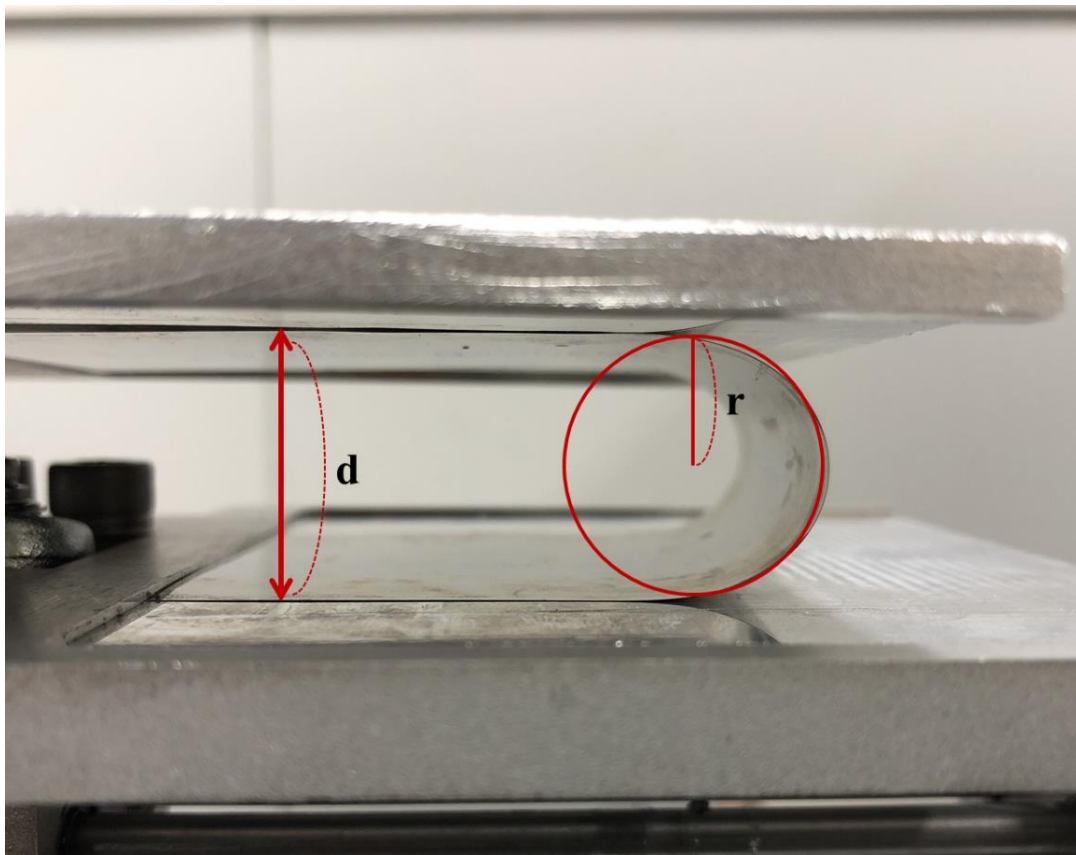
Figure 4.26. Image of supporting plate fixed upper and lower plate. Bending radius(r) is half of distance (d) between upper and lower plate.
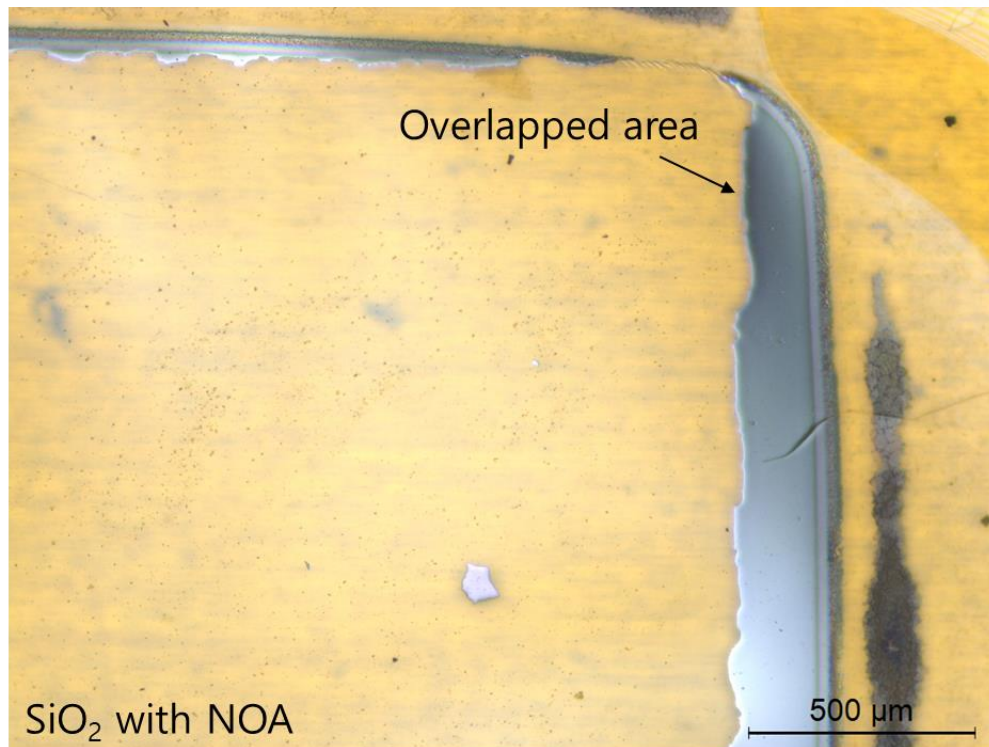
Figure 4.27. Optical microscopy image of edge of silicon dioxide sample for cyclic bending test attached on supporting plate.

The images were taken at the same place to confirm the initiation of cracks. As show in Figure 4.28, cracks did not occur when repeated bending was performed up to 10,000 cycles from 10 mm to 4 mm in bending radius. At each bending radius, images of sample surfaces were presented after 100 and 10,000 bending cycle. The transmittance of the silicon dioxide thin film is so high that it is difficult to confirm whether the silicon dioxide thin film has cracks. Chromium particles attached on silicon dioxide layer during etching process were used as reference point to take images at same position and presence of cracks was confirmed. The black dot on the silicon dioxide thin film was residual silicon particle after the etching process and was used for focusing during the microscopic observation.

At a bending curvature of 3 mm, it was confirmed that cracks were generated after 100 cycles of bending. The change in sample surface image due to repeated bending deformation is shown in Figure 4.29. Crack propagated as repeated bending progressed up to 5,000 cycles. When the bending curvature is 3 and 4 mm, the strains applied to the sample are 3.8 and 2.9%, respectively. Based on the elastic limit of 3.7% obtained from the tensile test. The two results show that the silicon dioxide thin film does not break even if it undergoes repeated bending below the elastic limit, and if the strain exceeding the elastic limit is applied, the silicon dioxide film breaks.

(a) r_b= 10 mm at 100 cycles — 100 μm

(b) r_b= 10 mm at 10,000 cycles — 100 μm

(c) r_b= 7 mm at 100 cycles — 100 μm

(d) r_b= 7 mm at 10,000 cycles — 100 μm

(e) r_b= 5 mm at 100 cycles — 100 μm

(f) r_b= 5 mm at 10,000 cycles — 100 μm

(g) r_b= 4 mm at 100 cycles — 100 μm

(h) r_b= 4 mm at 10,000 cycles — 100 μm
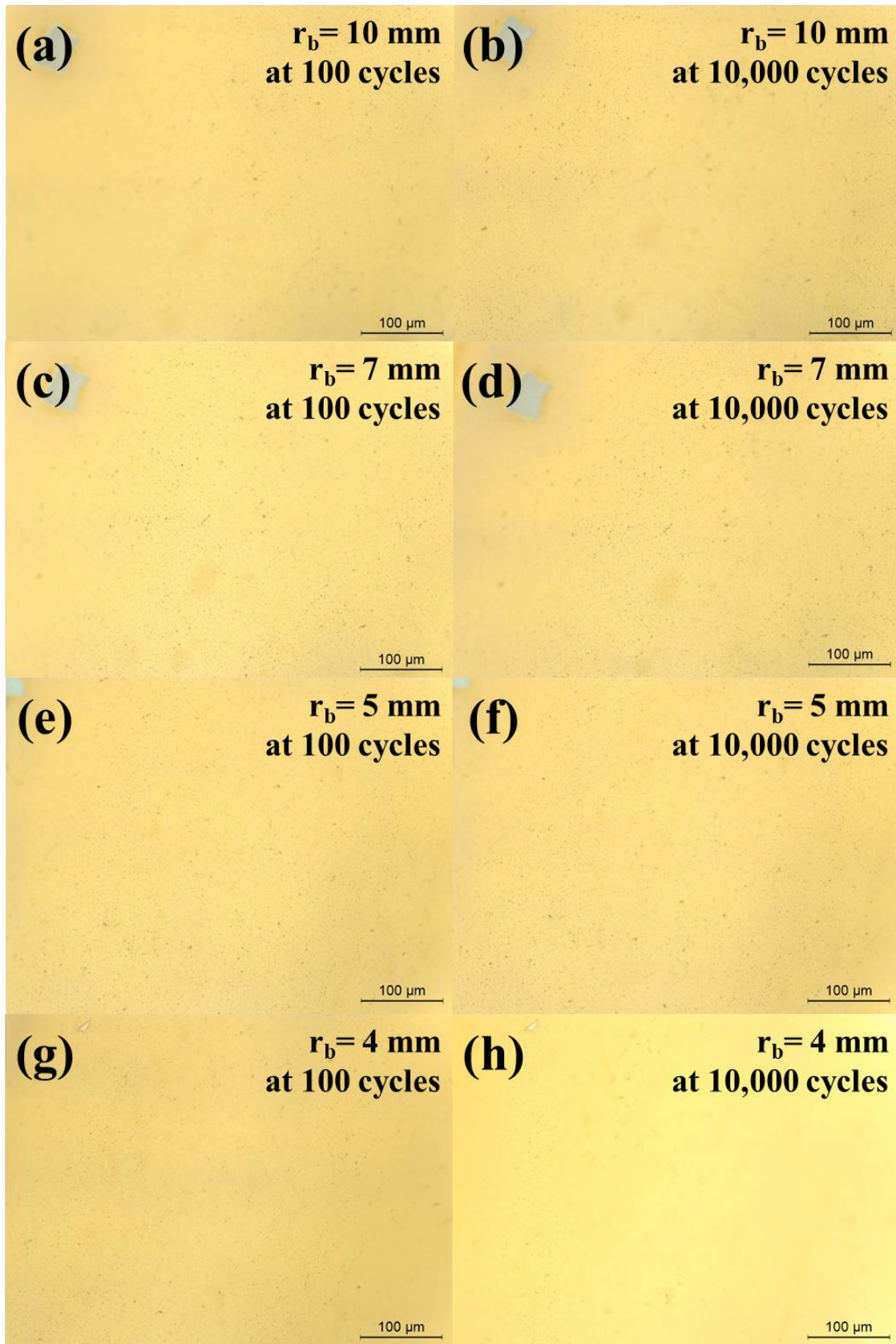
Figure 4.28. Optical microscopy image of silicon dioxide surface after 100 and 10,000 bending cycles at bending radius of 10, 7, 5, and 4 mm
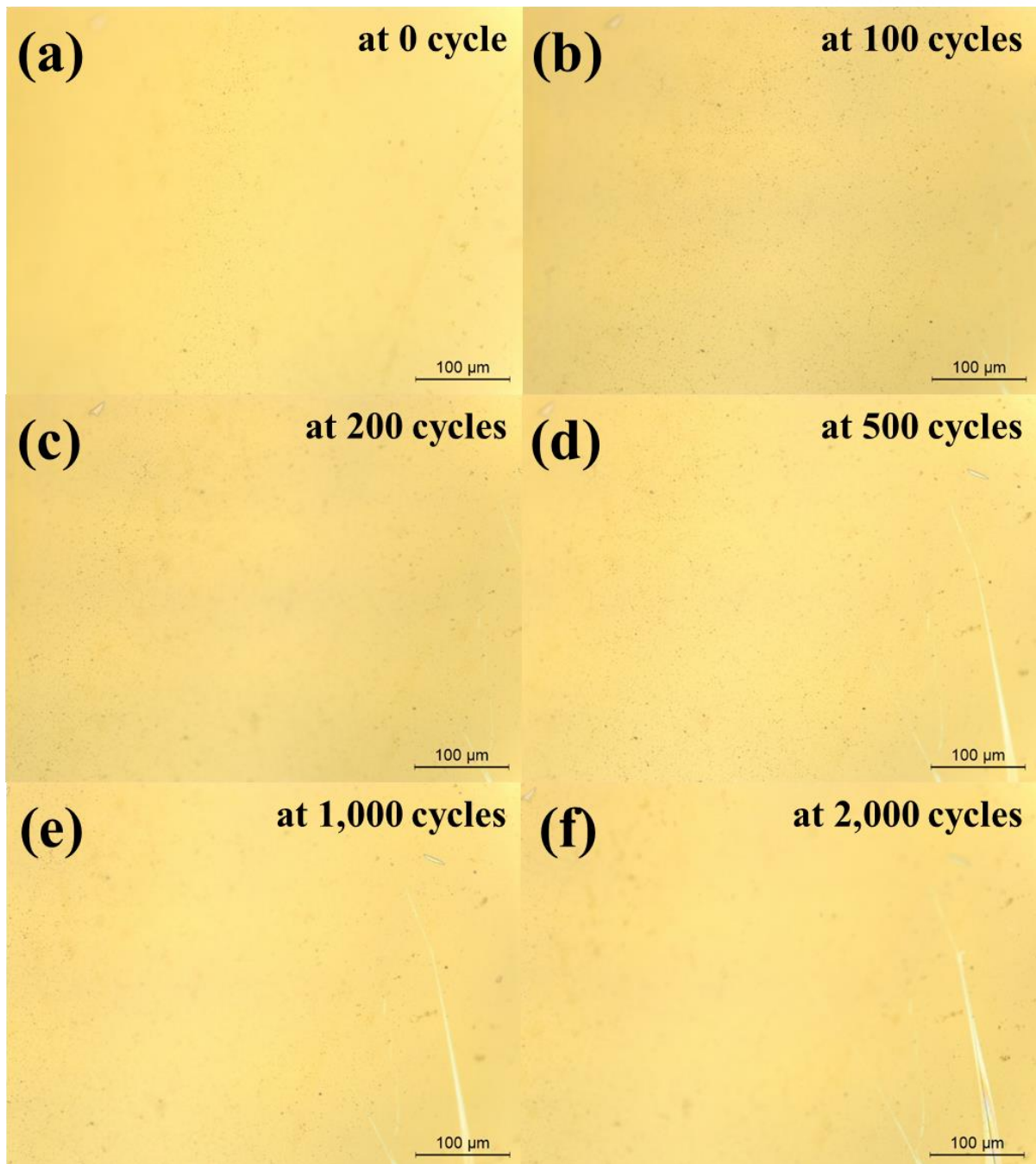
Figure 4.29. Optical microscopy image of silicon dioxide surface before and after 100, 200, 500, 1000, and 2000 bending cycles at bending radius of 3 mm

5. Conclusion

Flexible devices were fabricated using perovskite layer used as emission layer and flexibility was analyzed. The reduced efficiency during repeated bending at 2 mm bending curvature is similar to the reduced efficiency of the device with natural deterioration. When the bending curvature was 1 mm, the efficiency of the device decreased sharply as the repeated bending cycles increased. Based on the results of repeated bending experiments, the critical bending radius of the perovskite LED was analyzed to be 1 mm. Hole-indentation tests were performed to measure elastic limit of constituent materials of perovskite LEDs. The elastic limit of the perovskite was measured 10 times lower than the other components, confirming that perovskite layer is the weakest material among the constituent materials. In-situ micro-tensile tests were performed to measure accurate mechanical properties of perovskite. The strain of perovskite samples was measured at 1.1% using digital image correlation method. The critical bending radius was analyzed to be 0.96 mm using the elastic limit of perovskite layer. The critical bending curvature of 0.96 mm, which was analyzed by using the elastic limit, was similar to the bend curvature of 1 mm, in which the efficiency of the device decreased sharply during the repeated bending test. The degradation of perovskite LEDs during repeated bending deformation is caused by local deformation of perovskite layer.

Silicon dioxide thin films for encapsulation materials were fabricated by sol-gel process. The water vapor transmission rate of the silicon dioxide thin film was measured as 1.5×10^{-2} using MOCON. In-situ micro-tensile tests and cyclic loading tests were carried out to measure mechanical properties of silicon dioxide thin films. Silicon dioxide thin films was elastically deformed without plastic deformation behavior and brittle fractured at a strain of 3.7%. The critical bend radius on polymer substrate was calculated using the elastic limit of silicon dioxide and position of neutral plane and repeated bending tests were carried out up to 10000 cycles at near critical bending radius. At the strain below the elastic limit, defects were not formed in the silicon dioxide thin film during repeated bending test. However, cracks were generated and propagated at strain above elastic limit. Based on the results of repeated bending experiments, it can be applied to the flexible device at the strain below the elastic limit. In addition, the critical bending curvature can be reduced when the polymer is laminated on the silicon dioxide thin film and the thin film is moved close to the neutral plane.

Reference

1.	Tan, Z. K.;	Moghaddam, R. S.;	Lai, M. L.;	Docampo, P.;	Higler, R.;	Deschler, F.;	Price, M.;	Sadhanala, A.;	Pazos, L. M.;	Credgington, D.;	Hanusch, F.;	Bein, T.;	Snaith, H. J.;	Friend, R. H., Bright light-emitting diodes based on organometal halide perovskite. *Nature Nanotechnology* **2014,** *9* (9), 687-692.

2.	Wang, J.;	Wang, N.;	Jin, Y.;	Si, J.;	Tan, Z.-K.;	Du, H.;	Cheng, L.;	Dai, X.;	Bai, S.;	He, H.;	Ye, Z.;	Lai, M. L.;	Friend, R. H.; Huang, W., Interfacial Control Toward Efficient and Low-Voltage Perovskite Light-Emitting Diodes. *Advanced Materials* **2015,** *27* (14), 2311-2316.

3.	Deschler, F.;	Price, M.;	Pathak, S.;	Klintberg, L. E.;	Jarausch, D.-D.;	Higler, R.;	Huettner, S.;	Leijtens, T.;	Stranks, S. D.;	Snaith, H. J.;	Atatuere, M.;	Phillips, R. T.; Friend, R. H., High Photoluminescence Efficiency and Optically Pumped Lasing in Solution-Processed Mixed Halide Perovskite Semiconductors. *Journal of Physical Chemistry Letters* **2014,** *5* (8), 1421-1426.

4.	Kim, J.;	Nam, Y. S.;	Song, M. H.; Park, H. W., Large pulsed electron beam welded percolation networks of silver nanowires for transparent and flexible electrodes. *Acs Applied Materials & Interfaces* **2016,** *8* (32), 20938-20945.

5.	White, M. S.;	Kaltenbrunner, M.;	Głowacki, E. D.;	Gutnichenko, K.;	Kettlgruber, G.;	Graz, I.;	Aazou, S.;	Ulbricht, C.;	Egbe, D. A.; Miron, M. C., Ultrathin, highly flexible and stretchable PLEDs. *Nature Photonics* **2013,** *7* (10), 811.

6.	Li, L.;	Yu, Z.;	Hu, W.;	Chang, C. h.;	Chen, Q.; Pei, Q., Efficient Flexible Phosphorescent Polymer Light-Emitting Diodes Based on Silver Nanowire-Polymer Composite Electrode. *Advanced Materials* **2011,** *23* (46), 5563-5567.

7.	Liang, J.;	Li, L.;	Tong, K.;	Ren, Z.;	Hu, W.;	Niu, X.;	Chen, Y.; Pei, Q., Silver nanowire percolation network soldered with graphene oxide at room temperature and its application for fully stretchable polymer light-emitting diodes. *Acs Nano* **2014,** *8* (2), 1590-1600.

8.	Yu, Z.;	Zhang, Q.;	Li, L.;	Chen, Q.;	Niu, X.;	Liu, J.; Pei, Q., Highly flexible silver nanowire electrodes for shape-memory polymer light-emitting diodes. *Advanced Materials* **2011,** *23* (5), 664-668.

9.	Liang, J.;	Li, L.;	Niu, X.;	Yu, Z.; Pei, Q., Elastomeric polymer light-emitting devices and displays. *Nature Photonics* **2013,** *7* (10), 817.

10.	Jung, E. D.;	Nam, Y. S.;	Seo, H.;	Lee, B. R.;	Yu, J. C.;	Lee, S. Y.;	Kim, J.-Y.;	Park, J.-U.; Song, M. H., Highly efficient flexible optoelectronic devices using metal nanowire-conducting polymer composite transparent electrode. *Electronic Materials Letters* **2015,** *11* (5), 906-

914.

11.   Cho, H. C.;   Jeong, S. H.;   Park, M. H.;   Kim, Y. H.;   Wolf, C.;   Lee, C. L.;   Heo, J. H.;   Sadhanala, A.;   Myoung, N.;   Yoo, S.;   Im, S. H.;   Friend, R. H.; Lee, T. W., Overcoming the electroluminescence efficiency limitations of perovskite light-emitting diodes. *Science* **2015,** *350* (6265), 1222-1225.

12.   Xiao, Z.;   Kerner, R. A.;   Zhao, L.;   Tran, N. L.;   Lee, K. M.;   Koh, T.-W.;   Scholes, G. D.; Rand, B. P., Efficient perovskite light-emitting diodes featuring nanometre-sized crystallites. *Nature Photonics* **2017,** *11* (2), 108-115.

13.   Wei, Z.;   Perumal, A.;   Su, R.;   Sushant, S.;   Xing, J.;   Zhang, Q.;   Tan, S. T.;   Demir, H. V.; Xiong, Q., Solution-processed highly bright and durable cesium lead halide perovskite light-emitting diodes. *Nanoscale* **2016,** *8* (42), 18021-18026.

14.   Zhang, L.;   Yang, X.;   Jiang, Q.;   Wang, P.;   Yin, Z.;   Zhang, X.;   Tan, H.;   Yang, Y. M.;   Wei, M.;   Sutherland, B. R.;   Sargent, E. H.; You, J., Ultra-bright and highly efficient inorganic based perovskite light-emitting diodes. *Nature Communications* **2017,** *8*.

15.   Wang, N. N.;   Cheng, L.;   Ge, R.;   Zhang, S. T.;   Miao, Y. F.;   Zou, W.;   Yi, C.;   Sun, Y.;   Cao, Y.;   Yang, R.;   Wei, Y. Q.;   Guo, Q.;   Ke, Y.;   Yu, M. T.;   Jin, Y. Z.;   Liu, Y.;   Ding, Q. Q.;   Di, D. W.;   Yang, L.;   Xing, G. C.;   Tian, H.;   Jin, C. H.;   Gao, F.;   Friend, R. H.;   Wang, J. P.; Huang, W., Perovskite light-emitting diodes based on solution-processed self-organized multiple quantum wells. *Nature Photonics* **2016,** *10* (11), 699-+.

16.   Cao, Y.;   Wang, N. N.;   Tian, H.;   Guo, J. S.;   Wei, Y. Q.;   Chen, H.;   Miao, Y. F.;   Zou, W.;   Pan, K.;   He, Y. R.;   Cao, H.;   Ke, Y.;   Xu, M. M.;   Wang, Y.;   Yang, M.;   Du, K.;   Fu, Z. W.;   Kong, D. C.;   Dai, D. X.;   Jin, Y. Z.;   Li, G. Q.;   Li, H.;   Peng, Q. M.;   Wang, J. P.;   Huang, W., Perovskite light-emitting diodes based on spontaneously formed submicrometre-scale structures. *Nature* **2018,** *562* (7726), 249-+.

17.   Lin, K. B.;   Xing, J.;   Quan, L. N.;   de Arquer, F. P. G.;   Gong, X. W.;   Lu, J. X.;   Xie, L. Q.;   Zhao, W. J.;   Zhang, D.;   Yan, C. Z.;   Li, W. Q.;   Liu, X. Y.;   Lu, Y.;   Kirman, J.;   Sargent, E. H.;   Xiong, Q. H.; Wei, Z. H., Perovskite light-emitting diodes with external quantum efficiency exceeding 20 per cent. *Nature* **2018,** *562* (7726), 245-+.

18.   Bade, S. G. R.;   Li, J. Q.;   Shan, X.;   Ling, Y. C.;   Tian, Y.;   Dilbeck, T.;   Besara, T.;   Geske, T.;   Gao, H. W.;   Ma, B. W.;   Hanson, K.;   Siegrist, T.;   Xu, C. Y.; Yu, Z. B., Fully Printed Halide Perovskite Light-Emitting Diodes with Silver Nanowire Electrodes. *Acs Nano* **2016,** *10* (2), 1795-1801.

19.   Bade, S. G. R.;   Shan, X.;   Hoang, P. T.;   Li, J. Q.;   Geske, T.;   Cai, L.;   Pei, Q. B.;   Wang, C.; Yu, Z. B., Stretchable Light-Emitting Diodes with Organometal-Halide-Perovskite-Polymer Composite Emitters. *Advanced Materials* **2017,** *29* (23).

20.   Seo, H. K.;   Kim, H.;   Lee, J.;   Park, M. H.;   Jeong, S. H.;   Kim, Y. H.;   Kwon, S. J.;

Han, T. H.; Yoo, S.; Lee, T. W., Efficient Flexible Organic/Inorganic Hybrid Perovskite Light-Emitting Diodes Based on Graphene Anode. *Advanced Materials* **2017,** *29* (12).

21. Zhao, L. F.; Rolston, N.; Lee, K. M.; Zhao, X. H.; Reyes-Martinez, M. A.; Tran, N. L.; Yeh, Y. W.; Yao, N.; Scholes, G. D.; Loo, Y. L.; Selloni, A.; Dauskardt, R. H.; Rand, B. P., Influence of Bulky Organo-Ammonium Halide Additive Choice on the Flexibility and Efficiency of Perovskite Light-Emitting Devices. *Advanced Functional Materials* **2018,** *28* (31).

22. Kim, Y. H.; Cho, H.; Heo, J. H.; Kim, T. S.; Myoung, N.; Lee, C. L.; Im, S. H.; Lee, T. W., Multicolored Organic/Inorganic Hybrid Perovskite Light-Emitting Diodes. *Advanced Materials* **2015,** *27* (7), 1248-1254.

23. Feng, J., Mechanical properties of hybrid organic-inorganic CH3NH3BX3 (B = Sn, Pb; X = Br, I) perovskites for solar cell absorbers. *Apl Materials* **2014,** *2* (8).

24. Lomonosov, A. M.; Yan, X. L.; Sheng, C. X.; Gusev, V. E.; Ni, C. Y.; Shen, Z., Exceptional elastic anisotropy of hybrid organic-inorganic perovskite CH3NH3PbBr3 measured by laser ultrasonic technique. *Physica Status Solidi-Rapid Research Letters* **2016,** *10* (8), 606-612.

25. Letoublon, A.; Paofai, S.; Ruffle, B.; Bourges, P.; Hehlen, B.; Michel, T.; Ecolivet, C.; Durand, O.; Cordier, S.; Katan, C.; Even, J., Elastic Constants, Optical Phonons, and Molecular Relaxations in the High Temperature Plastic Phase of the CH3NH3PbBr3 Hybrid Perovskite. *Journal of Physical Chemistry Letters* **2016,** *7* (19), 3776-3784.

26. Rakita, Y.; Cohen, S. R.; Kedem, N. K.; Hodes, G.; Cahen, D., Mechanical properties of APbX (3) (A = Cs or CH3NH3; X = I or Br) perovskite single crystals. *Mrs Communications* **2015,** *5* (4), 623-629.

27. Sun, S. J.; Fang, Y. N.; Kieslich, G.; White, T. J.; Cheetham, A. K., Mechanical properties of organic-inorganic halide perovskites, CH3NH3PbX3 (X = I, Br and Cl), by nanoindentation. *Journal of Materials Chemistry A* **2015,** *3* (36), 18450-18455.

28. Chen, Y. N.; He, M. H.; Peng, J. J.; Sun, Y.; Liang, Z. Q., Structure and Growth Control of Organic-Inorganic Halide Perovskites for Optoelectronics: From Polycrystalline Films to Single Crystals. *Advanced Science* **2016,** *3* (4).

29. Song, T. B.; Chen, Q.; Zhou, H. P.; Jiang, C. Y.; Wang, H. H.; Yang, Y.; Liu, Y. S.; You, J. B.; Yang, Y., Perovskite solar cells: film formation and properties. *Journal of Materials Chemistry A* **2015,** *3* (17), 9032-9050.

30. Suo, Z.; Ma, E. Y.; Gleskova, H.; Wagner, S., Mechanics of rollable and foldable film-on-foil electronics. *Applied Physics Letters* **1999,** *74* (8), 1177-1179.

31. Hsueh, C. H., Modeling of elastic deformation of multilayers due to residual stresses and external bending. *Journal of Applied Physics* **2002,** *91* (12), 9652-9656.

32. Burroughes, J. H.; Bradley, D. D. C.; Brown, A. R.; Marks, R. N.; Mackay, K.; Friend, R. H.; Burn, P. L.; Holmes, A. B., LIGHT-EMITTING-DIODES BASED ON

CONJUGATED POLYMERS. *Nature* **1990,** *347* (6293), 539-541.

33.   Kraft, A.;   Grimsdale, A. C.; Holmes, A. B., Electroluminescent conjugated polymers - Seeing polymers in a new light. *Angewandte Chemie-International Edition* **1998,** *37* (4), 402-428.

34.   Gu, G.;   Bulovic, V.;   Burrows, P. E.;   Forrest, S. R.; Thompson, M. E., Transparent organic light emitting devices. *Applied Physics Letters* **1996,** *68* (19), 2606-2608.

35.   Burrows, P. E.;   Forrest, S. R.; Thompson, M. E., Prospects and applications for organic light-emitting devices. *Current Opinion in Solid State & Materials Science* **1997,** *2* (2), 236-243.

36.   Aziz, H.;   Popovic, Z.;   Tripp, C. P.;   Hu, N. X.;   Hor, A. M.; Xu, G., Degradation processes at the cathode/organic interface in organic light emitting devices with Mg : Ag cathodes. *Applied Physics Letters* **1998,** *72* (21), 2642-2644.

37.   Aziz, H.;   Popovic, Z.;   Xie, S.;   Hor, A. M.;   Hu, N. X.;   Tripp, C.; Xu, G., Humidity-induced crystallization of tris (8-hydroxyquinoline) aluminum layers in organic light-emitting devices. *Applied Physics Letters* **1998,** *72* (7), 756-758.

38.   McElvain, J.;   Antoniadis, H.;   Hueschen, M. R.;   Miller, J. N.;   Roitman, D. M.;   Sheats, J. R.; Moon, R. L., Formation and growth of black spots in organic light-emitting diodes. *Journal of Applied Physics* **1996,** *80* (10), 6002-6007.

39.   Do, L. M.;   Han, E. M.;   Niidome, Y.;   Fujihira, M.;   Kanno, T.;   Yoshida, S.;   Maeda, A.; Ikushima, A. J., OBSERVATION OF DEGRADATION PROCESSES OF AL ELECTRODES IN ORGANIC ELECTROLUMINESCENCE DEVICES BY ELECTROLUMINESCENCE MICROSCOPY, ATOMIC FARCE MICROSCOPY, SCANNING ELECTRON-MICROSCOPY, AND ANGER ELECTRON-SPECTROSCOPY. *Journal of Applied Physics* **1994,** *76* (9), 5118-5121.

40.   Schaer, M.;   Nuesch, F.;   Berner, D.;   Leo, W.; Zuppiroli, L., Water vapor and oxygen degradation mechanisms in organic light emitting diodes. *Advanced Functional Materials* **2001,** *11* (2), 116-121.

41.   Wang, C. C.;   Ecker, B. R.;   Wei, H. T.;   Huang, J. S.; Gao, Y. L., Environmental Surface Stability of the MAPbBr(3) Single Crystal. *J Phys Chem C* **2018,** *122* (6), 3513-3522.

42.   Dong, X.;   Fang, X.;   Lv, M. H.;   Lin, B. C.;   Zhang, S.;   Ding, J. N.; Yuan, N. Y., Improvement of the humidity stability of organic-inorganic perovskite solar cells using ultrathin Al2O3 layers prepared by atomic layer deposition. *Journal of Materials Chemistry A* **2015,** *3* (10), 5360-5367.

43.   Berhe, T. A.;   Su, W. N.;   Chen, C. H.;   Pan, C. J.;   Cheng, J. H.;   Chen, H. M.;   Tsai, M. C.;   Chen, L. Y.;   Dubale, A. A.; Hwang, B. J., Organometal halide perovskite solar cells: degradation and stability. *Energ Environ Sci* **2016,** *9* (2), 323-356.

44.   Park, J. S.;   Chae, H.;   Chung, H. K.; Lee, S. I., Thin film encapsulation for flexible AM-OLED: a review. *Semiconductor Science and Technology* **2011,** *26* (3).

45.   Burrows, P. E.;   Bulovic, V.;   Forrest, S. R.;   Sapochak, L. S.;   McCarty, D. M.;

Thompson, M. E., RELIABILITY AND DEGRADATION OF ORGANIC LIGHT-EMITTING DEVICES. *Applied Physics Letters* **1994,** *65* (23), 2922-2924.

46.	Grego, S.;	Lewis, J.;	Vick, E.; Temple, D., A method to evaluate mechanical performance of thin transparent films for flexible displays. *Thin Solid Films* **2007,** *515* (11), 4745-4752.

47.	Yu, D.;	Yang, Y. Q.;	Chen, Z.;	Tao, Y.; Liu, Y. F., Recent progress on thin-film encapsulation technologies for organic electronic devices. *Optics Communications* **2016,** *362*, 43-49.

48.	Lewis, J. S.; Weaver, M. S., Thin-film permeation-barrier technology for flexible organic light-emitting devices. *Ieee Journal of Selected Topics in Quantum Electronics* **2004,** *10* (1), 45-57.

49.	Jamieson, E. H. H.; Windle, A. H., STRUCTURE AND OXYGEN-BARRIER PROPERTIES OF METALLIZED POLYMER FILM. *Journal of Materials Science* **1983,** *18* (1), 64-80.

50.	Wuu, D. S.;	Chen, T. N.;	Wu, C. C.;	Chiang, C. C.;	Chen, Y. P.;	Horng, R. H.; Juang, F. S., Transparent barrier coatings for flexible organic light-emitting diode applications. *Chemical Vapor Deposition* **2006,** *12* (4), 220-224.

51.	Schaepkens, M.;	Kim, T. W.;	Erlat, A. G.;	Yan, M.;	Flanagan, K. W.;	Heller, C. M.; McConnelee, P. A., Ultrahigh barrier coating deposition on polycarbonate substrates. *Journal of Vacuum Science & Technology A* **2004,** *22* (4), 1716-1722.

52.	Seo, S. W.;	Jung, E.;	Seo, S. J.;	Chae, H.;	Chung, H. K.; Cho, S. M., Toward fully flexible multilayer moisture-barriers for organic light-emitting diodes. *Journal of Applied Physics* **2013,** *114* (14).

53.	Affinito, J. D.;	Gross, M. E.;	Coronado, C. A.;	Graff, G. L.;	Greenwell, E. N.; Martin, P. M., A new method for fabricating transparent barrier layers. *Thin Solid Films* **1996,** *290*, 63-67.

54.	Greener, J.;	Ng, K. C.;	Vaeth, K. M.; Smith, T. M., Moisture permeability through multilayered barrier films as applied to flexible OLED display. *Journal of Applied Polymer Science* **2007,** *106* (5), 3534-3542.

55.	Janicki, V.;	Sancho-Parramon, J.;	Stenzel, O.;	Lappschies, M.;	Goertz, B.;	Rickers, C.;	Polenzky, C.; Richter, U., Optical characterization of hybrid antireflective coatings using spectrophotometric and ellipsometric measurements. *Applied Optics* **2007,** *46* (24), 6084-6091.

56.	Tikhonravov, A. V.;	Trubetskov, M. K.; DeBell, G. W., Optical coating design approaches based on the needle optimization technique. *Applied Optics* **2007,** *46* (5), 704-710.

57.	Lee, J.;	Wu, J.;	Ryu, J. H.;	Liu, Z. J.;	Meitl, M.;	Zhang, Y. W.;	Huang, Y. G.; Rogers, J. A., Stretchable Semiconductor Technologies with High Areal Coverages and Strain-Limiting Behavior: Demonstration in High-Efficiency Dual-Junction GaInP/GaAs Photovoltaics. *Small* **2012,** *8* (12), 1851-1856.

58.	Lee, P.;	Lee, J.;	Lee, H.;	Yeo, J.;	Hong, S.;	Nam, K. H.;	Lee, D.;	Lee, S. S.; Ko, S. H., Highly Stretchable and Highly Conductive Metal Electrode by Very Long Metal Nanowire

Percolation Network. *Advanced Materials* **2012,** *24* (25), 3326-3332.

59.   Vijay, V.;   Rao, A. D.; Narayan, K. S., In situ studies of strain dependent transport properties of conducting polymers on elastomeric substrates. *Journal of Applied Physics* **2011,** *109* (8).

60.   Charton, C.;   Schiller, N.;   Fahland, M.;   Hollander, A.;   Wedel, A.; Noller, K., Development of high barrier films on flexible polymer substrates. *Thin Solid Films* **2006,** *502* (1-2), 99-103.

61.   Chwang, A. B.;   Rothman, M. A.;   Mao, S. Y.;   Hewitt, R. H.;   Weaver, M. S.; Silvernail, J. A.;   Rajan, K.;   Hack, M.;   Brown, J. J.;   Chu, X.;   Moro, L.;   Krajewski, T.; Rutherford, N., Thin film encapsulated flexible organic electroluminescent displays. *Applied Physics Letters* **2003,** *83* (3), 413-415.

62.   Chatham, H., Oxygen diffusion barrier properties of transparent oxide coatings on polymeric substrates. *Surface & Coatings Technology* **1996,** *78* (1-3), 1-9.

63.   Pantano, M. F.;   Espinosa, H. D.; Pagnotta, L., Mechanical characterization of materials at small length scales. *Journal of Mechanical Science and Technology* **2012,** *26* (2), 545-561.

64.   Yoshioka, T.;   Ando, T.;   Shikida, M.; Sato, K., Tensile testing of SiO2 and Si3N4 films carried out on a silicon chip. *Sensors and Actuators a-Physical* **2000,** *82* (1-3), 291-296.

65.   Tsuchiya, T.;   Inoue, A.; Sakata, J., Tensile testing of insulating thin films; humidity effect on tensile strength of SiO2 films. *Sensors and Actuators a-Physical* **2000,** *82* (1-3), 286-290.

66.   Kingery, W. D.;   Bowen, H. K.; Uhlmann, D. R., *Introduction to ceramics*. Wiley New York: 1976; Vol. 183.

67.   Chu, J. K.; Zhang, D. Q., Mechanical characterization of thermal SiO(2) micro-beams through tensile testing. *Journal of Micromechanics and Microengineering* **2009,** *19* (9).

68.   Sundararajan, S.;   Bhushan, B.;   Namazu, T.; Isono, Y., Mechanical property measurements of nanoscale structures using an atomic force microscope. *Ultramicroscopy* **2002,** *91* (1-4), 111-118.

69.   Weihs, T. P.;   Hong, S.;   Bravman, J. C.; Nix, W. D., MECHANICAL DEFLECTION OF CANTILEVER MICROBEAMS - A NEW TECHNIQUE FOR TESTING THE MECHANICAL-PROPERTIES OF THIN-FILMS. *Journal of Materials Research* **1988,** *3* (5), 931-942.

70.   Jaccodine, R. J.; Schlegel, W. A., Measurement of Strains at Si-Sio2 Interface. *Journal of Applied Physics* **1966,** *37* (6), 2429-+.

71.   Fang, W.; Wickert, J. A., POST BUCKLING OF MICROMACHINED BEAMS. *Journal of Micromechanics and Microengineering* **1994,** *4* (3), 116-122.

72.   Luo, C.;   Francis, A.; Liu, X., Determination of compressive residual stress in a doubly-clamped microbeam according to its buckled shape. *Microelectronic Engineering* **2008,** *85* (2), 339-347.

73. Matoy, K.; Schonherr, H.; Detzel, T.; Dehm, G., Micron-sized fracture experiments on amorphous SiOx films and SiOx/SiNx multi-layers. *Thin Solid Films* **2010,** *518* (20), 5796-5801.

74. Sharpe, W. N., Jr.; Pulskamp, J.; Gianola, D. S.; Eberl, C.; Polcawich, R. G.; Thompson, R. J., Strain measurements of silicon dioxide microspecimens by digital imaging processing. *Experimental Mechanics* **2007,** *47* (5), 649-658.

75. Zhao, J. H.; Ryan, T.; Ho, P. S.; McKerrow, A. J.; Shih, W. Y., Measurement of elastic modulus, Poisson ratio, and coefficient of thermal expansion of on-wafer submicron films. *Journal of Applied Physics* **1999,** *85* (9), 6421-6424.

76. Chen, F.; Li, B. Z.; Sullivan, T. D.; Gonzalez, C. L.; Muzzy, C. D.; Lee, H. K.; Levy, M. D.; Dashiell, M. W.; Kolodzey, J., Influence of underlying interlevel dielectric films on extrusion formation in aluminum interconnects. *J Vac Sci Technol B* **2000,** *18* (6), 2826-2834.

77. Scott, O. N.; Begley, M. R.; Komaragiri, U.; Mackin, T. J., Indentation of freestanding circular elastomer films using spherical indenters. *Acta Materialia* **2004,** *52* (16), 4877-4885.

78. Komaragiri, U.; Begley, M. R., The mechanical response of freestanding circular elastic films under point and pressure loads. *Journal of Applied Mechanics-Transactions of the Asme* **2005,** *72* (2), 203-212.

79. Lee, C.; Wei, X. D.; Kysar, J. W.; Hone, J., Measurement of the elastic properties and intrinsic strength of monolayer graphene. *Science* **2008,** *321* (5887), 385-388.

80. Berfield, T.; Patel, J.; Shimmin, R.; Braun, P.; Lambros, J.; Sottos, N., Micro-and nanoscale deformation measurement of surface and internal planes via digital image correlation. *Experimental Mechanics* **2007,** *47* (1), 51-62.

81. Knauss, W. G.; Chasiotis, I.; Huang, Y., Mechanical measurements at the micron and nanometer scales. *Mechanics of Materials* **2003,** *35* (3-6), 217-231.

82. Greek, S.; Ericson, F.; Johansson, S.; Schweitz, J.-Å., In situ tensile strength measurement and Weibull analysis of thick film and thin film micromachined polysilicon structures. *Thin Solid Films* **1997,** *292* (1-2), 247-254.

83. Saif, M.; MacDonald, N., Microinstruments for submicron material studies. *Journal of Materials Research* **1998,** *13* (12), 3353-3356.

84. Han, J. H.; Saif, M. T. A., In situ microtensile stage for electromechanical characterization of nanoscale freestanding films. *Rev Sci Instrum* **2006,** *77* (4).

85. Yu, J. C.; Kim, D. B.; Jung, E. D.; Lee, B. R.; Song, M. H., High-performance perovskite light-emitting diodes via morphological control of perovskite films. *Nanoscale* **2016,** *8* (13), 7036-7042.

86. Lee, S. Y.; Kim, S. H.; Nam, Y. S.; Yu, J. C.; Lee, S.; Kim, D. B.; Jung, E. D.; Woo, J. H.; Ahn, S.; Lee, S.; Choi, K. J.; Kim, J. Y.; Song, M. H., Flexibility of Semitransparent Perovskite Light-Emitting Diodes Investigated by Tensile Properties of Perovskite

Layer. *Nano Letters* **Accepted**.

87.   Vosgueritchian, M.;   Lipomi, D. J.; Bao, Z., Highly conductive and transparent PEDOT: PSS films with a fluorosurfactant for stretchable and flexible transparent electrodes. *Advanced Functional Materials* **2012,** *22* (2), 421-428.

88.   Han, J.;   Pugno, N. M.; Ryu, S., Nanoindentation cannot accurately predict the tensile strength of graphene or other 2D materials. *Nanoscale* **2015,** *7* (38), 15672-15679.

89.   Tan, X. J.;   Wu, J.;   Zhang, K. W.;   Peng, X. Y.;   Sun, L. Z.; Zhong, J. X., Nanoindentation models and Young's modulus of monolayer graphene: A molecular dynamics study. *Applied Physics Letters* **2013,** *102* (7).

90.   Tabor, D., The hardness of metals. 1951. Oxford: 2000.

91.   Mkhoyan, K. A.;   Silcox, J.;   Ellison, A.;   Ast, D.; Dieckmann, R., Full recovery of electron damage in glass at ambient temperatures. *Phys Rev Lett* **2006,** *96* (20).

92.   Zheng, K.;   Wang, C. C.;   Cheng, Y. Q.;   Yue, Y. H.;   Han, X. D.;   Zhang, Z.;   Shan, Z. W.;   Mao, S. X.;   Ye, M. M.;   Yin, Y. D.; Ma, E., Electron-beam-assisted superplastic shaping of nanoscale amorphous silica. *Nature Communications* **2010,** *1*.

93.   Mackovic, M.;   Niekiel, F.;   Wondraczek, L.; Spiecker, E., Direct observation of electron-beam-induced densification and hardening of silica nanoballs by in situ transmission electron microscopy and finite element method simulations. *Acta Materialia* **2014,** *79*, 363-373.

94.   Kim, B. J.;   Shin, H. A. S.;   Jung, S. Y.;   Cho, Y.;   Kraft, O.;   Choi, I. S.; Joo, Y. C., Crack nucleation during mechanical fatigue in thin metal films on flexible substrates. *Acta Materialia* **2013,** *61* (9), 3473-3481.